5-2012

Computational Fluid Dynamics Analysis of Butterfly Valve Performance Factors

Adam Del Toro
Utah State University

COMPUTATIONAL FLUID DYNAMICS ANALYSIS OF BUTTERFLY VALVE PERFORMANCE FACTORS

by

Adam Del Toro

A thesis submitted in partial fulfillment
of the requirements for the degree

of

MASTER OF SCIENCE

in

Mechanical Engineering

Approved:

Dr. Robert E. Spall Major Professor	Dr. Michael C. Johnson Committee Member
Dr. Aaron Katz Committee Member	Dr. Mark R. McLellen Vice President for Research and Dean of the School of Graduate Studies

UTAH STATE UNIVERSITY
Logan, Utah

2012

Abstract

Computational Fluid Dynamics Analysis of Butterfly Valve Performance Factors

by

Adam Del Toro, Master of Science

Utah State University, 2012

Major Professor: Dr. Robert E. Spall
Department: Mechanical and Aerospace Engineering

Butterfly valves are commonly used in industrial applications to control the internal flow of both compressible and incompressible fluids. A butterfly valve typically consists of a metal disc formed around a central shaft, which acts as its axis of rotation. As the valve's opening angle, θ, is increased from 0 degrees (fully closed) to 90 degrees (fully open), fluid is able to more readily flow past the valve. Characterizing a valve's performance factors, such as pressure drop, hydrodynamic torque, flow coefficient, loss coefficient, and torque coefficient, is necessary for fluid system designers to account for system requirements to properly operate the valve and prevent permanent damage from occurring. This comparison study of a 48-inch butterfly valve's experimental performance factors using Computational Fluid Dynamics (CFD) in an incompressible fluid at Reynolds numbers ranging approximately between 10^5 to 10^6 found that for mid-open positions (30-60 degrees), CFD was able to appropriately predict common performance factors for butterfly valves. For lower valve angle cases (10-20 degrees), CFD simulations failed to predict those same values, while higher valve angles (70-90 degrees) gave mixed results.

(152 pages)

Public Abstract

Computational Fluid Dynamics Analysis of Butterfly Valve Performance Factors

Adam Del Toro

Butterfly valves are commonly used to control fluid flow inside of piping systems. A butterfly valve typically consists of a metal disc formed around a central shaft, which acts as its axis of rotation. As a butterfly valve is rotated open, fluid is able to more readily flow past the valve. A butterfly valve's design is important to understand and is commonly characterized by its own performance factors. How a butterfly valve will perform, while in operation at different opening angles and under different types of flow, is critical information for individuals planning and installing piping systems involving the valve.

Performance factors common to a butterfly valve include the following: pressure drop, hydrodynamic torque, flow coefficient, loss coefficient, and torque coefficient. While these values can usually be obtained experimentally, it is sometimes not feasible or possible to calculate the performance factors of some butterfly valves. Another method wherein butterfly valve performance factors can be obtained is by using Computational Fluid Dynamics (CFD) software to simulate the physics of fluid flow in a piping system around a butterfly valve. This study sought to compare experimental and simulated CFD performance factors of a 48-inch diameter butterfly valve for various valve openings and flow conditions in order to determine the validity of using CFD to predict butterfly valve performance factors.

It was found that for mid-open butterfly valve positions (30-60 degrees), CFD was able to appropriately predict common performance factors for butterfly valves. For lower valve angle cases (10-20 degrees), CFD simulations failed to predict those same values, while higher valve angles (70-90 degrees) gave mixed results.

Acknowledgments

My wife, Mollie, first and foremost, deserves my thanks for continually aiding me and pushing me across the finish line. There have been innumerable nights of arriving home late from work and studying into the wee hours of the night. She has been a wonderful mother to our children even when I wasn't able to be around to help as much as I would have liked to have been. Her patience, love, and understanding have made this possible.

I would also like to thank Dr. Johnson for giving me the opportunity to be involved in this project with the UWRL and making sure I always had my "beans, bullets, and bandages." And also for being patient with me when the unexpected seemed to occur to me and my family during this past year and a half.

Furthermore, Dr. Spall deserves my gratitude and respect for being an exceptional professor and mentor to me throughout my studies here at Utah State University. I have drawn much on his wisdom and experience, especially when it comes to computational fluid dynamics.

Adam Del Toro

Contents

List of Tables

List of Figures

Acronyms

AWWA	American Water Works Association
ASME	American Society of Mechanical Engineers
CAD	Computer Aided Drafting
CFD	Computational Fluid Dynamics
D	Diameter
GCI	Grid Convergence Index
RANS	Reynold-Averaged Navier-Stokes
RE	Richardson Extrapolation
SST	Shear Stress Transport
TSM	Taylor Series Method
USACE	United States Army Corps of Engineers
UWRL	Utah Water Research Lab
VC	Volumetric Control

Chapter 1

Introduction

Butterfly valves are commonly used in industrial applications to control the internal flow of both compressible and incompressible fluids. A butterfly valve typically consists of a metal disc formed around a central shaft, which acts as its axis of rotation. As the valve's opening angle, θ, is increased from 0° (fully closed) to 90° (fully open), fluid is able to more readily flow past the valve. Butterfly valves must be able to withstand the stresses and forces that results from high Reynolds number flows. Characterizing a valve's performance factors, such as pressure drop, hydrodynamic torque, flow coefficient, loss coefficient, and torque coefficient, is necessary for fluid system designers to account for system requirements to properly operate the valve and prevent permanent damage from occurring to the valve. This study seeks to compare a 48-inch butterfly valve's experimental performance factors to those obtained using Computational Fluid Dynamics (CFD) and to assess the feasibility of using CFD to predict performance factors of butterfly valves.

Chapter 1 will contain a literature review regarding the research done on butterfly valves, its current state-of-art, and its connection to this study. A brief overview of butterfly valve attributes, nomenclature, features, and performance factors will also be highlighted. Chapter 2 will describe the experimental setup carried out by the UWRL for this study, including instrumentation, experimental results, and the uncertainty of the experimental results. Chapter 3 will present a short overview of CFD theory and use. Chapter 4 will provide details regarding the meshing process and setup used on the butterfly valve simulations, including geometry import and tessellation, boundary conditions, meshing models and options, Chapter 5 will cover the physical models used and their corresponding options. Chapter 6 will contain results from the executed CFD simulations, including descriptions of the flow field such as pressure and velocity, predicted performance factors, and demonstrated

grid convergence. Chapter 7 will draw upon results of the experiment and simulations and provide conclusive remarks.

1.1 Literature Review

One the earliest and most comprehensive pieces of research on the flow characteristics and performance of butterfly valves was performed by Cohn [1]. Using data provided by previous authors, Cohn attempted to parameterize torque and flow coefficients based on thickness to diameter ratio for numerous butterfly valve geometries, most of which were symmetrical.

McPherson [2] studied various blade variations of single eccentric butterfly valves in incompressible turbulent flow subject to free, submerged, and continuous piping discharge arrangements. McPherson found that for a given type of installation, the flow characteristics were not significantly influenced by either the shape of the blade or by the closing angle except for the near-open and closed positions, respectively. Using a two dimensional setup of different symmetric butterfly valve blades, cavitation was also predicted.

Sarpkaya [3] also studied the torque and cavitation characteristics of idealized two-dimensional and axially symmetrical butterfly valves by considering an idealized case of laminar uniform flow through a symmetrical lamina (representing the butterfly valve) between two infinite walls. Using these assumptions, Sarpkaya was able to extend approximate solutions to hydrodynamic torque, cavitation, and flow coefficients for three dimensional butterfly valves using semi-empirical equations.

Addy et al. [4] conducted several small-scale compressible flow experiments with sudden enlargement configurations for butterfly valve models to predict mass flowrate and overall pressure characteristics. In addition, a full size butterfly valve was built and tested. The sudden enlargement configurations were classified as three different types of nozzles: contoured converging, conical converging and sharp-edge orifice. It was concluded that the performance characteristics of the valve can be predicted if the valve flow coefficient is known for a specified operating pressure ratio.

Eom [5] building off the work of Cohn [1] and McPherson [2], studied the performance of

butterfly valves as a flow controller. Eom compared the flow characteristics of perforated and non-perforated butterfly valve disks and found their performance to be in good agreement with one another, except at low blade (opening) angle values of about 10 degrees. He also studied the effect that blockage ratios (area of disk to area of pipe or duct) had on butterfly valves as throttling devices. Furthermore, Eom was able to predict loss coefficients sufficiently well from blockage ratios at Reynolds numbers in the range of 10^4.

Kimura et al. [6] and Ogawa and Kimura [7] used free-streamline and wing theory to model symmetric butterfly valves between infinite parallel walls in two dimensions and used correction equations to compensate for pipe wall conditions. The correction equations also required a corrected opening angle and thickness of the disks, and uniform velocity. Using the given two-dimensional models, torque characteristics, pressure loss, and cavitation of three-dimensional experiments were predicted and analyzed. While the general pattern of torque coefficients followed the experimental data, the difference between the predicted and actual values were large. In more recent years since Kimura and Ogawa, scientific and engineering communities in the field of fliud dynamics and valve research have placed more emphasis in Computational Fluid Dynamics (CFD), especially with the advent of commercial CFD software in the 1990s.

Huang and Kim [8] were some of the first to use commercial CFD software to investigate three dimensional flow visualization of a symmetric butterfly valve (modeled as a thin flap valve disk). Huang used CFD code FLUENT to simulate a steady incompressible flow with k-ϵ turbulence modeling. Valve positions were simulated at openings of 30, 45, 60, 70, and 90 degrees. Huang also investigated the length downstream of the valve in which flow would return to fully developed conditions. Due to computational restrictions, a relatively coarse mesh of a maximum of 25,000 cells was used in the CFD calculations. Huang also compared his numerical results with the experiments carried out by Blevins [9]. The 45 degree case was found to be the most agreeable with the experimental data, while the rest lacked agreement.

Lin and Schohl [10] used commercial CFD software FLUENT to predict drag coefficients

for a symmetric coin shaped butterfly valve at opening angles in an infinite flow field with results obtained experimentally by Hoerner [11]. Sensitivity of the results to turbulence model selection, accuracy of discretization schemes, grid quality, and grid dependence were studied as part of the validation. Lin compared k-ϵ, k-ω, and k-ω SST turbulence models and opined that the later model was preferred for resolving the Reynolds-averaged Navier-Stokes equations and that use of a 1^{st} order discretization for the flow domain led to predictions significantly higher than those from the 2^{nd} order schemes. Flow coefficients aligned well with experimental data overall, however it should be noted that exact modeling comparisons between the experimental setup and the numerical model were difficult to match. Lin also modeled a 3.66 meter diameter butterfly valve within a pipe at valve openings of 20, 40, 50, 60, 70, 80, and 90 degrees with cavitation free conditions and incompressible flow using CFD. A computational mesh size included about 1.5 million tetra and hexa-elements. Pressure drop across the valve was calculated and predicted flow coefficients matched relatively well with experimental data provided by the United States Army Corps of Engineers (USACE) for a similarly shaped disc butterfly damper.

Song et al. [12] performed a structural analysis of large butterfly valves, in addition to validating three-dimensional experimental data of a butterfly valve's pressure drop, flow coefficient, and hydrodynamic torque coefficient using general purpose CFD code CFX [13]. The k-ϵ turbulence model was selected by Song since it does not involve the complex non-linear damping functions required by other models. A mesh of nearly one million cells was used with a domain extending eight pipe diameters upstream from the valve and approximately ten pipe diameters downstream. Cases were run for disk opening angles of 5 to 90 degrees in increments of 5 degrees. Generally, good results were obtained except when the valve opening angle was less than 20 degrees. In the 20 degree case, differences between experimental and simulation data were found to be nearly 50%.

Leutwyler and Dalton [14, 15] performed a CFD study in two and three dimensions for symmetric butterfly valves in compressible fluids at various angles and over a range of of pressure ratios. The general purpose CFD code FLUENT was used with the following

turbulence models: Spalart-Allmaras, k-ϵ, and k-ω. Leutwyler favored the k-ϵ turbulence model for its well rounded capabilities and moderate computational costs. In addition to examining grid refinement, coefficients for lift, drag and torque were validated against experimental values.

Henderson et al. [16] measured torque and head loss of a symmetrical butterfly valve installed in a hydro-electric power generating scheme for steady flow at Reynolds numbers of order 10^6. This was done for valve opening angles of 10 to 80 degrees in 10 degree increments. The general purpose CFD software ANSYS CFX was validated using collected experimental data. In the experiment, Henderson used anti-vacuum valves downstream in a penstock tunnel to prevent severe cavitation. The CFD flow domain extended from about 58 diameters (D) upstream and 15D downstream to ensure fully developed flow conditions. Tetrahedral elements were used on the valve face to best model the butterfly valve features. Consequently, the number of cells in the domain ranged from 2.2 million to 220 million. Henderson favored the Shear Stress Transport (SST) turbulence modeled and found that for valve angles greater than 20 degrees, the flow downstream from the valve was dominated strongly by unsteady vortical disturbances. An estimated eddy shedding frequency of about 1.3 Hz was estimated. Cases were run in which the CFD models had a symmetrical boundary to improve solution time and one in which the whole model was used for a steady and transient solution, respectively. The main difference manifested between the full and symmetry models was that the whole model was able to show the eddy shedding alternate between sides, while the torque coefficients and flow patterns remained unchanged overall. While the overall pattern of the predicted torque characteristics are similar to the experimental data, they differ by over 25% in many mid-valve positions. Henderson concluded that better field measurements, including the flow rate, could improve the modeling of the CFD boundary conditions.

Cheiworapuek et al. [17] investigated incompressible turbulent flow past a butterfly valve at 15, 30, 45, 60 and 90 degree opening angles. The CFD code FLUENT was used to validate experimental data for butterfly valves having diameters of 150 and 300 mm. The

number of elements used in the simulation ranged from 1.1 million to 1.4 million. The k-ϵ turbulent model was used. For the experiment, pressure taps were located 1D upstream and 14D downstream. Cheiworapuek observed that vortices were found near the tips of the butterfly valve and became larger as the valve disk was oriented at more closed positions. The loss coefficient was generally unaffected by a change in inlet velocity for a given disk orientation. Large differences between the experimental data and simulation results were on the order of 50% for loss coefficients and torque.

Feng et al. [18] used a general purpose CFD code with a k-ϵ turbulence model to study cavitation and flow characteristics of a 1.2 meter diameter double eccentric butterfly valve. A hybrid mesh of quadrilateral and triangular elements were used. The flow domain extended from five diameters upstream to about ten diameters downstream. Feng found that a double eccentric structure had improved dynamic response and self-sealing in comparison with a single or no offset butterfly valve.

While many have researched butterfly valves over the years, the following comparison study will seek to contribute insight into the use of CFD to predict butterfly valve performance factors, especially in specifying the level of agreement that can be expected at various valve opening angles, and discuss meshing methods to improve results.

1.2 Butterfly Valve Attributes

Many butterfly valves have asymmetrical features and thus their direction of installation, commonly referred to as a seating direction, typically affect the valve's flow characteristics. Butterfly valves can be installed in one of two directions: seated upstream and seated downstream. Seated upstream signifies that the valve seat, where the valve seals off flow when fully closed, is upstream of the valve disk shaft or axis of rotation. Seated downstream signifies that the valve seat is downstream of the valve disk shaft or axis of rotation. A layout of the butterfly valve for the present configuration (seated downstream) and opening angle definition, θ, can be seen in Fig. 1.1. The port diameter of a seated downstream butterfly valve is defined as the diameter of the main valve body as it leaves the main valve body and enters into the pipe diameter in which it is installed. Figure 1.2

further shows the main features and components of the butterfly valve used in this paper. Components that are considered dynamic and move with the rotation of the main disk body are the following listed in Fig. 1.2: bottom and top shaft, rubber seal, seal ring retainer, and retainer bolts. The rest are static components. Epoxy bonds the seating ring onto the main valve body. The top and bottom sleeves help secure their corresponding shafts to the main valve and disc body. The rubber seal is fastened tight onto the main disc body by means of the seal ring retainer and corresponding bolts. The rubber seal ensures a tightly closed valve when fully closed.

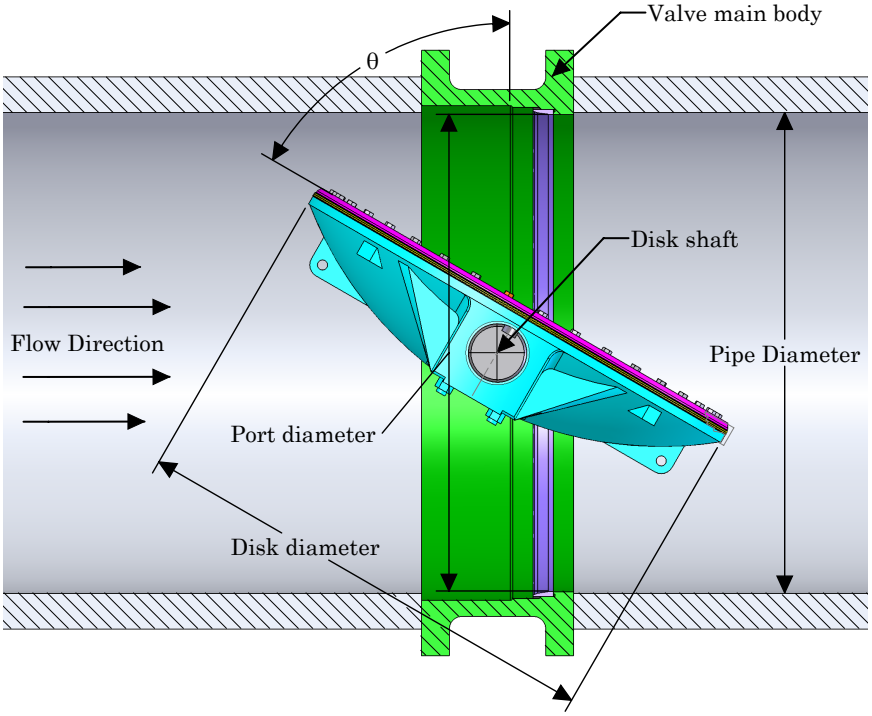

Fig. 1.1: Cross-section of a 48-inch butterfly valve installed in a pipeline in the seated downstream position and open at an angle, θ.

1.3 Butterfly Valve Performance Factors

Characterizing a butterfly valve typically involves evaluating the most common performance factors such as: pressure drop across the valve, hydrodynamic torque, flow coefficient,

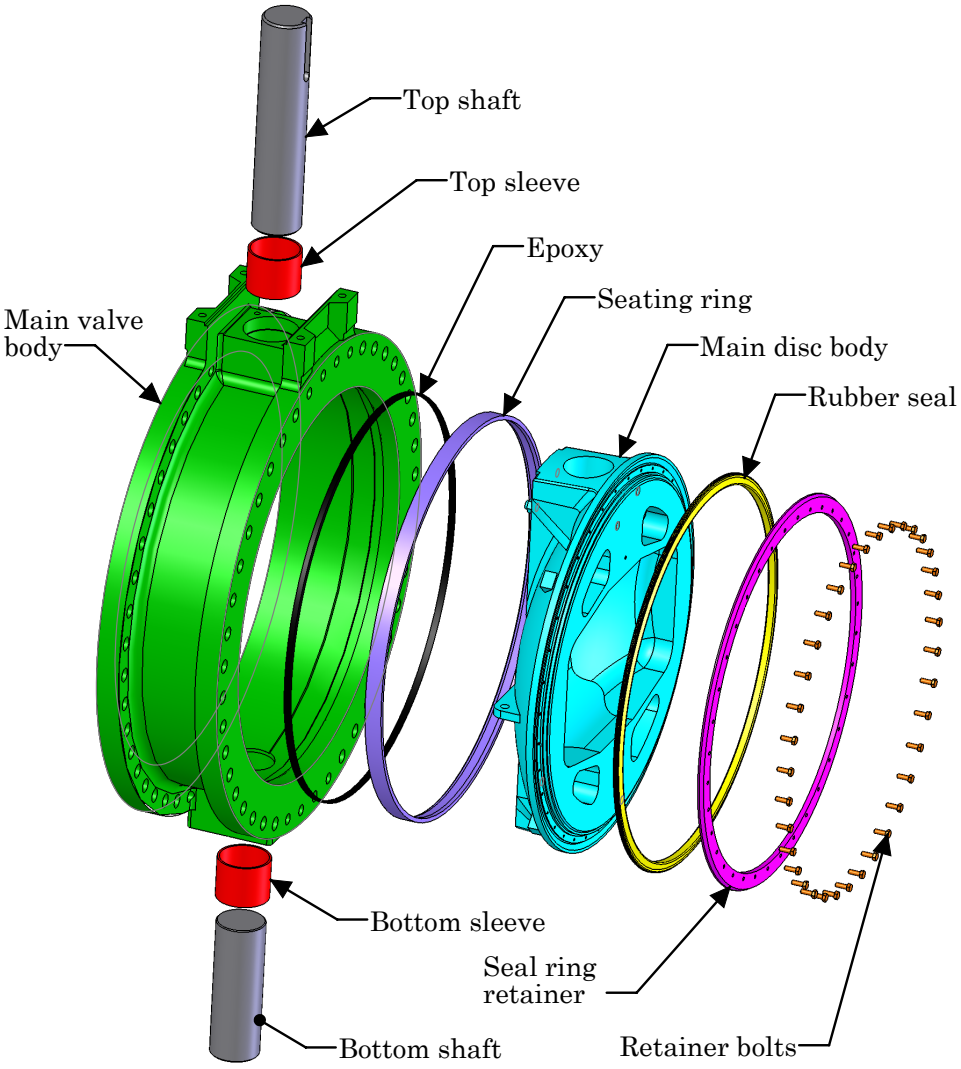

Fig. 1.2: Exploded view of the components of a 48-inch butterfly valve.

loss coefficient, and the torque coefficient. These performance factor standards have been widely published by Bosserman and AWWA [19] and will be described in subsequent paragraphs.

1.3.1 Pressure Loss

Pressure loss across a valve is often attributed to disruptions caused in the flow field such as obstruction, flow separation and mixing. For butterfly valves, pressure losses vary depending on the disk angle configuration, θ, and flow rate, Q. The pressure loss is represented by the absolute pressure differential between the measured pressure upstream, $P_{u\theta}$ and the measured pressure downstream, $P_{d\theta}$, as given in Eqn. 1.1 below:

$$\Delta P_\theta = P_{u\theta} - P_{d\theta} \tag{1.1}$$

For a given flow rate, pressure losses will generally decrease as the valve's opening angle increases due to less interference in the flow. In this study, the upstream and downstream pressures were measured at a point two diameters upstream and six diameters downstream, respectively, per AWWA guidelines [19]. It should also be noted that this pressure loss represents a gross measurement instead of net measurement. This means that head losses due to pipe friction length between measurement points (which are minimal), are included in the ΔP_θ measurements, and thus affect other performance factors to be discussed.

1.3.2 Hydrodynamic Torque

The sign convention used in this study is for torque around the valve shaft (axis of rotation) to be positive when flow acts to close the valve, such that a positive torque is required to keep the valve open. Measurement of hydrodynamic torque requires measuring the total opening and closing torque, $T_{to\theta}$ and $T_{tc\theta}$, respectively, as demonstrated below and described later in the experimental setup section.

Total Opening and Closing Torque

The total opening and closing torques can be defined as follows in equations 1.2 and 1.3:

$$T_{to\theta} = T_{d\theta} + T_{b\theta} + T_{cg\theta} + T_p, \tag{1.2}$$

$$T_{tc\theta} = T_{d\theta} - T_{b\theta} - T_{cg\theta} - T_p, \tag{1.3}$$

where $T_{d\theta}$ is the hydrodynamic torque, $T_{b\theta}$ is the bearing torque, $T_{cg\theta}$ is the center of gravity torque, and T_p is the packing and hub torque. These various torques will be briefly described below.

Bearing Torque ($T_{b\theta}$)

The bearing torque, $T_{b\theta}$, in a butterfly valve is the frictional resistance to rotation imposed on the valve shaft by the bearings. Its value is highest at the near-closed position because of the high differential pressure when the valve is nearly closed. Bearing torque reduces to nearly zero as the valve reaches the fully open position and always acts in the opposite direction to the valve's movement. It is defined in Eqn. 1.4:

$$T_{b\theta} = \frac{\pi {D_d}^2 \Delta P_\theta d_s C_f}{8}, \tag{1.4}$$

where D_d is the disk diameter, ΔP_θ is the pressure drop while at the disc angle θ, d_s is the shaft diameter, and C_f is the coefficient of friction between the shaft and bushing.

Center of Gravity Torque ($T_{cg\theta}$)

Center of gravity torque, $T_{cg\theta}$, is caused by the offset center of gravity of the disc and occurs when the valve shaft is located in or near the horizontal plane. This torque is often assumed as insignificant, which in the case of this study is deemed valid since the stem is in the vertical position. Center of gravity torque is defined in Eqn. 1.5 as:

$$T_{cg\theta} = S_c W_d C_g \cos(\theta + \gamma), \tag{1.5}$$

where S_c is the sign convention variable, W_d is the weight of valve disc, C_g is the valve disc center of gravity distance from the shaft centerline, θ is the valve opening position angle where closed=0 degrees and fully open=90 degrees, and γ is the center of gravity offset angle in non-symmetric disc designs [19].

Packing and Hub Torque (T_p)

The packing and hub torque is due to friction between the shaft seal and the valve shaft, and the friction between the disc and/or shaft and the body hub seal where the shaft penetrates the pressure boundary. The packing and hub torque always acts in the opposite direction to the valve's movement and is defined below in Eqn. 1.6:

$$T_p = C_{pck} d_s, \tag{1.6}$$

where C_{pck} is a packing coefficient [19], and d_s is the valve shaft diameter.

Hydrodynamic Flow Torque ($T_{d\theta}$)

The hydrodynamic flow torque is due to the effects of the internal fluid media (water in this case) or gravity acting on the valve at any given opening angle, θ. Hydrodynamic flow torque is necessary to compute flow characteristics and the torque coefficient for the valve, and in determining motor requirements for operating the butterfly valve. Combining Eqns. 1.2 and 1.3 yields the hydrodynamic torque given in Eqn. 1.7 due to cancellation of terms:

$$T_{d\theta} = \frac{T_{to\theta} + T_{tc\theta}}{2}. \tag{1.7}$$

1.3.3 Flow Coefficient

The valve flow coefficient, $C_{v\theta}$ is a measure of the flow rate of water through a valve at 60° F at a pressure drop of 1 psi (lb/in^2) and is customarily presented in units of gpm/psi$^{1/2}$ as seen in Eqn. 1.8 below:

$$C_{v\theta} = Q\sqrt{\frac{SG}{\Delta P_\theta}}, \tag{1.8}$$

where Q is the flow rate in gpm, SG is the specific gravity of the fluid in use, and ΔP_θ is the pressure drop across the valve in psi. The valve flow coefficient is useful to manufacturers and users in understanding the flow capacity of valves.

1.3.4 Loss Coefficient

The flow resistance coefficient, commonly known as the loss coefficient, K_θ, is a dimensionless value commonly used in the design of thermal fluid systems to predict head losses present due to the presence of various components. The loss coefficient is shown below in Eqn. 1.9:

$$K_\theta = \frac{2gh_{L\theta}}{{V_{avg}}^2}, \tag{1.9}$$

where g is the gravity constant of 9.81 m/s, $h_{L\theta}$ is the head loss between any two reference points in a system, and $V_{avg} = QA$ is the average velocity of the fluid flow, where Q is the flow rate, and A is the cross-sectional area of flow. The head loss, $h_{L\theta}$, is further defined in Eqn. 1.10 below:

$$h_{L\theta} = \frac{\Delta P_\theta}{\rho g}, \tag{1.10}$$

where ΔP_θ is the pressure loss measured across the points previously described, and ρ is the density of the fluid in use. Substituting Eqn. 1.10 into Eqn. 1.9 and simplifying gives Eqn. 1.11 as seen below:

$$K_\theta = \frac{2\Delta P_\theta}{\rho {V_{avg}}^2}. \tag{1.11}$$

1.3.5 Torque Coefficient

The torque coefficient, $C_{t\theta}$, is a dimensionless quantity used by manufacturers and users to determine the torque and power requirements of valves scaled relative one to another. Torque coefficient is defined in Eqn. 1.12 as:

$$C_{t\theta} = \frac{T_{d\theta}}{D_d^3 \Delta P_\theta}. \tag{1.12}$$

Chapter 2

Experimental Setup and Results

Utah State University (USU) was contracted to conduct performance tests at the Utah Water Research Laboratory (UWRL) on a 48-inch butterfly valve. The valve was installed in the seated downstream position in a 47.25 inch internal diameter steel pipe line as seen in Fig. 2.1. A flowchart regarding the experimental setup can be seen in Fig. 2.2. Flow was regulated upstream using a control valve to ensure a fully developed flow profile before traveling a length of 15 diameters (D) to encounter a 48-inch Venturi flowmeter, which was used to measure the volume flow rate, Q. Further downstream an additional 15D from the Venturi flowmeter, a pressure tap was installed. The pressure tap was used to measure the pressure, $P_{u\theta}$, 2D upstream from the butterfly valve which was configured with linear strain gages. During the experiment, the butterfly valve was opened and closed under each set of flow conditions in order to measure the total opening and closing torques, $T_{to\theta}$ and $T_{tc\theta}$, using the installed strain gages. Six diameters downstream from the butterfly, another pressure tap was installed to measure the pressure, $P_{d\theta}$. Beyond the downstream pressure tap, the flow line extended an additional 15D before reaching another control valve, and then out to atmospheric conditions.

The temperature of the water used in the experiment varied little at an average of 48.6 °F, which gives the following fluid properties: $SG = 1.0007$ for the specific gravity, and $\nu = 1.45 * 10^{-5}$ ft^2/sec for the kinematic viscosity. Using these values combined with the five directly measured values of Q, $P_{u\theta}$, $P_{d\theta}$, $T_{to\theta}$, and $T_{tc\theta}$, the following flow performance factors from section 1.3 were calculated for the butterfly valve: pressure drop (ΔP_θ), hydrodynamic torque ($T_{d\theta}$), flow coefficient ($C_{v\theta}$), loss coefficient (K_θ), and the torque coefficient ($C_{t\theta}$). These values and performance measurements were performed and calculated for nine different valve degree angle openings, from $\theta = 10$ degrees to $\theta = 90$ degrees in 10 degree

increments. The instrumentation used to take the measurements will be briefly described, followed by a review of the instrumentation uncertainty of directly measured values and the uncertainty of the flow performance factors.

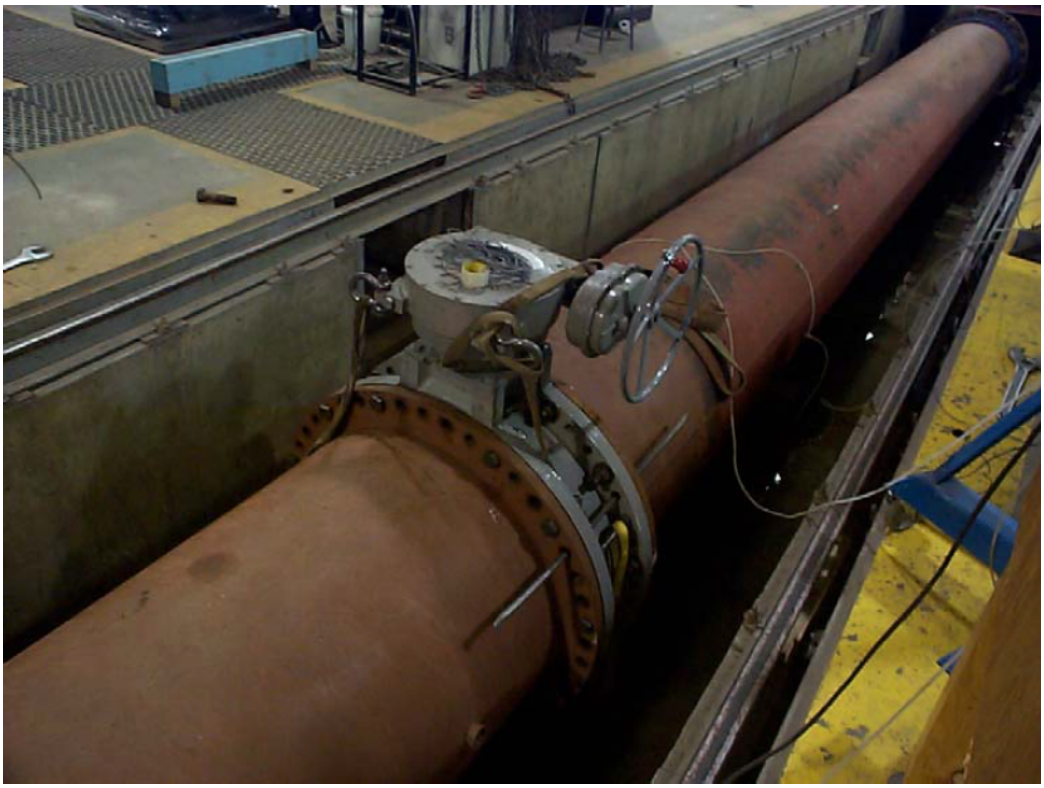

Fig. 2.1: Example of a butterfly valve installed in a pipeline at the UWRL.

2.1 Instrumentation

Using the setup previously described, five flow configuration properties were directly measured using instrumentation installed in the experimental system: a venturi flowmeter, pressure taps, and strain gages. These will now be briefly discussed.

Venturi flowmeters are considered to be very accurate flowmeters. They are generally characterized by their gradual contraction and expansion, which prevents flow separation and swirling. They only suffer frictional losses on the inner wall surfaces and cause very

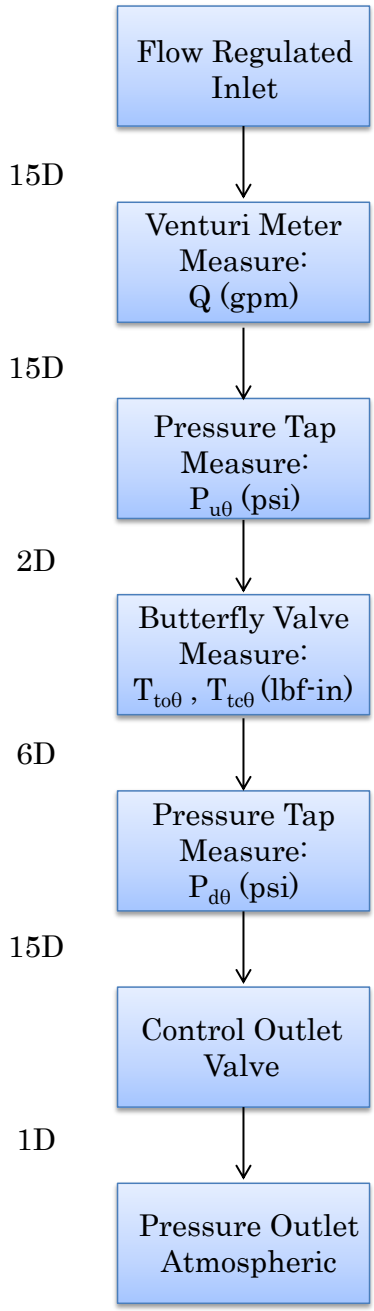

Fig. 2.2: Flowchart of the experimental setup and measured values.

low head losses. Figure 2.3 shows a cross-section of a Venturi flowmeter. By using the assumptions of the Bernoulli and continuity equations [20], Venturi flowmeters can measure the volume flow rate. The relative uncertainty of the 48-inch Venturi flowmeter used in this experiment was $U_Q/Q = 0.25\%$.

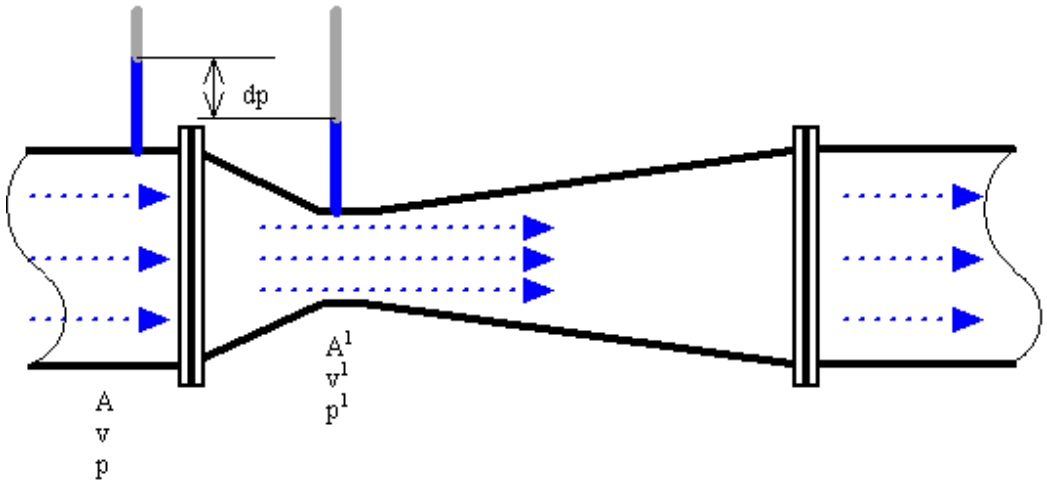

Fig. 2.3: Interior cross section of an axisymmetrical Venturi flowmeter.

Pressure taps are commonly used in piping systems to take differential measurements of pressure. This is done by drilling prescribed holes through the pipe wall and welding the tap fittings into the drilled hole such that the tapped fitting is flush to the interior of the pipe wall, so as not to interfere significantly with the fluid flow. Once this is done for another pressure tap, a pressure transducer is connected to both pressure taps, allowing the transducer to take a differential measurement of the two. The relative uncertainty of the pressure transducer used in this experiment was $U_{\Delta P_\theta}/\Delta P_\theta = 0.25\%$.

Torque strain gages are used by installing thin strain gages onto cylindrical surfaces that will undergo torsion. Using the stress-strain relationship of a known material and calibrating the strain gages, the torque can be calculated. For this experiment, calibrated linear strain gages were installed on the butterfly valve shafts. For each set of flow conditions associated

with the valve degree opening, an actuator cycled the butterfly valve to completely open and closed positions numerous times in order to measure the total opening and closing torques. The relative uncertainty of these measurements using the strain gages was $U_{T_{to\theta}}/T_{to\theta} = U_{T_{tc\theta}}/T_{tc\theta} = 3\%$.

2.2 Experimental Results

Results for the described experiment were provided by the UWRL. The directly measured flow values are provided in Table 2.1. The calculated flow performance factors are provided in Table 2.2 along with Reynolds numbers for each respective flow.

Table 2.1: Directly measured flow values recorded at various butterfly valve degree openings.

θ (deg.)	Q (gpm)	$P_{u\theta}$ (psi)	$P_{d\theta}$ (psi)	$T_{o\theta}$ (lbf-in)	$T_{c\theta}$ (lbf-in)
10	6229.3	14.00	3.95	12965	-2086
20	14343.1	13.80	5.71	18488	6025
30	23941.3	13.45	7.25	23154	13785
40	35999.5	12.70	8.25	30341	23459
50	54967.6	10.70	6.94	43670	38134
60	69166.1	8.80	6.45	48675	44021
70	79804.3	7.10	5.23	45694	42060
80	90501.3	5.15	3.63	43933	39840
90	93559.1	4.55	3.59	28330	21544

Table 2.2: Calculated flow performance factors at various butterfly valve degree openings.

θ (deg.)	V_{avg} (ft/s)	Re	ΔP_θ (psi)	$T_{d\theta}$ (lbf-in)	$C_{v\theta}$ (gpm/psi$^{1/2}$)	K_θ	$C_{t\theta}$
10	1.14	$3.10 \cdot 10^5$	10.05	5439.5	1966.1	1148.91	0.005
20	2.62	$7.11 \cdot 10^5$	8.09	12256.5	5043.6	174.59	0.015
30	4.38	$1.19 \cdot 10^6$	6.20	18469.5	9621.0	47.98	0.029
40	6.59	$1.79 \cdot 10^6$	4.45	26900.0	17076.8	15.23	0.059
50	10.06	$2.73 \cdot 10^6$	3.76	40902.0	28362.5	5.52	0.106
60	12.66	$3.44 \cdot 10^6$	2.35	46348.0	45156.5	2.18	0.192
70	14.60	$3.96 \cdot 10^6$	1.87	43877.0	58409.9	1.30	0.228
80	16.56	$4.50 \cdot 10^6$	1.52	41886.5	73341.0	0.83	0.267
90	17.12	$4.65 \cdot 10^6$	0.96	24937.0	95438.8	0.49	0.232

2.3 Uncertainty of Experimental Results

Knowing the uncertainty in the direct measurements and the calculated flow performance factors is vital to understanding the range within which to expect errors arising from systematic and random uncertainties. Uncertainty analysis of the experimental data and calculated results provide important information regarding the possible overlap between the experiment itself and the CFD simulations. For example, if large relative uncertainties are discovered for the experimental data and if large disparities exist between the experimental and simulation results, it could be difficult to quantify the level of agreement between the two.

A common method for carrying out a general uncertainty analysis involves using the Taylor Series Method (TSM) for propagation of uncertainties [21]. This usually involves considering a result, r, as a function of several variables

$$r = r(X_1, X_2, ..., X_N). \tag{2.1}$$

The combined standard uncertainty at 95% confidence interval, U_{95}, is given as

$$U_{95} = 2\left[\sum_{i=1}^{N}\left(\frac{\partial r}{\partial X_i}\right)^2 ({b_{X_i}}^2 + {s_{X_i}}^2)\right]^{1/2}, \tag{2.2}$$

where b_{X_i} and s_{X_i} are the systematic and random standard uncertainties, respectively. A detailed general uncertainty analysis has been carried out in Appendix A for all the performance factors listed in Table 2.2. The experimental relative uncertainties are provided in Table 2.3.

Table 2.3: Experimental relative uncertainties of flow performance factors at various butterfly valve degree openings.

θ (deg.)	$V_{avg}(\%)$	$\frac{U_{\Delta P_\theta}}{\Delta P_\theta}(\%)$	$\frac{U_{T_{d\theta}}}{T_{d\theta}}(\%)$	$\frac{U_{C_{v\theta}}}{C_{v\theta}}(\%)$	$\frac{U_{K_\theta}}{K_\theta}(\%)$	$\frac{U_{C_{t\theta}}}{C_{t\theta}}(\%)$
10	0.25	0.25	3.62	0.28	0.56	3.63
20	0.25	0.25	2.38	0.28	0.56	2.39
30	0.25	0.25	2.19	0.28	0.56	2.20
40	0.25	0.25	2.14	0.28	0.56	2.15
50	0.25	0.25	2.13	0.28	0.56	2.14
60	0.25	0.25	2.12	0.28	0.56	2.14
70	0.25	0.25	2.12	0.28	0.56	2.14
80	0.25	0.25	2.12	0.28	0.56	2.14
90	0.25	0.25	2.14	0.28	0.56	2.16

Chapter 3

CFD Setup

Using general purpose CFD software STAR-CCM+[1], the previously described experiment was modeled in an attempt to simulate and predict the measured butterfly valve performance factors. The overall approach to simulating the experimental model consisted of: using a computer aided design model of the butterfly valve with appropriate cylindrical parts added to simulate pipe flow upstream and downstream of the valve, properly meshing and applying physical models to the simulation, creating appropriate flow conditions to match the experiment, such as mass flow rate, fluid properties, valve angle opening, etc., ensuring iterative and grid convergence and time independent results, and recording the predicted flow performance factors and overall flow properties. Simulations were evaluated for nine different valve degree openings from $\theta = 10$ to 90 degrees in ten degree increments, and two additional simulations for the 10, 50, and 90 degree cases with coarser meshes to investigate grid refinement.

According to Versteeg and Malalasekera [22], a large source of uncertainty in CFD modeling can result from poor representation of boundary conditions, particularly the inlet and outlet conditions for internal flow. While the outlet conditions are of less concern as discussed later on, the inlet boundary condition deserves special consideration. In order to ensure the fully developed flow conditions listed in Table 2.1 for each valve opening case, a periodic flow simulation was setup prior to simulation of the butterfly valve case and was used as the upstream boundary condition.

The periodic flow simulation for this study allowed rapid development of fully developed flow conditions by forcing a short internal turbulent flow simulation to match a specified pressure drop. By iterating the pressure drop several times, the fully turbulent

[1]STAR-CCM+ version 7.04 is a widely verified CFD software package distributed by CD-Adapco.

flow conditions of each simulation case can match the experimental flow conditions found in 2.1. The turbulent kinetic energy, turbulent dissipation rate, and velocity vectors for the periodic flow cases are then extracted and used as the necessary inlet boundary conditions of the valve simulations. This allows for exceptional representation of the inlet boundary condition values, eliminates the need for a long upstream entry length cylinder region to simulate the development of fully developed flow prior to passing into the butterfly valve, and effectively decreases the amount of time needed to iterate over a larger domain valve simulation. More details regarding the procedure can be found in Appendix B.

A brief discussion regarding computational fluid dynamics will now be presented, followed by a description in the next chapter of how butterfly valve simulations were setup using STAR-CCM+.

3.1 Computational Fluid Dynamics

Governing equations of fluid dynamics commonly referenced for incompressible isothermal fluids in CFD include the Navier-Stokes equations [23] given in conservative form using index notation as seen in Eqn. 3.1. The Navier-Stokes equations are a simplification of the conservation of momentum equations and the constitutive equations that define the relationship between shear and strain for a newtonian fluid.

$$\frac{\partial u_i}{\partial t} + \frac{\partial}{\partial x_j}(u_j u_i) = -\frac{1}{\rho}\frac{\partial p}{\partial x_i} + \nu \frac{\partial^2 u_i}{\partial {x_j}^2} \tag{3.1}$$

While many laminar solutions (low Reynolds number flows) are possible using Eqn. 3.1, nonlinearities and instability arise due to turbulence. Turbulence is often characterized as irregular and random flow, with three-dimensional vortical fluctuations. Most methods of analyzing turbulence results in more unknowns than available equations, and thus results in an equation closure problem. Some techniques used include focusing on the mean flow and the effects of turbulence on mean flow properties by using what are called the unsteady Reynolds-averaged Navier-Stokes (RANS) equations [22] as given in Eqn. 3.2 using index

notation:

$$\frac{\partial \overline{u_i}}{\partial t} + \overline{u_j}\frac{\partial \overline{u_i}}{\partial x_j} = \frac{1}{\rho}\frac{\partial}{\partial x_j}(-\overline{p}\delta_{ij} + \mu\frac{\partial \overline{u_i}}{\partial x_j} + \tau_{ij}^{'}), \tag{3.2}$$

where $\tau_{ij}^{'}$ is the Reynolds stress tensor that attempts to describe the diffusive nature of turbulence as defined in Eqn. 3.3 .

$$\tau_{ij}^{'} = -\rho\overline{u'_i u'_j} = -\rho \begin{bmatrix} \overline{u'^2} & \overline{u'v'} & \overline{u'w'} \\ \overline{v'u'} & \overline{v'^2} & \overline{v'w'} \\ \overline{w'u'} & \overline{w'v'} & \overline{w'^2} \end{bmatrix} \tag{3.3}$$

However, in order to compute turbulent flows with the RANS equations, it is necessary to develop turbulence models to predict the Reynolds stresses and have closure.

Some of the most common turbulence models include: mixing length, Spalart-Allmaras, k-ϵ, k-ω, algebraic stress, and Reynolds stress. While each turbulence model has its strengths, weaknesses, and variations, this study will focus on using the k-ϵ model only. Reasons for choosing the k-ϵ turbulence model include the following: simple turbulence model to use for which only initial and/or boundary conditions need to be supplied, excellent performance for many industrially relevant flows, and well established as the most widely validated turbulence model [22]. Since the initial and/or boundary conditions are only required, they can be easily extracted from the periodic flow cases with ease as mentioned earlier in this chapter.

While many variations of the k-ϵ turbulence model are commonly used, they all derive from the standard k-ϵ model. The standard k-ϵ model uses the following transport equations for the turbulent kinetic energy, k, and turbulent dissipation rate, ϵ, respectively:

$$\frac{\partial}{\partial t}(\rho k) + \frac{\partial}{\partial x_j}(\rho k u_j) = \frac{\partial}{\partial x_j}\left[\left(\mu + \frac{\mu_t}{\sigma_k}\right)\frac{\partial k}{\partial x_j}\right] + 2\mu_t S_{ij}S_{ij} - \rho\epsilon \tag{3.4}$$

$$\frac{\partial}{\partial t}(\rho \epsilon) + \frac{\partial}{\partial x_j}(\rho \epsilon u_j) = \frac{\partial}{\partial x_j}\left[\left(\mu + \frac{\mu_t}{\sigma_\epsilon}\right)\frac{\partial \epsilon}{\partial x_j}\right] + C_{1\epsilon}\frac{\epsilon}{k}2\mu_t S_{ij}S_{ij} - C_{2\epsilon}\rho\frac{\epsilon^2}{k} \tag{3.5}$$

where $C_{1\epsilon}, C_{2\epsilon}, C_{\mu}, \sigma_k$, and σ_ϵ are empirical constants and μ_t, the turbulent viscosity, is modeled as

$$\mu_t = \rho C_\mu \frac{k^2}{\epsilon}. \tag{3.6}$$

Versteeg and Malalasekera provide additional information regarding the formulation and calculation of these transport equations [22].

Chapter 4

Meshing

In order to numerically solve the RANS equations from Chapter 3, it is necessary to discretize or partition a normally continuous medium into discrete volumetric cells, which consist of vertices and faces. A vertex is a point in space defined by a position vector as seen in Fig. 4.1. A number of vertices can be used to define a feature curve or a face. A feature curve in its most basic terms consists of two vertices that define a line in two dimensional space. A face defines a surface in three-dimensional space with four or more faces being used to define a three-dimensional cell. All of the volumetric cells combined are what is called a volume mesh.

In a numerical simulation, a volume mesh represents the mathematical description of the space or geometry of the problem being solved. In this study using CFD, the volume mesh represents the entire simulated flow field inside the experimental continuum previously described in Chapter 2. By solving the RANS equations using CFD, flow properties existent at each discrete volumetric cell such as the velocity, pressure, turbulence, etc. will attempt to simulate the experimentally measured values individually and as a whole. As the mesh is refined to better represent more discrete cells in the flow domain, the ability of CFD to simulate and predict the real life conditions improves. However, the trade off of a larger amount of cells to compute is often undesirable due to a lack of computational resources.

The meshing process in STAR-CCM+ involves creating a mesh continua for the continuum that one is attempting to model, selecting correct meshing models, making any changes to mesh sizing parameters and/or attributes globally and/or locally, setting volumetric controls, and running the surface and volume mesh generators. Checking the quality of the mesh by inspection and diagnostic tools usually follows as well as some iterations to get the correct sizing parameters for the specific simulation.

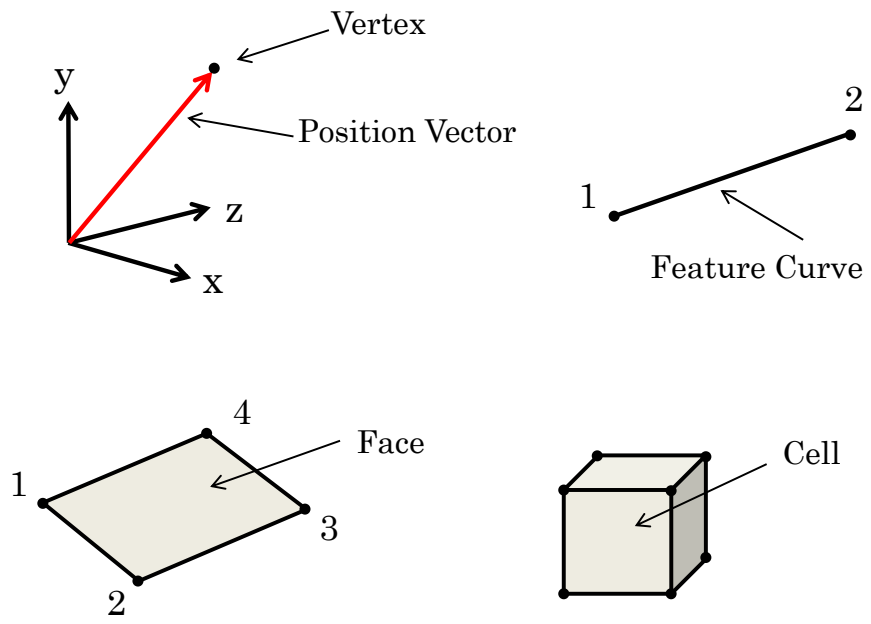

Fig. 4.1: Illustration of the individual components of a volume mesh.

4.1 Geometry Import and Tessellation

After being provided with the appropriate computer aided drafting (CAD) model of the butterfly valve used in the experiment, as seen in Fig. 1.2, the CAD model was imported into STAR-CCM+ and re-tessellated with a very fine level of surface refinement as seen in Fig. 4.2. Tessellation is the process in which the surfaces of three-dimensional models are represented using triangles. A coarse tessellation level for complex geometries will typically produce a poor representation of the curved and intricate features of any CAD model. A finer level of tessellation will typically preserve the desired surface curvatures and features of a CAD model with a trade off of requiring more triangles to represent it.

After tessellation, CAD model components were assigned as parts. Two cylindrical parts, representing the piping upstream and downstream in the experiment, were added to each end of the valve. The seated downstream position for the butterfly valve was used to match the experiment. Each cylinder has an inner diameter of 47.25 inches to match

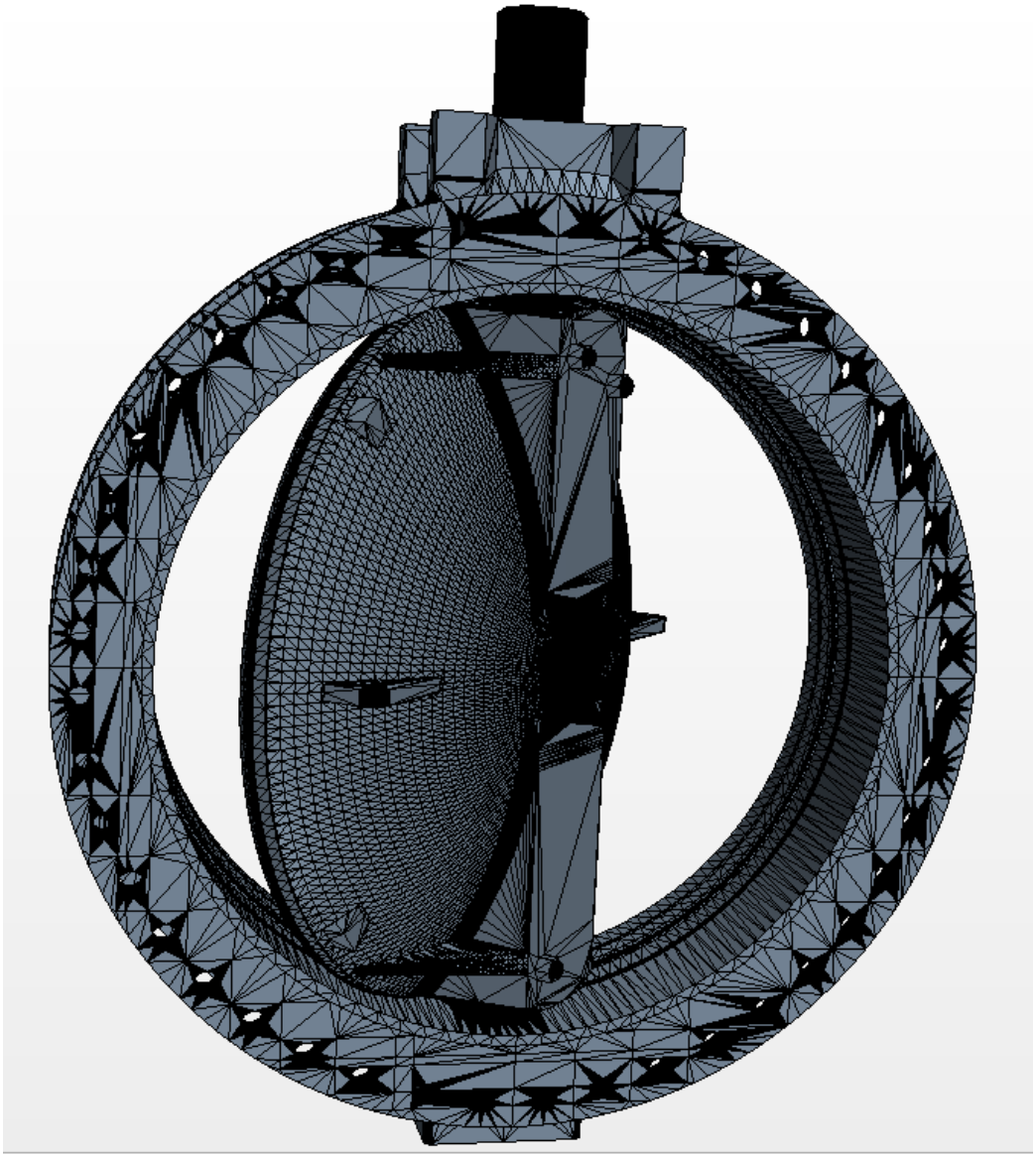

Fig. 4.2: Example of a tessellated butterfly valve at 50 degree open position.

the nominal inner diameter of the steel pipe used in the experiment. One cylinder extends approximately two and a half times the inner diameter (2.5D) upstream from the valve.

This significantly shortened upstream entry length, prior to reaching the valve, is justified by using a periodic flow simulation to determine the appropriate fully developed flow conditions that should be existent at the inlet face before approaching the butterfly valve in the pipe line. Upon convergence and correct matching of volume flow rates between the periodic simulations and the measured experiments of Table 2.1, the necessary values for the inlet boundary conditions of this study, such as the velocity, turbulent kinetic energy, and turbulent dissipation rate, were extracted from the periodic simulations and mapped onto the inlet for the 2.5D long upstream cylinder. Additional information regarding the periodic simulation technique used in this study can be found in Appendix B.

Another cylinder extends approximately 6.5D downstream from the valve. The downstream domain extends an additional 5.5D approximately by using a meshing extrusion technique which will be discussed later on. This brings the total length of the downstream domain from the valve to nearly 12D. This length downstream from the valve was chosen to ensure that the assumed boundary conditions of a fully developed flow outlet were as valid as possible as will be later discussed.

Next, each cylinder's combined surfaces were split into three surfaces: side, top, and bottom, where the side represents the interior walls of the pipe, and the top or the bottom could be the mating surface connecting into the butterfly valve geometry or the inlet or outlet. In order to have a flow domain from an inlet connect into the upstream cylinder to the valve and then to the downstream cylinder leaving to an outlet, a top or bottom surface was removed with its opposite side connecting into the valve for each cylinder. Figure 4.3 shows an example of an upstream cylinder connecting into a butterfly valve in the seated downstream position. The face connecting to the valve has been removed, and the dark colored face on the left represents the inlet boundary for the domain. The downstream cylinder was manipulated in similar fashion. After all of the aforementioned parts were defined and created, they were assigned to a region continuum.

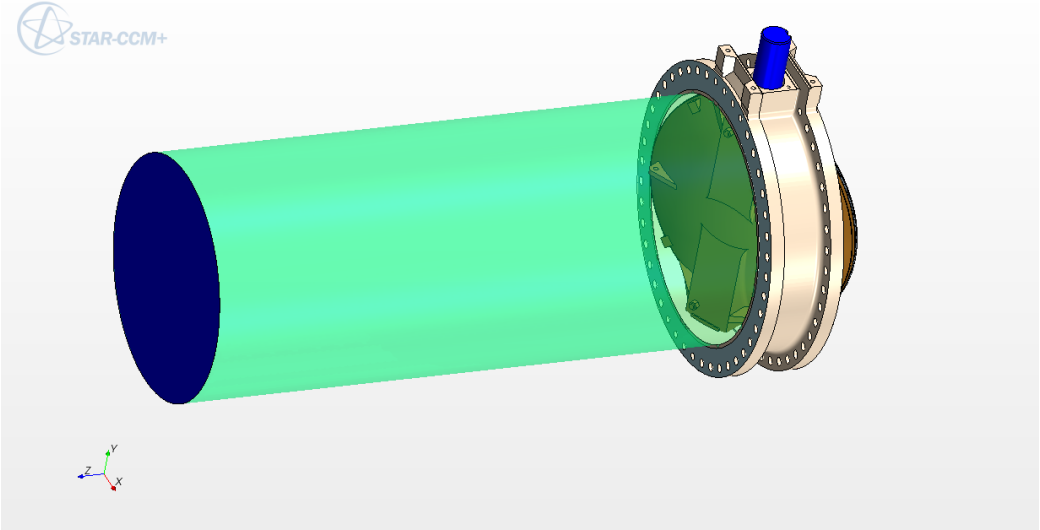

Fig. 4.3: Demonstration of upstream cylinder with velocity inlet boundary added onto the butterfly valve at partially opened position.

4.2 Boundary Conditions

In three dimensions, boundaries are surfaces that completely surround and define a region. Each boundary has its own properties and can be given custom configurations such as meshing surface size, or how it should behave relative to other surfaces. The main boundary types chosen were the following: wall, internal interface, velocity inlet, and flow outlet. These boundaries and their corresponding chosen surfaces for this study, will now be discussed.

4.2.1 Wall

A wall boundary represents an impermeable surface. For simulations with viscous flow such as this one, it also represents a no-slip boundary. All of the following surfaces were chosen as wall boundaries except: the upstream inlet face, the downstream outlet face, and the interface connecting the downstream cylinder to the extruded cylinder portion as seen in Fig. 4.4. All valve faces were assumed to be smooth by inspection at the time of the experiment, and therefore required no modifications to surface roughness. All other

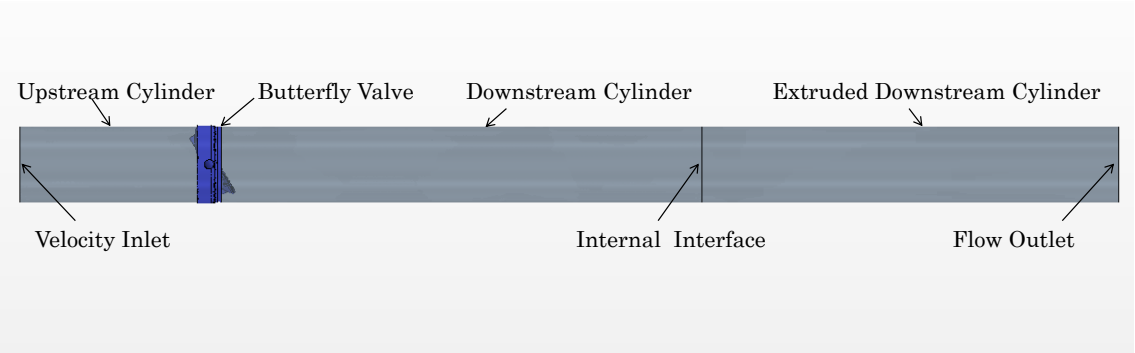

Fig. 4.4: Illustration of boundaries and components of the butterfly valve simulations.

walls, constituting the interior walls of the upstream cylinder and all connected downstream cylinders were modified with a rough wall surface specification and roughness height of 0.0024 inches to match the steel pipe conditions of the experiment. All other wall roughness parameters were left as default.

4.2.2 Internal Interface

The internal interface joins two regions within the same continuum and can be used to combine together separate regions from the same continuum for in-place or periodic interfaces. When the extrusion process takes place, an internal interface boundary is automatically created between the outlet of the original 6.5D downstream cylinder and the inlet of the newly extruded 5.5D cylinder portion. This internal interface will cause the two sections to behave as one continuous flow region with no interruption in the fluid flow.

4.2.3 Velocity Inlet

A velocity inlet boundary represents the inlet of a duct at which the flow velocity is known. The upstream cylinder inlet face was selected as such. For the velocity inlet boundary, the velocity must be specified by the user, as well as the turbulent dissipation rate and the turbulent kinetic energy when using the k-ϵ turbulence model, which was the case in this study. These values were extracted from the periodic flow simulations previously

discussed and were mapped onto this boundary using their corresponding coordinates.

4.2.4 Flow Split Outlet

The flow split outlet boundary represents the outlet of a duct and can allow flow split fractions in which the user can specify the percentage of flow leaving multiple ducts. In this study, that value is set to unity for the downstream outlet face of the extruded cylinder. Additionally, flow properties such as velocity, turbulence qualities, etc. are forced to have zero gradients normal to the outflow face. In order to properly apply this boundary condition, the pipe length downstream from the installed butterfly valve must be long enough that the flow has become fully developed so as not to prematurely force the flow to a zero gradient condition.

For instance, most flow manufacturers recommend installing their flow meters 10D to 20D downstream of any valve because swirling turbulent eddies generated by valves largely disappear and the velocity flow profile returns to fully developed [20]. Huang [8] compared how flow profiles changed for CFD simulation by forcing the zero gradient condition on the outlet for a butterfly valve simulation for different exit lengths. It was observed that in changing the exit length of the pipe downstream from 8D to 9D, a 2% difference was recorded. For this study, no significant differences were observed between simulation cases run initially with 15D exit lengths compared to 12D exit lengths. Consequently, a length of approximately 12D was used in order to simplify the flow model and computational requirements.

4.3 Meshing Models and Options

Once the region continuum and boundaries are setup correctly, the meshing models can be set. The main meshing models selected were the following: polyhedral mesher, extruder, prism layer mesher, surface wrapper, and the surface remesher. An explanation of each meshing model as well as selected parameters and options for this study will be described. Further explanations can be found in Appendix C and also in the STAR-CCM+ user's manual [24].

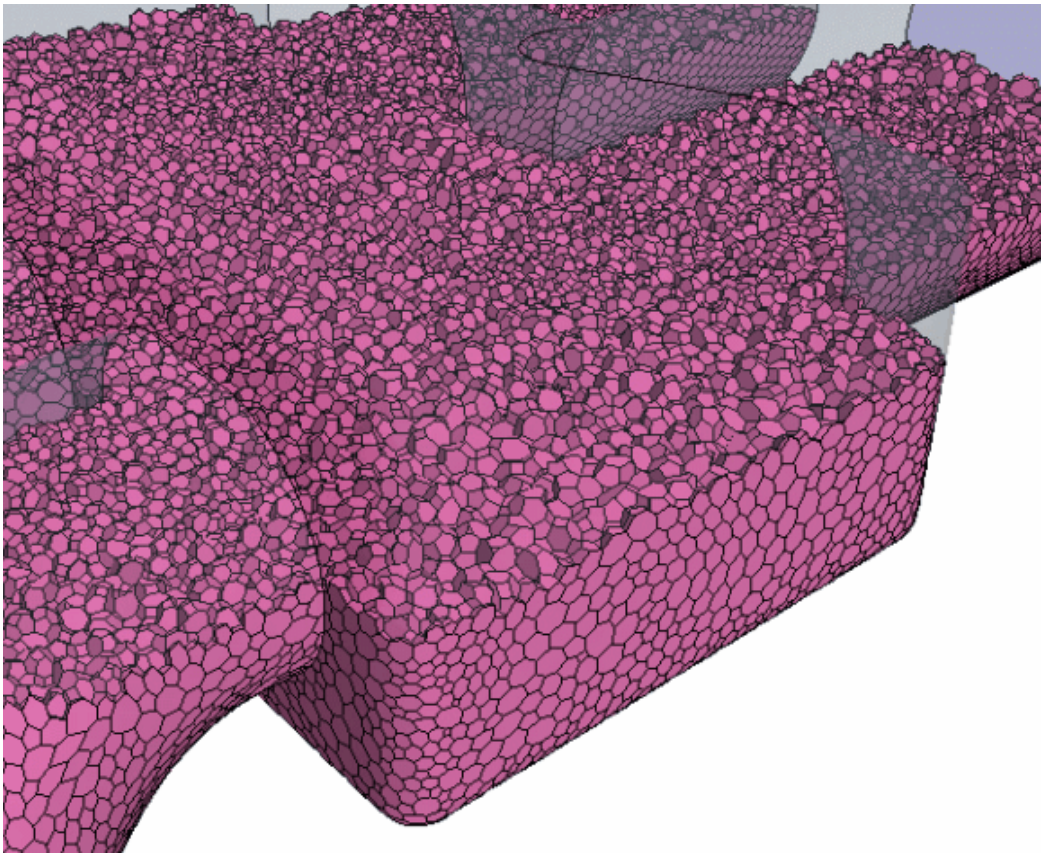

Fig. 4.5: Illustration of polyhedral volumetric cells in a mesh.

4.3.1 Polyhedral Mesher

The polyhedral mesher is a core volume mesh model that dictates the main aspects of the entire mesh to be constructed. Polyhedral cells created typically have an average of 14 cell faces and provide a balanced solution. A large advantage that the polyhedral meshing model has compared to tetrahedral meshes is that they are relatively easy and efficient to generate, and contain approximately five times fewer cells than a tetrahedral mesh, thus alleviating computational burdens. Figure 4.5 shows an example of what polyhedral cells look like in a typical volume mesh. The run optimizer option for the polyhedral mesher was also enabled.

4.3.2 Extruder

As previously mentioned, an extruded portion of the downstream cylinder extending approximately 5.5D beyond the original downstream cylinder was to be constructed during the meshing process as illustrated in Fig. 4.4. The extruder mesher model allows a boundary located in a region continuum to be extended beyond its originally constructed bounds. This is particularly useful since the extended domain can be produced as orthogonal extruded cells which are ideal in steady flows such as internal flow in a pipe. By creating orthogonal extruded cells in a significant portion of the domain, the computational expenses are much less in comparison to using a polyhedral mesher to construct the same region. The frozen boundaries and check validity options were also selected to prevent the extruded boundary from shifting and to error check problems with the extrusion. Before meshing, the extrusion parameters at the boundary of extrusion must be chosen. The following parameters were selected: average normal extrusion, 80 layers of extrusion, stretching extrusion magnitude of six, and a magnitude of 260 inches ($\approx$ 5.5D), with a new region being created for the extrusion as part of the continuum.

4.3.3 Prism Layer Mesher

The prism layer mesher model is used to generate orthogonal prismatic cells next to wall boundaries. This layer of cells helps resolve the boundary layer and improve the accuracy of the flow solution. By default, they are created only on wall boundary types. The default options that were selected for the prism layer mesher include: geometric progression for the stretching function, stretch factor for the stretching mode, a gap fill percentage of 25%, a minimum thickness percentage of 10%, a layer reduction percentage of 50%, a boundary march angle of 50 degrees, a concave angle limit of zero, a convex angle limit of 360 degrees, a near core layer aspect ratio of 1, and the improve subsurface quality option selected.

4.3.4 Surface Wrapper

The surface wrapper is typically used to provide a closed, manifold, non-intersecting surface and is used for imported surfaces that include the following: multiple intersecting

parts, missing data in the form of holes and gaps, surface mismatches, double and internal surfaces, and overly complex geometry with too much detail. The curvature and proximity refinement options were also selected. The resulting surface quality from the surface wrapper is not optimal so it is commonly used with the surface remesher to provide a high quality starting surface for the core volume mesher. Because the CAD geometry of the butterfly valve involves multiple parts with narrow gaps, such as between the valve and the disc, the surface wrapper was chosen to help alleviate meshing issues.

Figures 4.6 and 4.7 show the undesirable intersection that can occur between the butterfly valve main body and the disk after meshing. Figure 4.7 shows a close up view of the intersection. Such intersections in narrow gaps misrepresent the valve's geometry. In particular, this misrepresentation could cause a higher predicted pressure drop and affect the flow simulation results. Figures 4.8 and 4.9 demonstrate a proper application of using the surface wrapper with no unintended intersections. Setting the surface wrapper involves first adding a contact prevention set under the fluid continuum's mesh values node. Once a contact prevention set is added, two sets of boundaries for which to prevent intersection must be set, including a search floor. For the first set of boundaries, the following regions were selected: epoxy, main body, ring body seat. The second set of boundaries including the following regions: main disc body, ring retainer, and rubber seal, shaft top, and shaft bottom. The search floor was set to 0.001m.

4.3.5 Surface Remesher

The surface remesher model is used to retriangulate surfaces as needed to improve the overall quality of an existing surface and optimize it for the volume mesh models. It is also typically used for remeshing surfaces that are produced by the surface wrapper model, which is the case in this study. The following options were selected for the surface remesher model: curvature, proximity, and compatibility refinement, retain geometric features, create aligned meshes, minimum face quality of 0.1, and enable automatic surface repair.

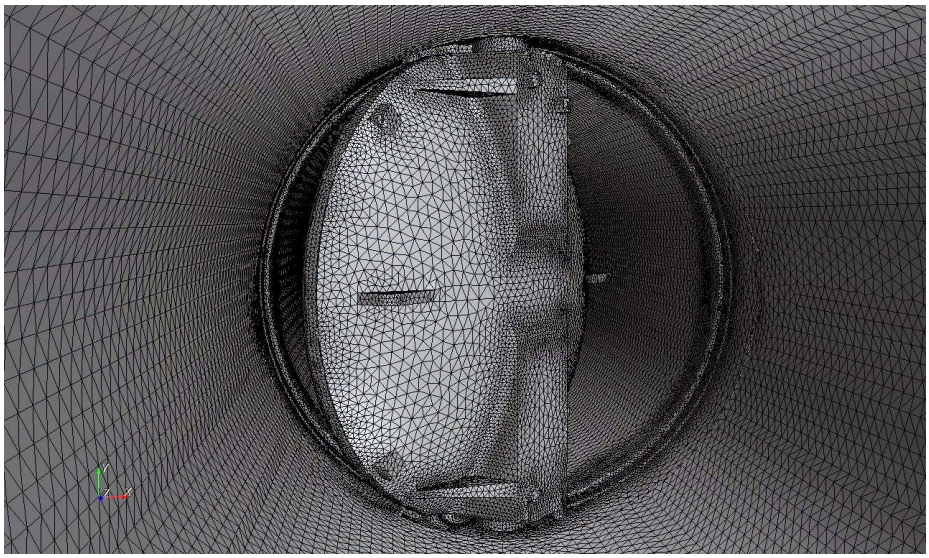

Fig. 4.6: Surface mesh inside of the butterfly valve with no contact prevention enabled for the surface wrapper.

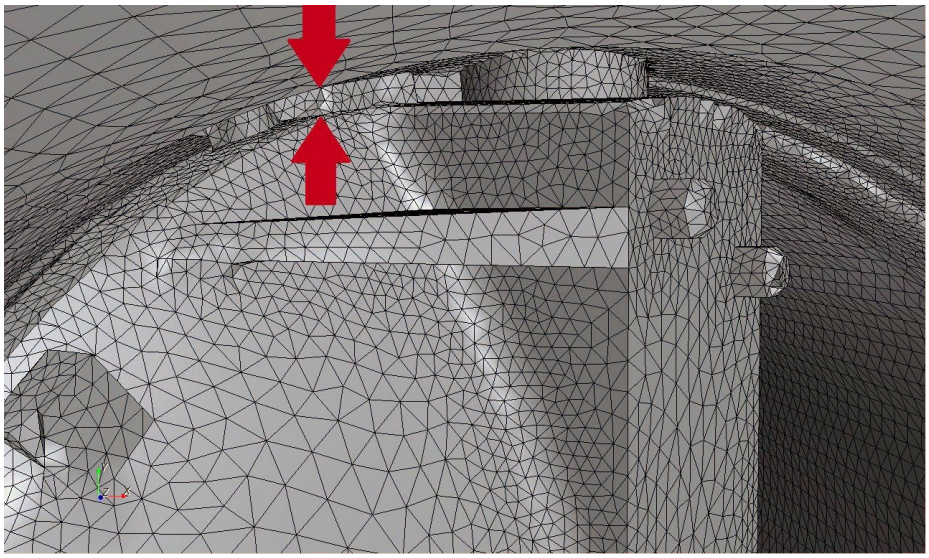

Fig. 4.7: Close-up view of the unintended surface mesh intersection between the butterfly valve wall and the disk.

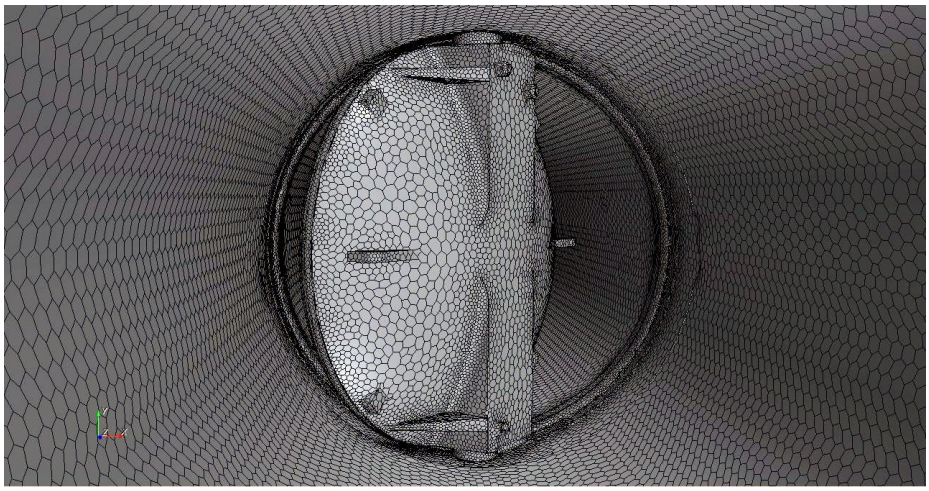

Fig. 4.8: Surface mesh inside of the butterfly valve with contact prevention properly applied with the surface wrapper.

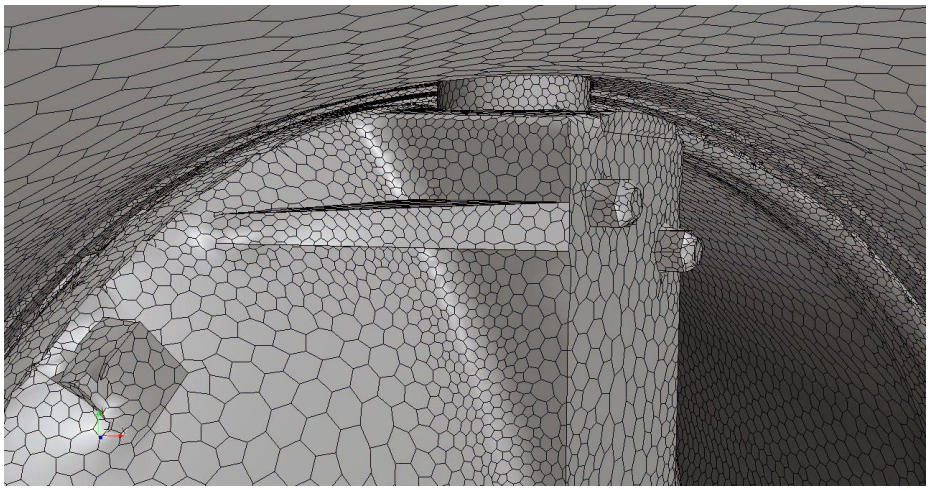

Fig. 4.9: Close-up view of a correct application of the surface mesh between the butterfly valve wall and the disk.

Table 4.1: Reference values for butterfly valve CFD simulations.

Reference Value	Dimension/Value
Base Size	50 mm
Automatic Surface Repair Minimum Proximity	0.06
Automatic Surface Repair Minimum Quality	0.05
CAD Projection	Enabled
Number of Prism Layers	8
Prism Layer Stretching	1.2
Prism Layer Thickness	35.0mm
Enable Curvature deviation distance	Disabled
Basic Curvature	120 points/circle
Surface Growth Rate	1.25
Surface Proximity # of points in gap	2.0
Surface Proximity Search Floor	0.0m
Surface Relative Minimum Size	25%
Surface Relative Target Size	100%
Tet/Poly Density	1.0
Tet/Poly Growth Factor	1.0
Tet/Poly Volume Blending Factor	1.0
Wrapper Feature Angle	30.0 deg.
Wrapper Scale Factor	100%

4.3.6 Reference Values

Once the meshing models have been selected with their given parameters and options, reference values based off those models need to be set. Reference values apply to all meshing parameters on a global level and can be set to apply to all boundaries and surfaces in a region continuum. Custom values can also be selected for each boundary inside the continuum. Furthermore, most reference values can be set as absolute quantities or as a percentage relative to the base size. The meshing reference values were set as seen in Table 4.1.

It should also be noted that the base size reference value was the same for all results presented in Chapter 6, and were only modified to investigate grid refinement at two coarser levels each carried out for the 10, 50, and 90 degree open cases which will be later discussed. Once all the options and parameters were set for the core mesh, local refinement using volumetric controls was carried out.

4.4 Localized Refinement

In CFD simulations, it is common to enable localized refinement in areas that are of most interest, and/or require greater detail in order to appropriately resolve existent behavior. In STAR-CCM+, volumetric controls (VC) can be enabled to allow the user to make predefined volumes from generic and custom geometries to refine the mesh as desired within those volumes. Custom parameters were enabled inside each VC for the following: custom base size relative to the reference base size value in Table 4.1, number of prism layers, prism layer stretching, and prism layer absolute thickness. Three different VCs were enabled and labeled as: coarse, fine, and disc, as seen in Figs. 4.10 and 4.11. The mesh accordingly becomes more refined as the butterfly valve is approached from either side of the general domain into the VC regions until reaching its finest VC closest to the disc. This will ensure that computational burdens are not excessive due to refining unnecessary parts of the whole mesh, and that meshing resources are placed in the area of interest and likely instability. Table 4.2 shows the custom values used for each VC. Regions not within a VC maintain the same parameters and options as found in Table 4.1.

The coarse volumetric control extends 1.75 m in both directions away from the butterfly valve as a large cylinder that encompasses the flow domain within its length. The fine volumetric control extends 0.85 m in both directions away from the butterfly valve as a large cylinder that encompasses the flow domain within its length. The disc control volume is modeled as a thick disk that encompasses the dynamic disc components of the butterfly valve. This disc volumetric control has a radius of 0.75 m with a total thickness of 0.5 m centered along the butterfly valve shaft and perpendicular to the axis of flow. While the coarse and fine volumetric controls remain stationary, the disc volumetric control has the same alignment as the valve degree opening. Sizes of the volumetric controls in Figs. 4.10 and 4.11 have been embellished to distinguish the overlap between each volumetric control. After meshing, the difference between the volumetric control regions is easily identified, due to the progression of refinement of the mesh as the butterfly valve is approached as seen in Figs. 4.12 and 4.13.

Table 4.2: Custom values for volumetric controls.

Volumetric Control	Relative Base Size (%)	Number of Prism Layers	Prism Layer Stretching	Prism Layer Absolute Thickness (mm)
Coarse	80	8	1.2	30
Fine	50	4	1.2	25
Disk	35	3	1.2	10

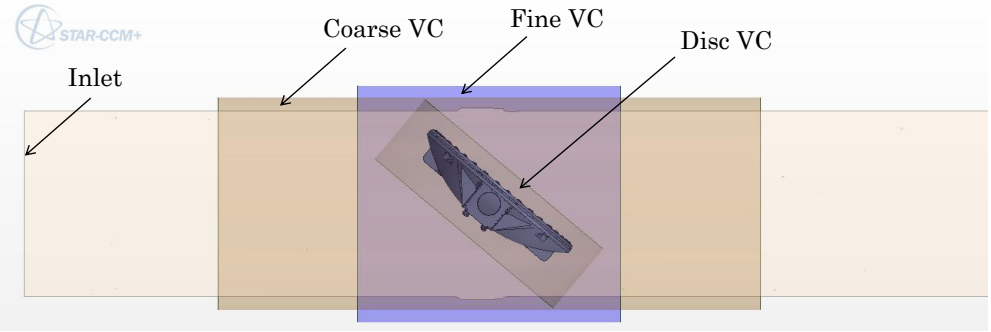

Fig. 4.10: Top view of the three volumetric controls for a 50 degree open valve.

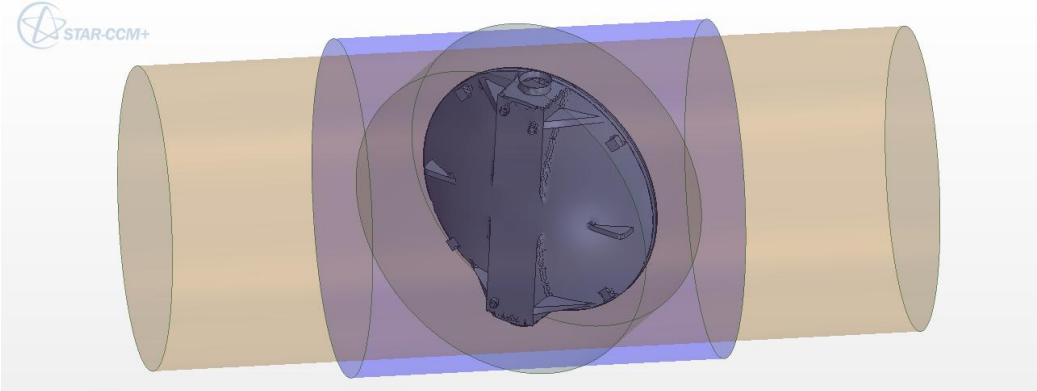

Fig. 4.11: Isotropic view of the three volumetric controls for a 50 degree open valve.

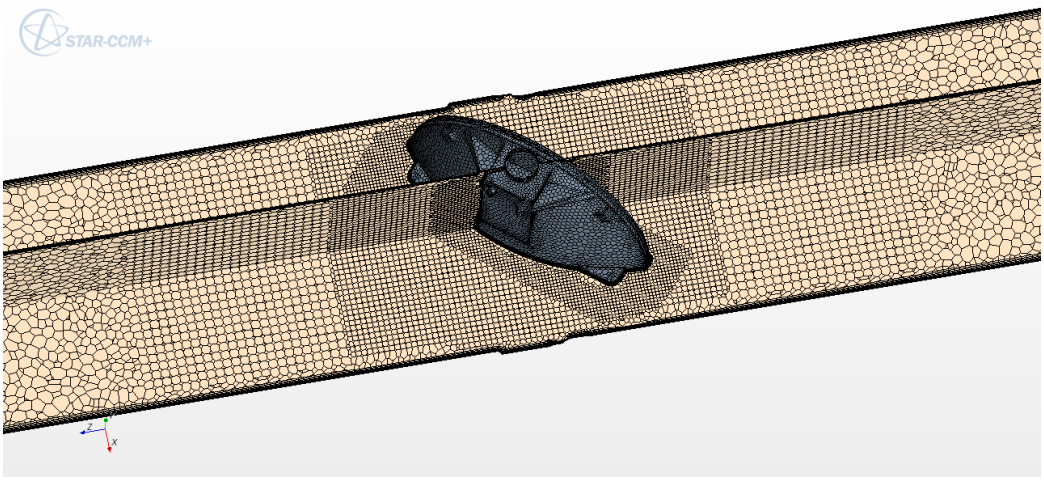

Fig. 4.12: Isotropic view of two cross-sections of a volumetric mesh with three volumetric controls for a 50 degree open valve.

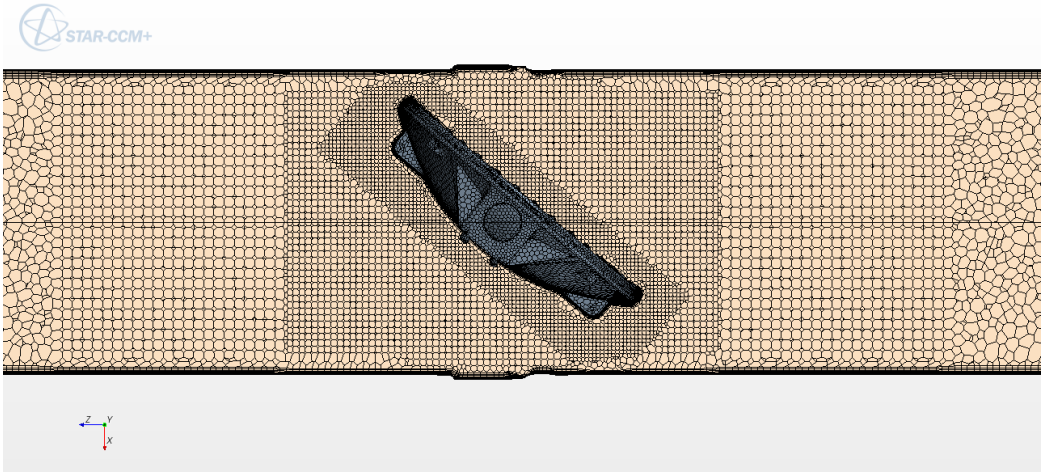

Fig. 4.13: Top view of a cross-section of a volumetric mesh with three volumetric controls for a 50 degree open valve.

4.5 Grid Refinement

A vital part of using numerical methods such as CFD, is estimating the contribution of discretization errors. In order to investigate this, it is necessary to carry out grid refinement and/or coarsening of the discretized domain one is trying to solve in order to see the behavior of the solution as more or less resolution is provided by the corresponding mesh. For this study, three different disk angle opening cases were coarsened to estimate the discretization error. The three different disk angle openings investigated were the following: 10, 50, and 90 degrees open.

The recommended method for discretization error estimation is the GCI method [25], which is based on the Richardson extrapolation (RE) method. The GCI method will be outlined here, with the results presented in Chapter 6.

The first step of the GCI method involves defining a representative cell size, h, which for three-dimensional calculations is given as

$$h = \left[\frac{1}{N}\sum_{i=1}^{N}(\Delta V_i)\right]^{1/3}, \tag{4.1}$$

where ΔV_i is the volume of the i^{th} cell, and N is the total number of cells used for the computations. The second step requires three different sets of grids and run simulations to determine the values of key variables, ϕ, important to the objective of the simulation study. For this study, the key variables are the butterfly valve performance factors. The grid representative cell sizes for the three different meshes used are h_1, h_2, h_3, where h_1 represents the finest mesh and h_3 represents the coarsest mesh, such that $h_1 < h_2 < h_3$. For the third step we define mesh refinement ratios, r, such that $r_{21} = h_2/h_1$, and $r_{32} = h_3/h_2$, in order to calculate the apparent order, p, of the method using the following expressions

$$p = \frac{1}{ln(r_{21})}\left|ln\left|\frac{\epsilon_{32}}{\epsilon_{21}}\right| + q(p)\right|, \tag{4.2}$$

$$q(p) = ln\left(\frac{r_{21}^2 - s}{r_{32}^2 - s}\right), \tag{4.3}$$

$$s = 1 * sign\left(\frac{\epsilon_{32}}{\epsilon_{21}}\right), \tag{4.4}$$

where $\epsilon_{32} = \phi_3 - \phi_2$, $\epsilon_{21} = \phi_2 - \phi_1$, with ϕ_k denoting the solution on the k^{th} grid. If $\epsilon_{32}/\epsilon_{21} < 0$, oscillatory convergence is indicative, and the percent occurrence of oscillatory convergence should be reported. Agreement of the observed apparent order with the formal order of the scheme used can be taken as a good indication of the grids being in the asymptotic range, while the converse should not necessarily be taken as a sign of unsatisfactory calculations [25]. Additionally, if ϵ_{32} or ϵ_{21} is really close to zero, the above procedure will not work. This might be an indication of oscillatory convergence or, in rare situations, it may indicate that the "exact" solution has been attained. Step four involves calculating the extrapolated value from

$$\phi_{ext}^{21} = \frac{(r_{21}^p \phi_1 - \phi_2)}{r_{21}^p - 1}), \tag{4.5}$$

and similarly for ϕ_{ext}^{32}. For step five, the following error estimates are calculated and reported along with the apparent order:

$$e_a^{21} = \left|\frac{\phi_1 - \phi_2}{\phi_1}\right|, \tag{4.6}$$

$$e_{ext}^{21} = \left|\frac{\phi_{ext}^{21} - \phi_1}{\phi_{ext}^{21}}\right|, \tag{4.7}$$

$$GCI_{fine}^{21} = \frac{1.25 e_a^{21}}{r_{21}^p - 1}, \tag{4.8}$$

termed the approximate relative error, extrapolated relative error, and the fine-grid convergence index, respectively.

When computed profiles of the key variables are presented, it is recommended that numerical uncertainty be indicated by error bars on the profile, analogous to experimental uncertainty. This is done by using the GCI index of Eqn. 4.8 in conjunction of an average value of $p = p_{avg}$ as a measure of the global accuracy, which is plotted in the form of error bars for the simulated results. These results will be presented in Chapter 6. However, it should be noted that the error bars in the results are of such small magnitude that they are rarely identifiable in the plots in Chapter 6.

Chapter 5

Physics

5.1 Physical Models and Options

Once the meshing continuum was completely setup, a physics continuum was added to the simulation in order to define the physical models that will govern the fluid flow in the prescribed domain. The main physical models chosen include the following: gradients, implicit unsteady, k-ϵ turbulence, realizable k-ϵ two-layer, Reynolds-averaged Navier-Stokes, segregated flow, three dimensional, turbulent, two-layer all y+ wall treatment. An explanation of each meshing model as well as selected parameters and options for this study are described in subsequent paragraphs. Further explanations can be found in Appendix D and also the STAR-CCM+ user's manual [24].

5.1.1 Three Dimensional

This spatial model provides a method for computing and accessing mesh metrics such as the cell volume and centroid for each discrete cell in three dimensions.

5.1.2 Gradients

Gradients are used in several places within the transport equation solution methodology including: reconstructing field values at the cell faces, secondary gradients for diffusion terms, pressure gradients for pressure-velocity coupling in the segregated flow model, and strain-rate and rotation-rate calculations for turbulence models.The default options and parameters chosen include: verbose disabled, Hybrid Gauss-LSQ gradient method, Venkatakrishnan limiter method, least-squares quality criterion enabled, flat cells curvature criterion enabled, cell skewness criterion enabled, chevron-cell criterion enabled, least-squares tensor

minimum eigenvalues ratio set to 0.1, normalized flat cells curvature factor set to 1.0, maximum safe skewness angle set to 75 degrees, and the minimum unsafe skewness angle set to 88 degrees.

5.1.3 Implicit Unsteady

This time model provides a basis for which temporal discretization occurs and is only available for use with the segregated flow models. It also controls the time-step size and update of the simulation at each physical time step. One of the main objectives of the simulations in this study is to know the butterfly valve performance factors under steady inlet and outlet conditions in the flow. In order to achieve this, one can select time models such as steady and iterate until convergence. Another option is to select the explicit unsteady or implicit unsteady time models and step through time until the flow solution becomes unchanging.

The steady model will remove any time varying values from the governing CFD equations and attempt to converge on a steady-state solution, which can be difficult due to the various complexities of any given flow domain. The explicit and implicit unsteady models march through the simulations in discrete physical time steps, with the implicit method offering more enhanced stability in exchange for a longer computational time. Because of instabilities in the simulations of this study, the steady and explicit unsteady models struggled to converge and produce good results. Consequently, the implicit unsteady time model was chosen, with a 1^{st} order temporal discretization and time step size of 0.05 seconds for most simulations.

5.1.4 Liquid

This model simulates a single-component liquid material inside the fluid continuum. The liquid chosen for the simulations was water, with the following material properties: density of 1000.7 kg/m^3 and a dynamic viscosity of 0.001348 Pa-s.

5.1.5 Constant Density

Choosing the constant density model allows the liquid model to be treated as an incompressible fluid.

5.1.6 Segregated Flow

The segregated flow model solves the flow equations (one for each component of velocity, two for the turbulence equations, and one for pressure) in a segregated, or uncoupled, manner. The linkage between the momentum and continuity equations is achieved with a predictor-corrector approach. The following options and parameters chosen were: 2^{nd} order for the convection scheme, minimum absolute pressure of 1000 Pa, flow boundary diffusion enabled, secondary gradients enabled, and delta-V dissipation disabled.

5.1.7 Turbulent

This viscous regime allows for the modeling of turbulence, which is characterized by irregular, random, and unstable flow. Once selected, a selection of possible turbulent models is made available to the user.

5.1.8 k-ϵ Turbulence

Selecting the turbulence modeling option automatically invokes the Reynolds-Averaged Navier-Stokes (RANS) model to solve for Reynolds-Averaged Turbulence.

5.1.9 Realizable k-ϵ Two-Layer

The realizable two-layer k-ϵ model combines the realizable k-ϵ model with the two-layer approach. The coefficients in the models are identical, but the model gains the added flexibility of an all y+ wall treatment. Chosen options and parameters include: Wolfstein shear driven two-layer type, 2^{nd} order convection scheme, normal stress term disabled, two-layer ReY* set to 60, two-layer delta ReY set to 10, secondary gradients enabled, buoyancy production of dissipation set to boundary layer operation, C_μ set to 0.09, $C_{1\epsilon}$ set to 1.44,

$C_{2\epsilon}$ set to 1.9, C_t set to 1.0, σ_k set to 1.0, σ_ϵ set to 1.2, Sarkar set to 2.0, turbulent kinetic energy minimum set to 1.0E-10, and total dissipation rate minimum set to 1.0E-10.

5.1.10 Two-Layer All y+ Wall Treatment

Two-Layer All y+ wall treatment is a formulation that is identical to the All y+ wall treatment, but contains a wall boundary condition for the turbulent kinetic energy that is consistent with the two-layer formulation. The all y+ wall treatment is a hybrid treatment that attempts to emulate the high y+ wall treatment for coarse meshes and the low y+ wall treatment for fine meshes. It is also formulated with the desirable characteristic of producing reasonable answers for meshes of intermediate resolution (that is, when the wall-cell centroid falls within the buffer region of the boundary layer).

5.1.11 Reference Values

Only two reference values are required for the physics continuum: minimum allowable wall distance and reference pressure. The minimum allowable wall distance was set to 1.0E-6 m and the reference pressure was specified at a point 2D upstream from the butterfly valve, which coincides with the measurements taken in Table 2.1. Corresponding values for ΔP_θ were specified at this reference point for each simulation. The absolute pressures in the butterfly valve simulations used this as a point of reference for the entire system.

5.1.12 Initial Conditions

Prior to running the solver, initial conditions must be set across the entire flow domain. The gage pressure was set to zero, while the turbulent dissipation rate, turbulent kinetic energy, and velocity were set to the same values extracted from their corresponding periodic flow simulations previously discussed.

5.2 Criteria for Convergence

Throughout the process of running the CFD software to solve the equations governed by the physics models selected, the residuals must be monitored for satisfactory convergence.

Residuals represent the change in the solution of each equation being solved after each iteration. The following residuals were monitored by plotting after every iteration within each time step: continuity, x-momentum, y-momentum, z-momentum, turbulent kinetic energy, and turbulent dissipation rate. According to the American Society of Mechanical Engineers (ASME) [26], iterative convergence between each time step should be at least three (preferably four) orders of magnitude decrease in the normalized residuals for each equation solved. Convergence criteria for this study follows the ASME standard, combined with a "leveling out" of the residuals as seen in Fig. 5.1, giving convergence between each time step.

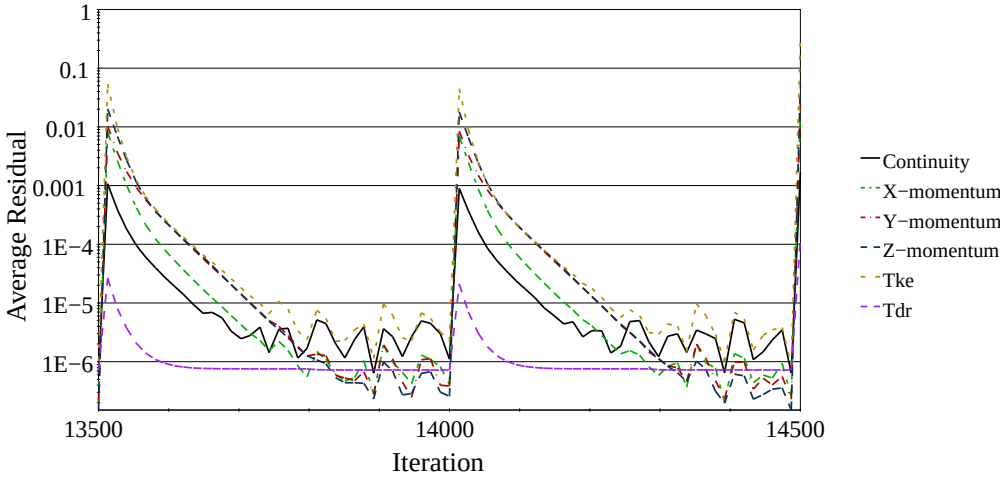

Fig. 5.1: Example of residual convergence between time steps.

The performance factors were also monitored at each time step, in order to observe when they stopped changing. The simulations typically required about 100-120 time steps on average (5-6 seconds of physical time), for the performance factors to become time-independent as seen in Fig. 5.2.

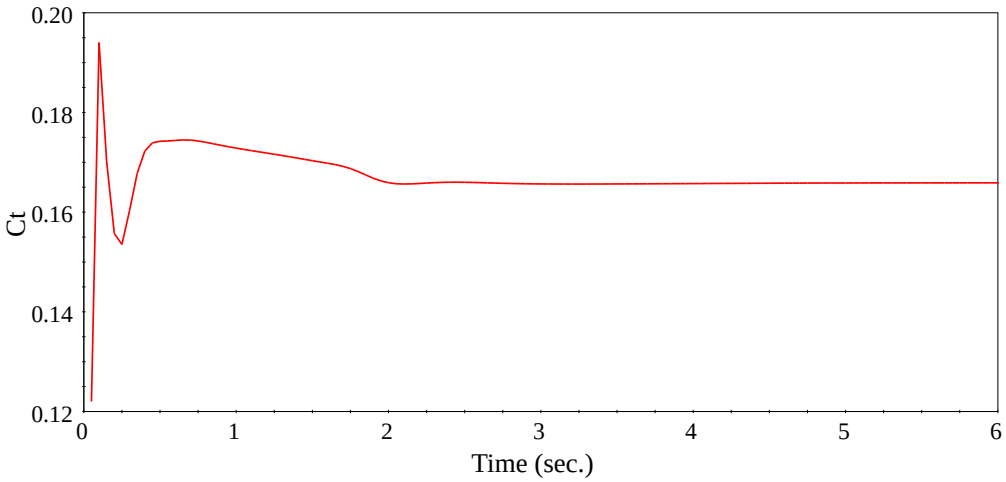

Fig. 5.2: Example of convergence for the torque coefficient, $C_{t\theta}$.

Chapter 6

Results

All of the CFD simulations discussed were carried out using the criteria previously mentioned in Chapters 4 and 5. The flow fields generated by the simulations were studied, including visualizations of flow field streamlines, velocity vectors, and pressure fields. These visualizations are shown in Figs. 6.1 - 6.29 and will be discussed accordingly. Additional figures are provided in Appendix E. The performance factors were also calculated and tabulated for comparison with the experimental results as shown in Tables 6.1 - 6.5. Additionally, Figs. 6.30 - 6.34 show plots of these results, including the relative difference of the simulation results from the experiment (E_{rel}). An outline of these results will be discussed in this chapter, followed by the results of the grid refinement study for the 10, 50, and 90 degree open cases.

6.1 Visualization of the Results

A common characteristic of the simulated flow in all of the valve degree openings is the development and eventual dissipation of a pair of swirling vortices that form after passing around the butterfly valve as seen in Fig. 6.1 and 6.2. The absolute pressure and velocity scalar bars represent the disk surface and streamlines, respectively. The top streamline view in Fig. 6.1 shows some steady streamlines along the larger opening between the valve disk and the pipe wall. Streamlines along the butterfly valve disk separate from the valve disk and cause a large amount of turbulent and swirling behavior. Henderson et al. [16] also noted this behavior and the presence of a strong pair of vortices behind butterfly valves as seen in Fig. 6.2.

Visualization of the flow field for the absolute pressure and the velocity vectors is presented along two planes intersecting the flow domain: one perpendicular to the angle

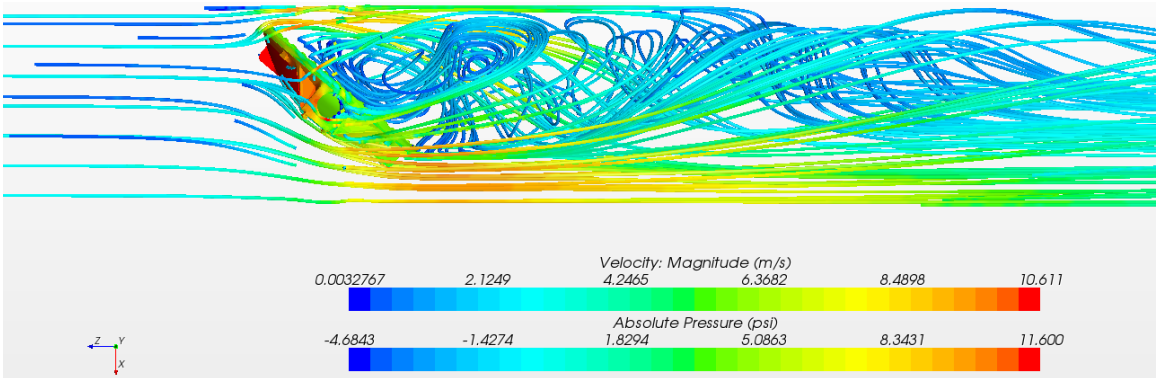

Fig. 6.1: Top streamline view of the swirling vortex flow features and the absolute pressure on the surface of a 50 degree open butterfly valve disk.

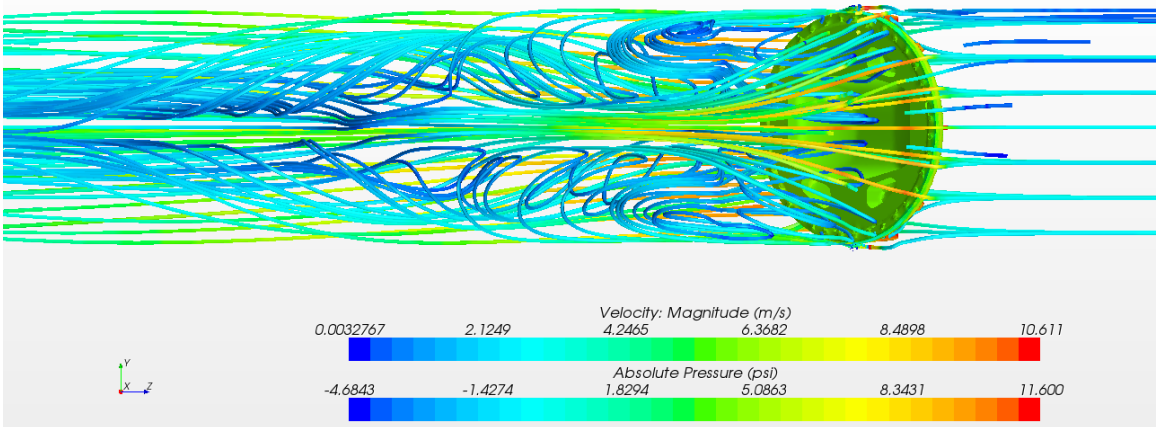

Fig. 6.2: Backside streamline view of the the swirling vortex flow features and the absolute pressure on the surface of a 50 degree open butterfly valve disk.

of rotation, and another parallel to the angle of rotation for the butterfly valve, referred henceforth as the top and side views, respectively. These visualizations can be seen in Figs. 6.3 - 6.29. Detailed views of the region surrounding the valve are also given in the mentioned figures, in order to allow greater clarity regarding the characteristics of the flow.

For the 10 degree open cases, high pressure is observed in the small gap between the valve disk and the pipe wall as shown in Fig. 6.3. A large pressure drop across the valve is also observed. The velocity vectors in Fig. 6.4 show swirling and rotational flow behind the valve disk, with large eddies present. The velocity vectors for the side view in Fig. 6.5 show a pair of eddy regions symmetrically across from one another.

For the 20 degree open case, distinct areas of high pressure are seen on the larger gap opening between the butterfly valve disk and the pipe wall as seen in Fig. 6.6. A much smaller pressure drop across the valve is present in comparison to the 10 degree case. The velocity flow field is similar to that of the 10 degree case with exception to a more concentrated eddy region directly behind the valve disk as seen in Fig. 6.7.

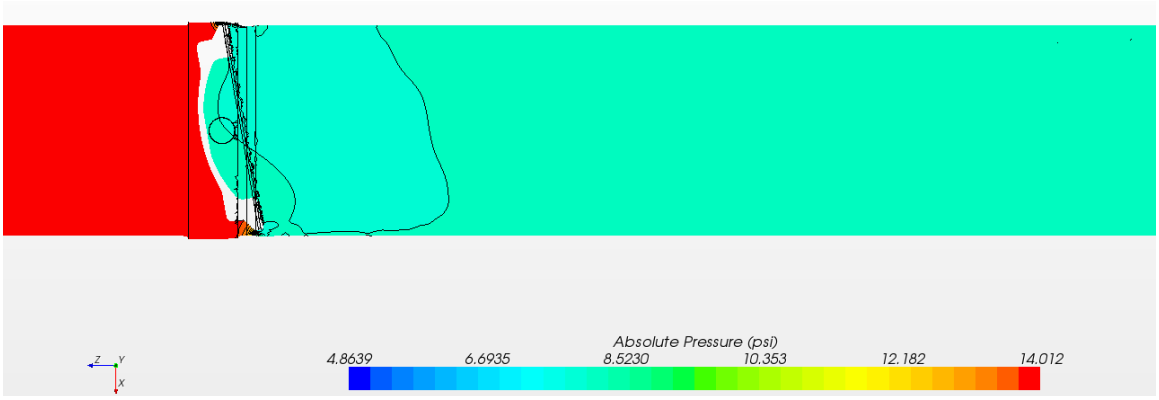

Fig. 6.3: Detailed top view of absolute pressure across the butterfly valve for the 10 degree open case.

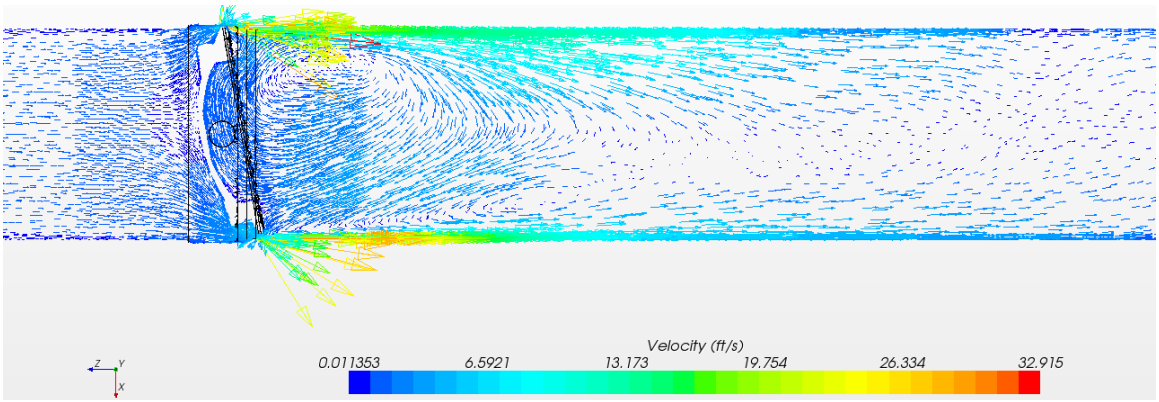

Fig. 6.4: Detailed top view of velocity vectors across the butterfly valve for the 10 degree open case.

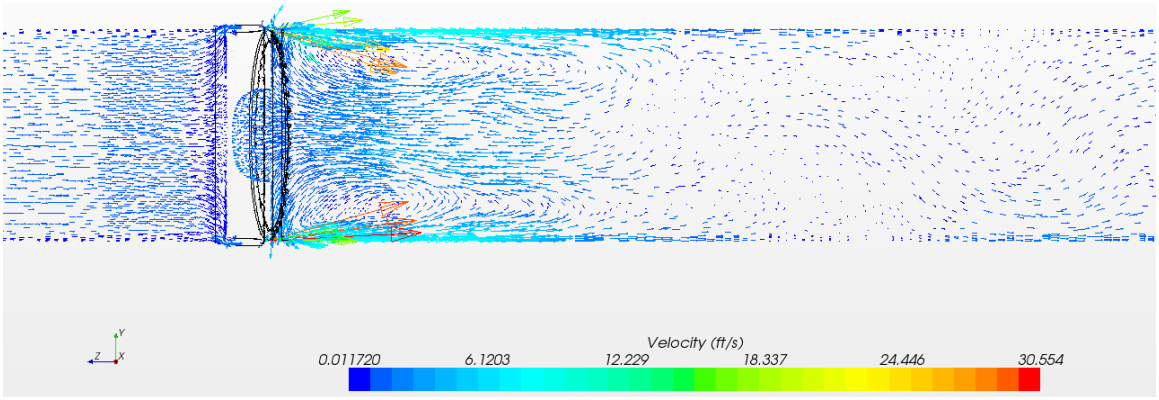

Fig. 6.5: Detailed side view of velocity vectors across the butterfly valve for the 10 degree open case.

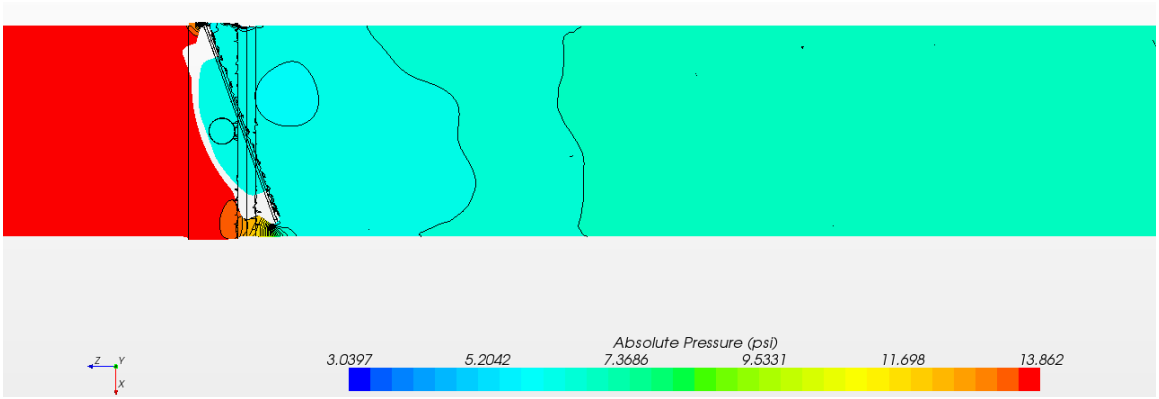

Fig. 6.6: Detailed top view of absolute pressure across the butterfly valve for the 20 degree open case.

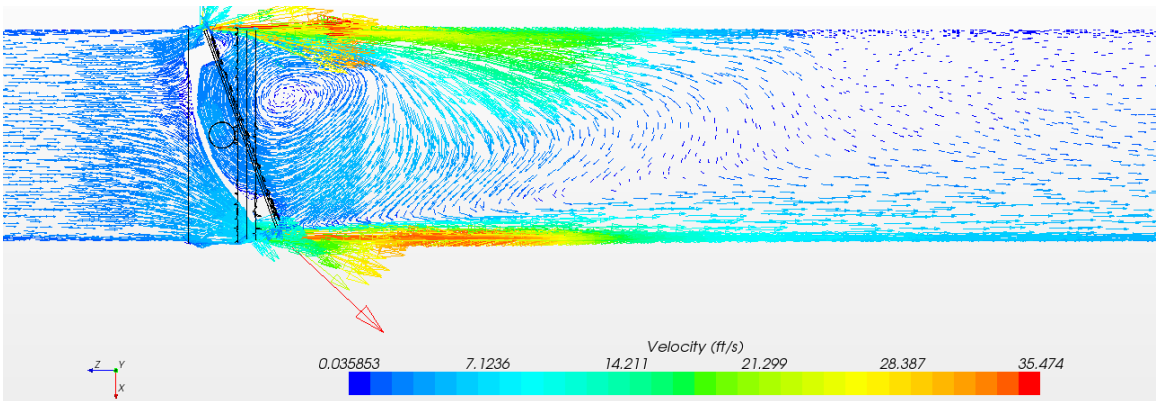

Fig. 6.7: Detailed top view of velocity vectors across the butterfly valve for the 20 degree open case.

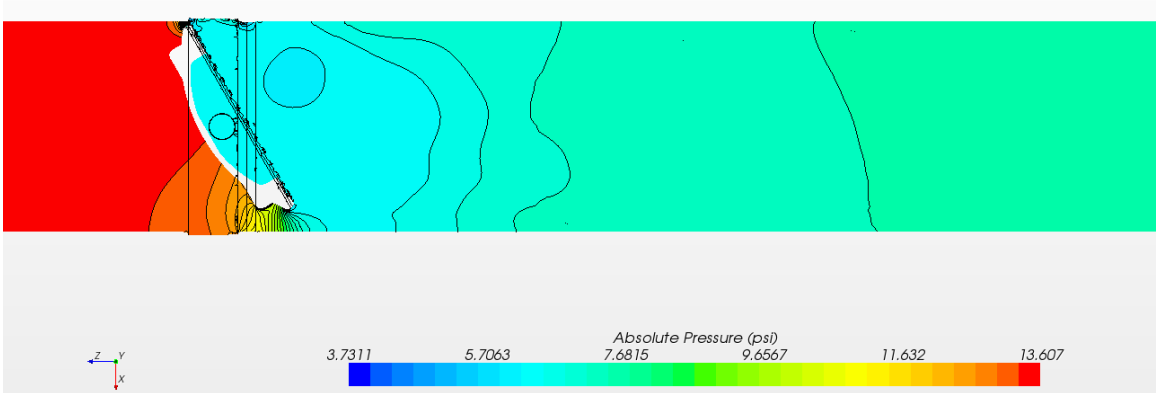

Fig. 6.8: Detailed top view of absolute pressure across the butterfly valve for the 30 degree open case.

The 30 degree open case shows a more gradual drop in pressure from the top view of Fig. 6.8 in the larger gap region between the valve disk and the pipe wall. Figure 6.9 shows more flow moving along the pipe wall after passing the butterfly valve instead of recirculating into the strong eddy region behind the butterfly valve. The eddy regions from the side view in Fig. 6.10 appear to have moved closer towards each other near the centerline of the pipe.

In the 40 degree open case, the region of highest pressure distinctly appears at the point where the upstream flow first makes contact with the valve disk's rotating edge as seen in Fig. 6.11. In the earlier cases considered, this distinction was not observed, as the main flow maintained a higher region of pressure prior to passing through the gap between the disk and pipe wall. The concentrated eddy behind the disk from the top view appears to have moved closer to the valve axis of rotation than earlier cases as seen in Fig. 6.12. The flow passing through the gap between the disk and pipe wall also seems to be less inclined to participate in the rotating flow behind the disk. From the side view in Fig. 6.13, an interesting elliptically shaped eddy recirculation region is formed approximately one diameter length downstream.

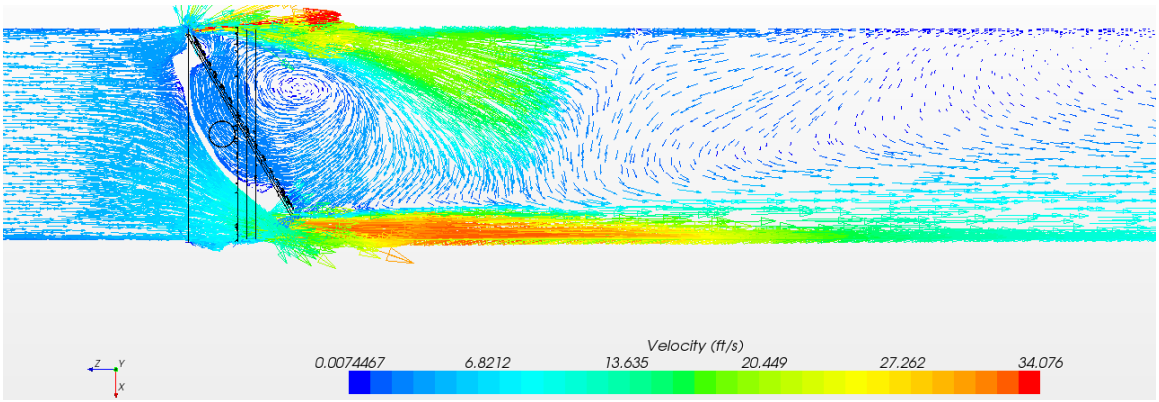

Fig. 6.9: Detailed top view of velocity vectors across the butterfly valve for the 30 degree open case.

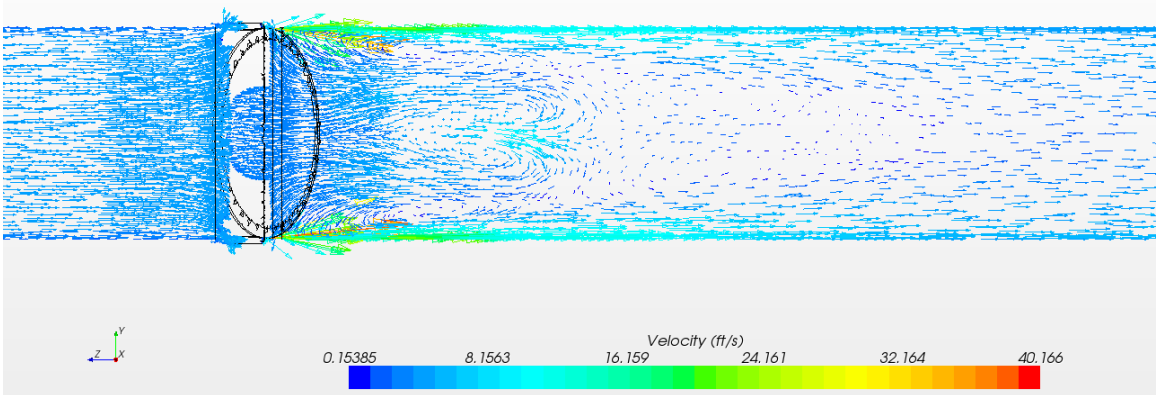

Fig. 6.10: Detailed side view of velocity vectors across the butterfly valve for the 30 degree open case.

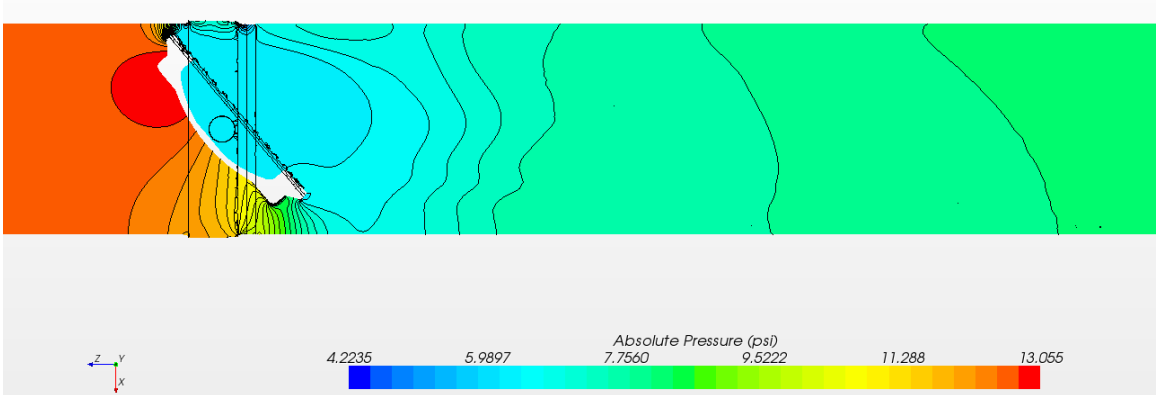

Fig. 6.11: Detailed top view of absolute pressure across the butterfly valve for the 40 degree open case.

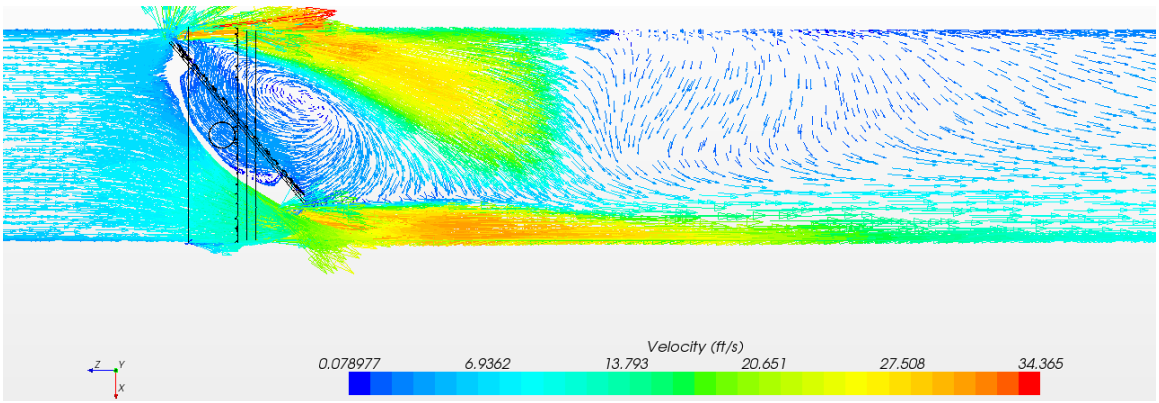

Fig. 6.12: Detailed top view of velocity vectors across the butterfly valve for the 40 degree open case.

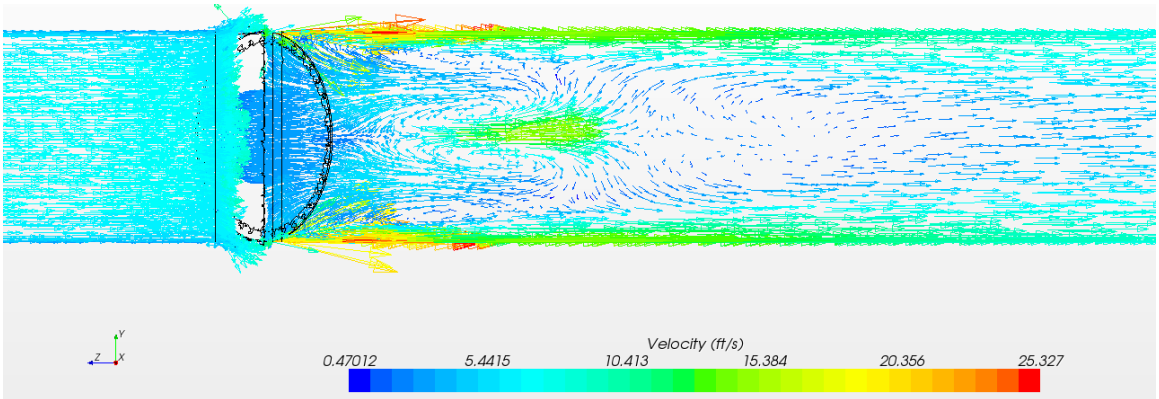

Fig. 6.13: Detailed side view of velocity vectors across the butterfly valve for the 40 degree open case.

The 50 degree open cases also exhibits the same behavior as the 40 degree case for the distinct region of high pressure at the disk's rotated edge as seen in Fig. 6.14. In Fig. 6.15, the amount of recirculation and swirling behind the valve has decreased due to a larger area available in the relatively smaller gap between the disk and the pipe wall. This ultimately allows the flow to separate less as it comes around the valve. The elliptically shaped eddy observed in the 40 degree case has increased in magnitude of velocity as observed in Fig. 6.16.

For the 60 degree open case, the high pressure region at the rotated edge of the disk becomes less distinct. Figure 6.17 shows a more gradual pressure drop as the flow moves past the valve disk. Figure 6.18 shows the circulation region behind the valve moving even closer to the cavity portion of the disk since more flow is able to stay attached longer down the disk edge. While this occurs, the side view in Fig. 6.19 shows an even more increased amount of circulating flow in the eddy region previously described.

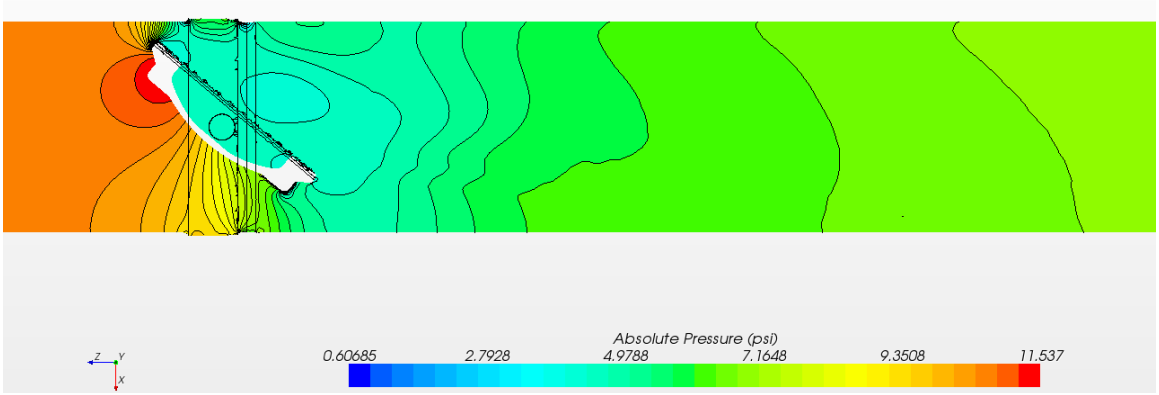

Fig. 6.14: Detailed top view of absolute pressure across the butterfly valve for the 50 degree open case.

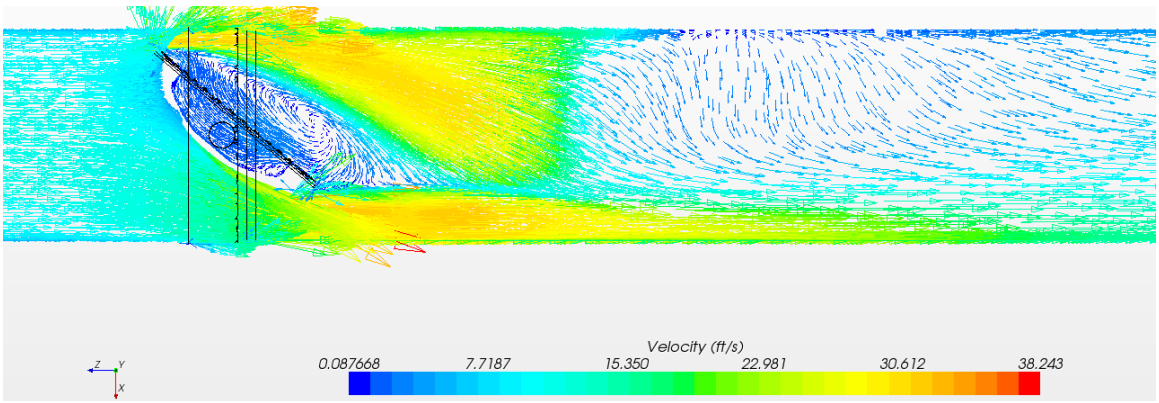

Fig. 6.15: Detailed top view of velocity vectors across the butterfly valve for the 50 degree open case.

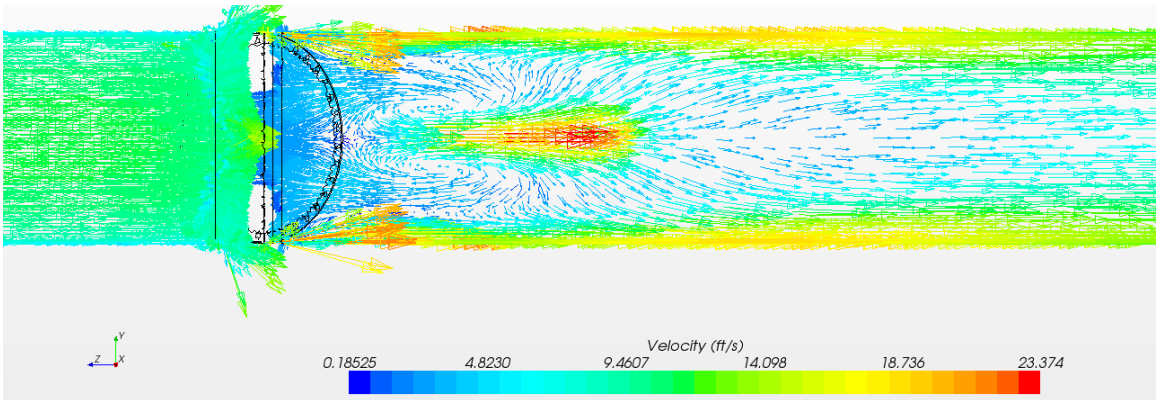

Fig. 6.16: Detailed side view of velocity vectors across the butterfly valve for the 50 degree open case.

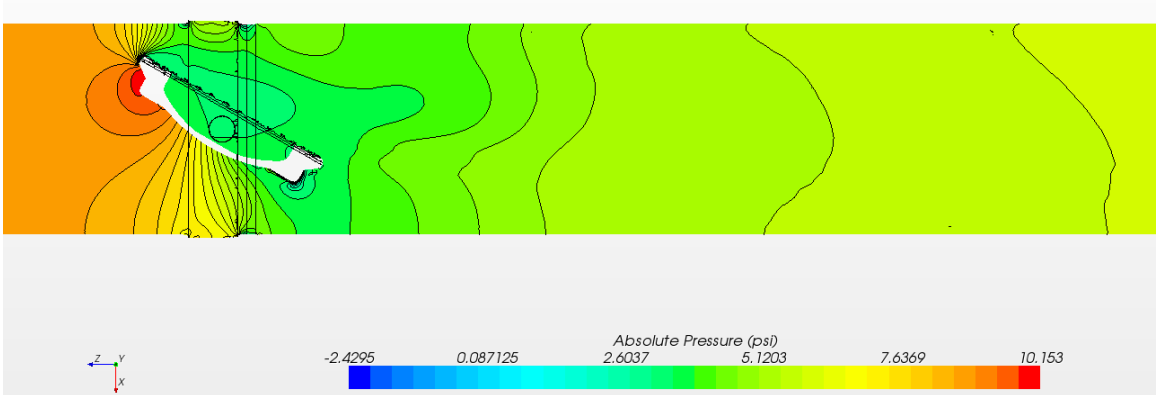

Fig. 6.17: Detailed top view of absolute pressure across the butterfly valve for the 60 degree open case.

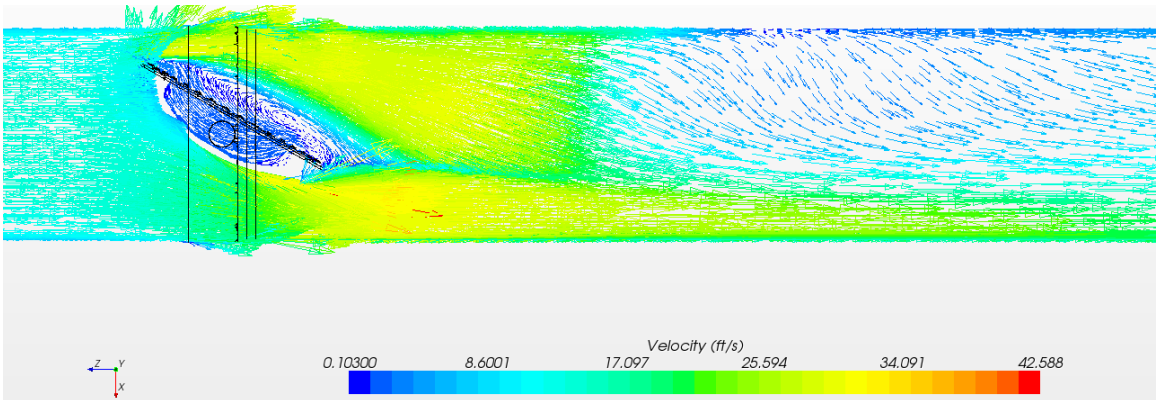

Fig. 6.18: Detailed top view of velocity vectors across the butterfly valve for the 60 degree open case.

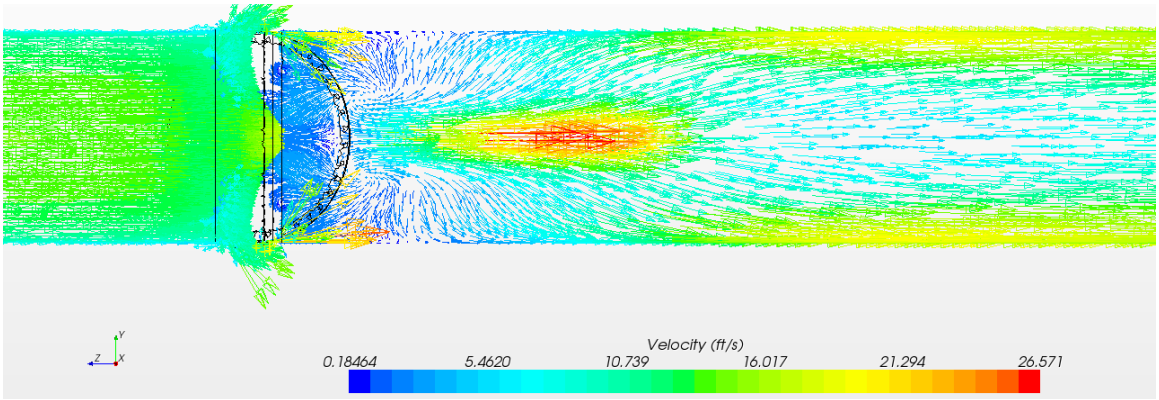

Fig. 6.19: Detailed side view of velocity vectors across the butterfly valve for the 60 degree open case.

The 70 degree open case, shows a similar pattern in the decrease of the high pressure region at the rotated edge of the disc in Fig. 6.20. The side view in Fig. 6.21, shows high regions of pressure in the pockets on the convex side of the butterfly valve disk as the flow becomes more perpendicular to the valve opening angle. The recirculation from the top view in Fig. 6.22 has become practically contained inside the concave side and feature of the butterfly valve disk. In Fig. 6.23, highly concentrated velocity vectors can be seen approximately one diameter downstream from the valve with less recirculation present.

The 80 degree open case shows agreement with the pattern seen in the top view of the 70 degree open case. For the side view, the regions of high pressure are present in the first set of pockets on the convex side of the butterfly valve disk as seen in Fig. 6.24. Two recirculating areas opposite from one another in Fig. 6.25 appear to have formed near the pipe walls and disk, downstream from the valve. These eddy regions appear to dissipate quickly downstream due to the highly dominant flow in the direction downstream from the valve.

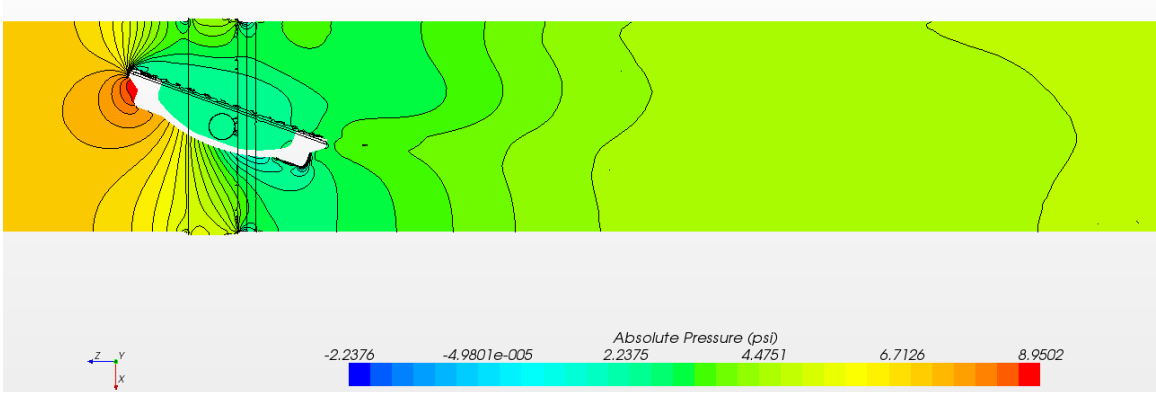

Fig. 6.20: Detailed top view of absolute pressure across the butterfly valve for the 70 degree open case.

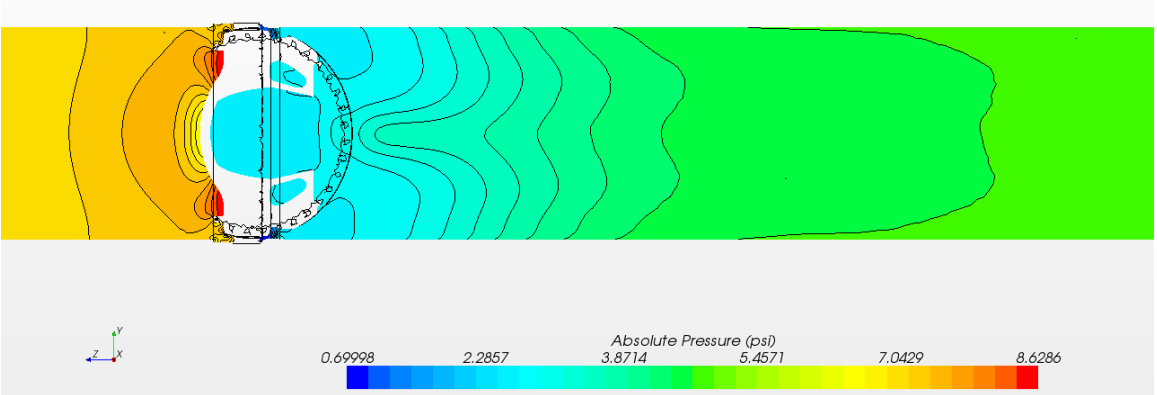

Fig. 6.21: Detailed side view of absolute pressure across the butterfly valve for the 70 degree open case.

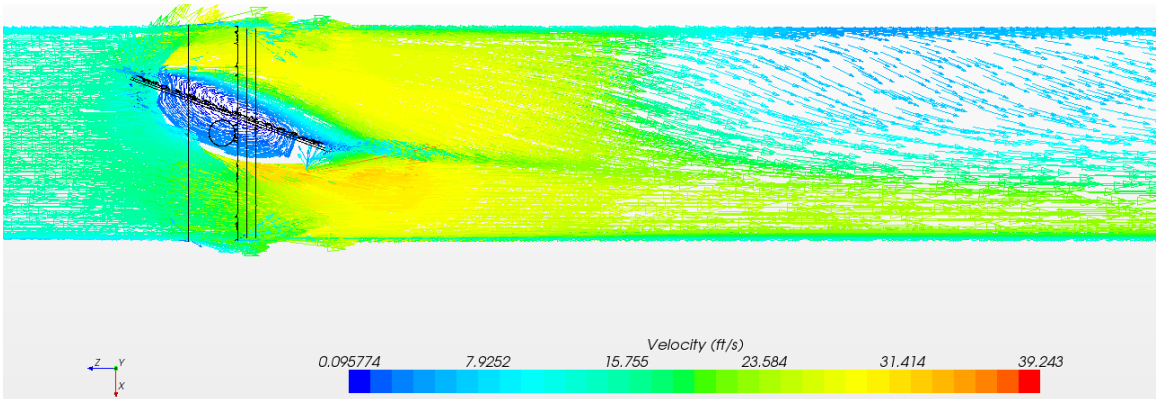

Fig. 6.22: Detailed top view of velocity vectors across the butterfly valve for the 70 degree open case.

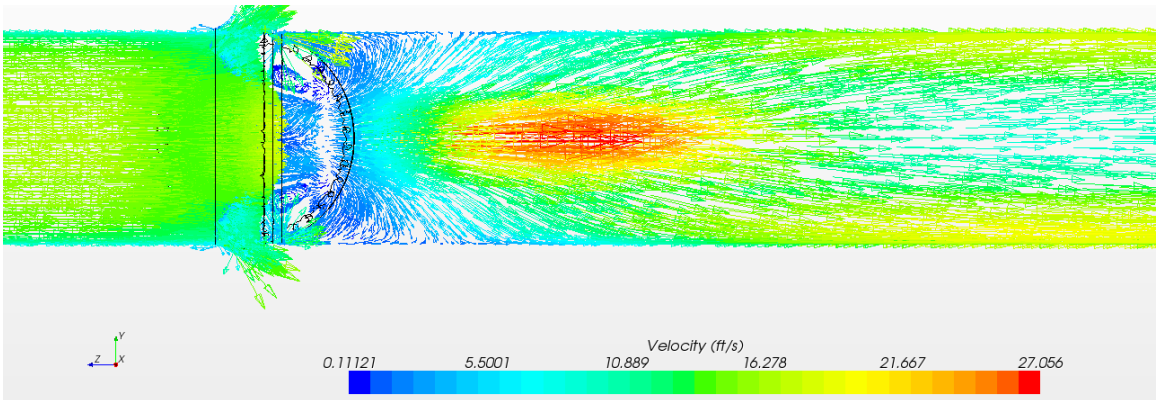

Fig. 6.23: Detailed side view of velocity vectors across the butterfly valve for the 70 degree open case.

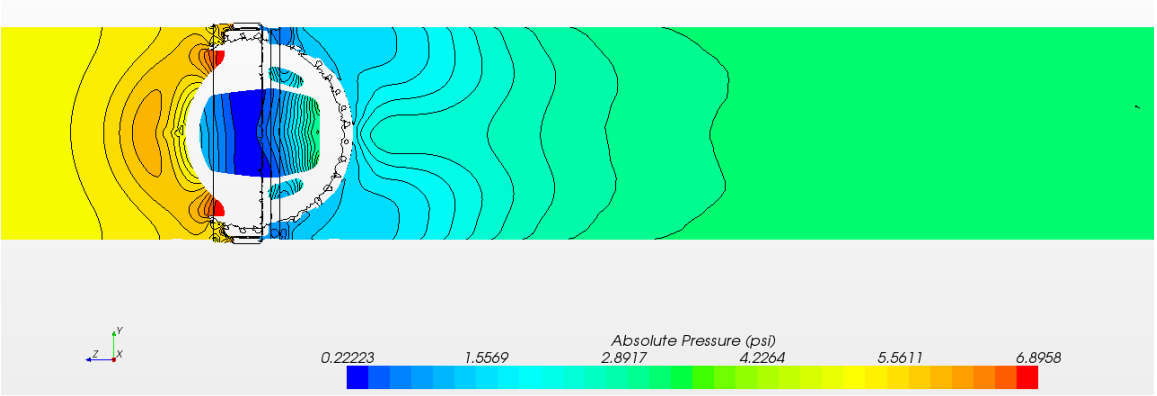

Fig. 6.24: Detailed side view of absolute pressure across the butterfly valve for the 80 degree open case.

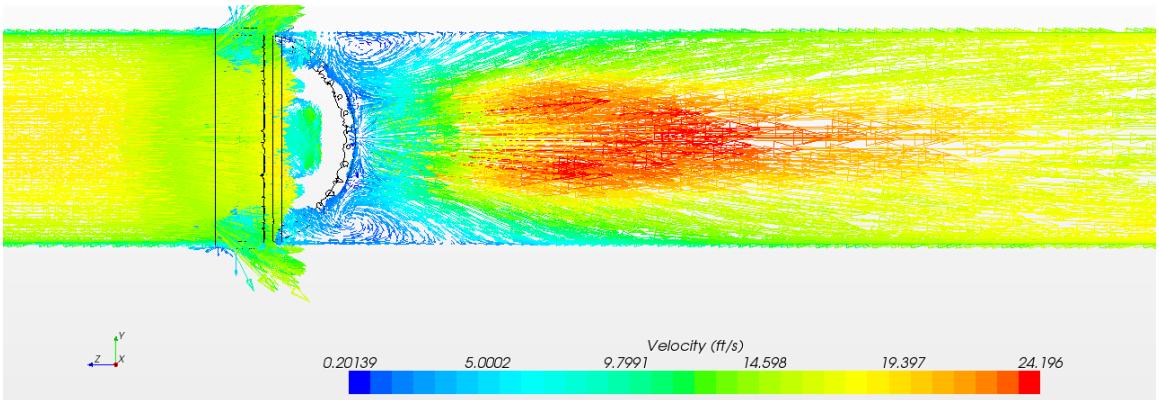

Fig. 6.25: Detailed side view of velocity vectors across the butterfly valve for the 80 degree open case.

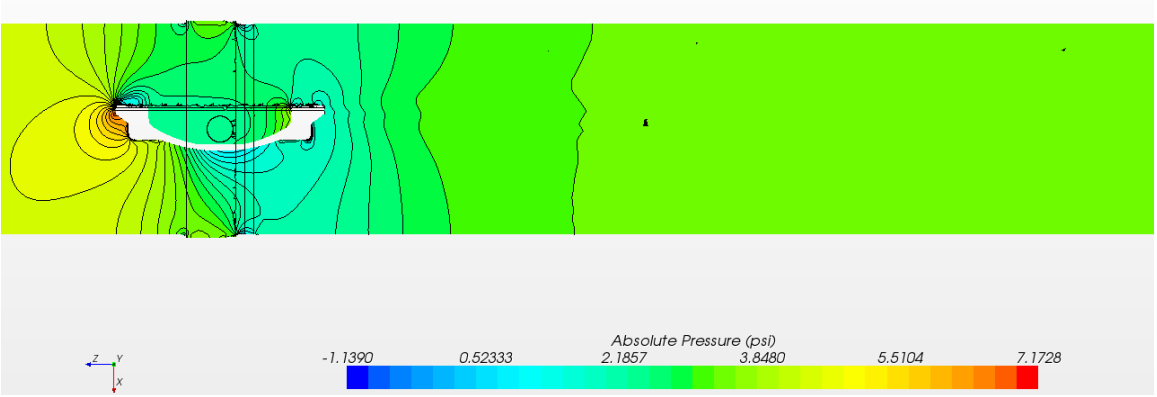

Fig. 6.26: Detailed top view of absolute pressure across the butterfly valve for the 90 degree open case.

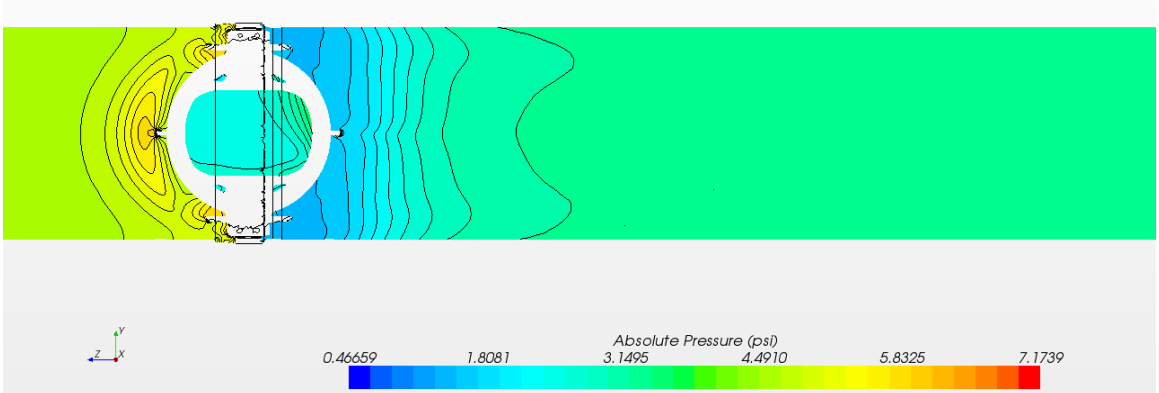

Fig. 6.27: Detailed side view of absolute pressure across the butterfly valve for the 90 degree open case.

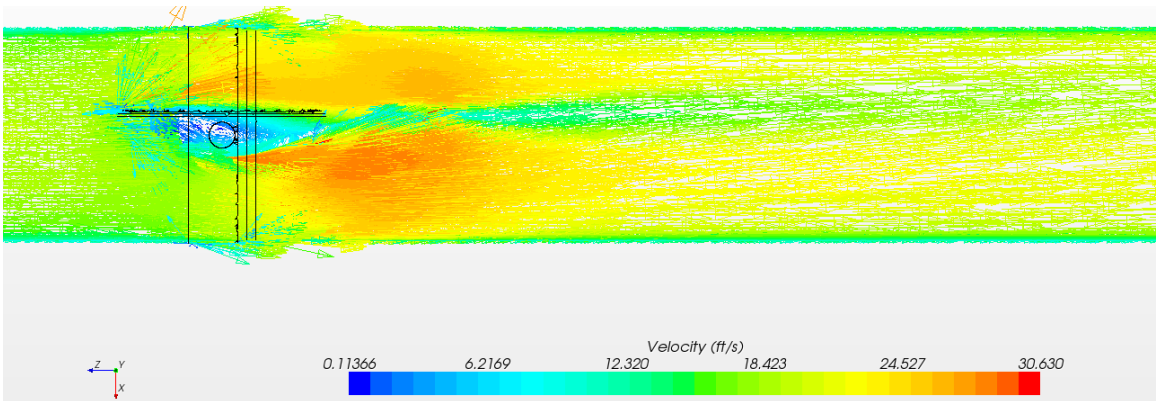

Fig. 6.28: Detailed top view of velocity vectors across the butterfly valve for the 90 degree open case.

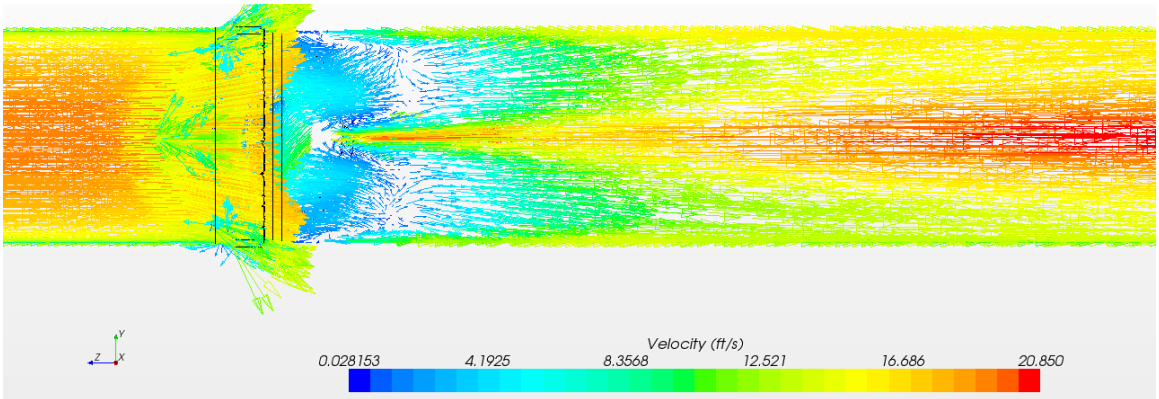

Fig. 6.29: Detailed side view of velocity vectors across the butterfly valve for the 90 degree open case.

In the 90 degree open case, the pressure gradients are quite gradual with a small amount of pressure distinctness at the leading edge of the disk in Fig. 6.26. The high pressure values in the pockets, appear to have lessened in the side of view of Fig. 6.27. Figure 6.28 shows a largely unobstructed flow and small amounts swirling due to the high opening valve angle in the flow. Like the 80 degree case, effects from the eddy regions in Fig. 6.29, appear to dissipate quickly downstream as the flow is dominated by a high velocity flow.

6.2 Comparison of Results

The pressure drop, ΔP_θ, as seen in Fig. 6.30 and Table 6.1, shows a general agreement in the pattern of the results, with exception of when θ=10 and 20 degrees. The relative difference from the experiment is least when θ = 30-50 degrees, giving values of $E_{ref} \approx \pm 5\%$. However, the pressure drop over other valve angles was not predicted well by the CFD simulations. The worst case for E_{ref} was found when θ= 10 degrees, giving a value of $E_{ref} \approx 43\%$.

The hydrodynamic torque, $T_{d\theta}$, as seen in Fig. 6.31 and Table 6.2, has an overall agreement in the pattern of the results for all valve angle openings observed, with the simulation results slightly higher than the experimental results as θ increases. Good results

in the range of $E_{ref} \approx \pm 15\%$ were found when θ = 20-80 degrees. Excellent results in the range of $E_{ref} \approx \pm 10\%$ were found when θ = 30-70 degrees. The best agreement occurred when θ=40 degrees, giving $E_{ref} \approx 5\%$. The worst cases, were observed when θ=10 and 90 degrees, giving relative difference values higher than $E_{ref} = \pm 30\%$.

The flow coefficient, $C_{v\theta}$, as seen in Fig. 6.32 and Table 6.3, demonstrates an overall agreement in the pattern of the results for all valve angle openings, with the simulation results slightly more biased higher than the experimental results as θ increases. Excellent results in the range of $E_{ref} \approx \pm 10\%$ were found when θ = 20-90 degrees. The best results were found when θ=40 and 50 degrees, giving values of $E_{ref} \approx \pm 1\%$. Overall, the CFD simulations were able to reasonably predict the experimental values except for the θ=10 degree case. The 10 degree case shows $E_{ref} \approx 33\%$.

The loss coefficient, K_θ, as seen in Fig. 6.33 and Table 6.4, shows an overall agreement in the pattern of the results for all valve angle openings. Excellent results in the range of $E_{ref} \approx \pm 5\%$ were found when θ=30-50 degrees. The closest agreement occurs when θ=40 and 50 degrees, which gives $E_{ref} < 2\%$. The rest of the cases gave results above $E_{ref} = \pm 15\%$ with the worst two case occurring when θ=10 and 90 degrees. The relative differences for these two cases were respectively, $E_{ref} \approx$ -44% and 25%. The CFD simulations struggled to adequately predict the loss coefficient overall within a range of $\pm 15\%$.

The torque coefficient, $C_{t\theta}$, as seen in Fig. 6.34 and Table 6.5, exhibits the same agreement in pattern of the results as the rest of the performance factors. The CFD simulations were able to predict the torque coefficient for all valve degree openings within $E_{ref} \approx \pm 14\%$. Excellent results within $E_{ref} \approx \pm 5\%$ can be found for when θ=10-50, and 90 degrees. Best results were found when θ=50 degrees which gives $E_{ref} < 1\%$. The worst case was seen for when θ=60 degrees, which gives $E_{ref} \approx -14\%$.

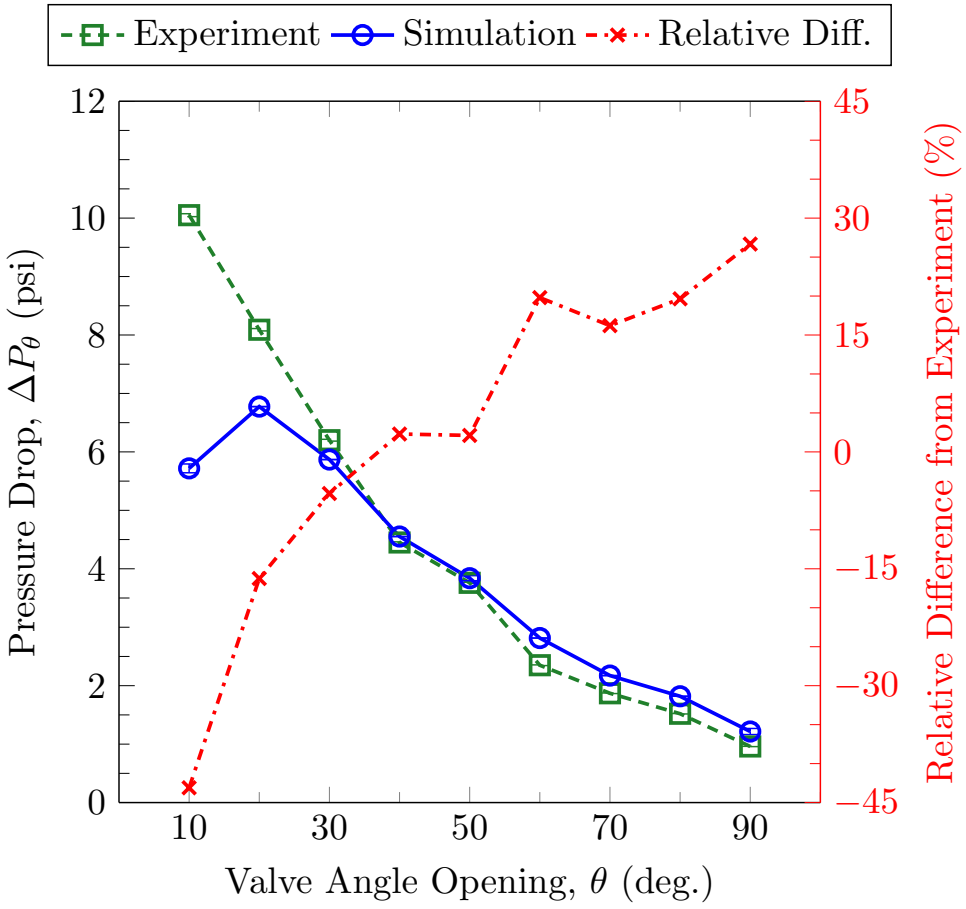

Fig. 6.30: Comparison plot of pressure drop results between the experiment and simulation.

Table 6.1: Comparison of pressure drop results between the experiment and simulation.

θ (deg.)	ΔP_θ Experiment (psi)	ΔP_θ Simulation (psi)	Relative Difference from Experiment (%)
10	10.05	5.72	-43.10
20	8.09	6.78	-16.25
30	6.20	5.87	-5.34
40	4.45	4.55	2.30
50	3.76	3.84	2.11
60	2.35	2.82	19.80
70	1.87	2.17	16.20
80	1.52	1.82	19.64
90	0.96	1.22	26.67

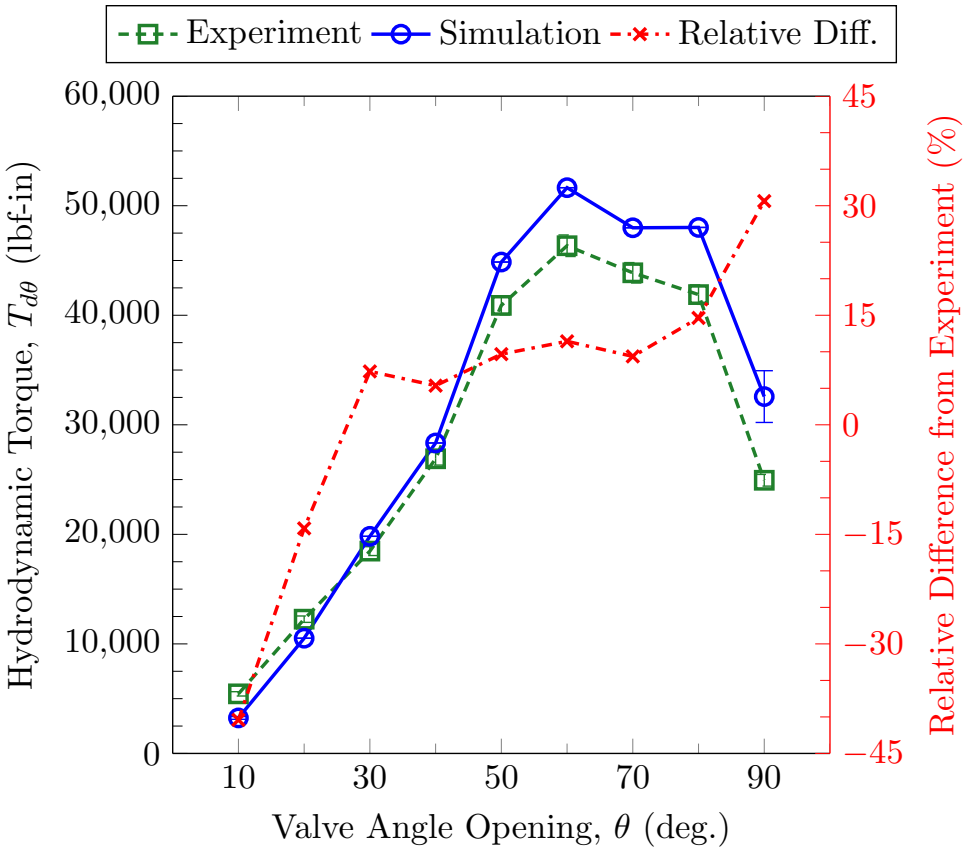

Fig. 6.31: Comparison plot of hydrodynamic torque results between the experiment and simulation.

Table 6.2: Comparison of hydrodynamic torque results between the experiment and simulation.

θ (deg.)	$T_{d\theta}$ Experiment (lbf-in)	$T_{d\theta}$ Simulation (lbf-in)	Relative Difference from Experiment (%)
10	5439.5	3241.8	-40.40
20	12256.5	10518.1	-14.18
30	18469.5	19819.8	7.31
40	26900.0	28341.3	5.36
50	40902.0	44859.2	9.67
60	46348.0	51647.4	11.43
70	43877.0	47986.3	9.37
80	41886.5	48017.3	14.64
90	24937.0	32576.7	30.64

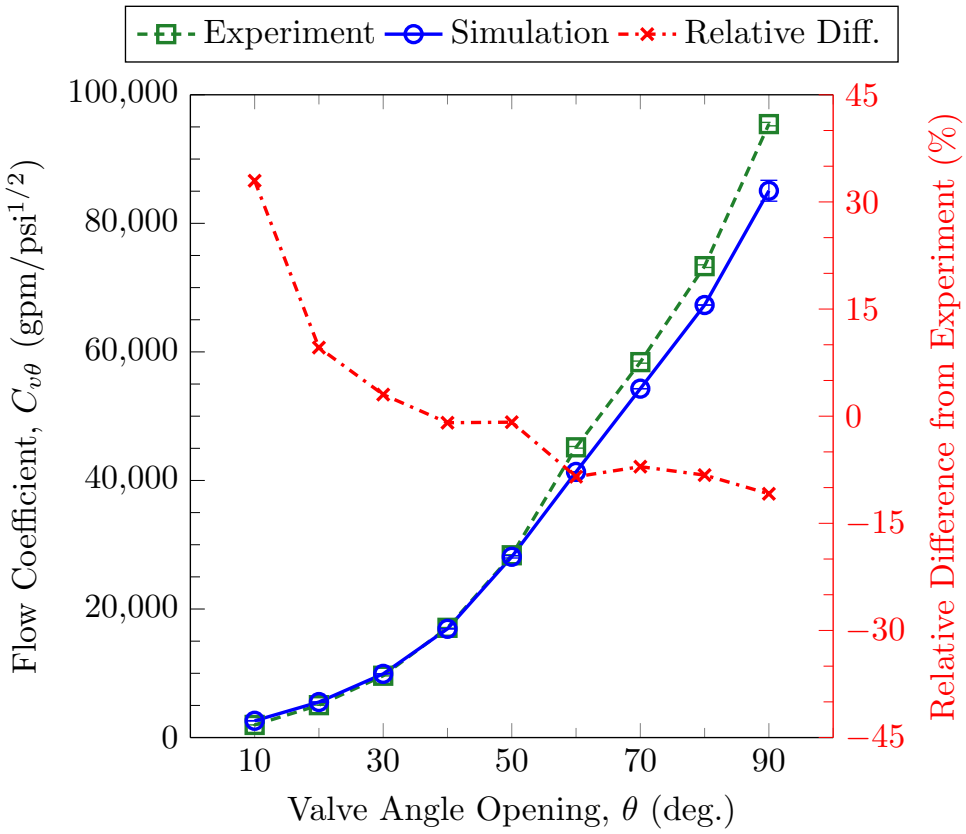

Fig. 6.32: Comparison plot of flow coefficient results between the experiment and simulation.

Table 6.3: Comparison of flow coefficient results between the experiment and simulation.

θ (deg.)	$C_{v\theta}$ Experiment (gpm/psi$^{1/2}$)	$C_{v\theta}$ Simulation (gpm/psi$^{1/2}$)	Relative Difference from Experiment (%)
10	1966.1	2614.3	32.97
20	5043.6	5528.1	9.61
30	9621.0	9912.2	3.03
40	17076.8	16920.6	-0.91
50	28362.5	28124.6	-0.84
60	45156.5	41327.8	-8.48
70	58409.9	54281.6	-7.07
80	73341.0	67291.4	-8.25
90	95438.8	85070.3	-10.86

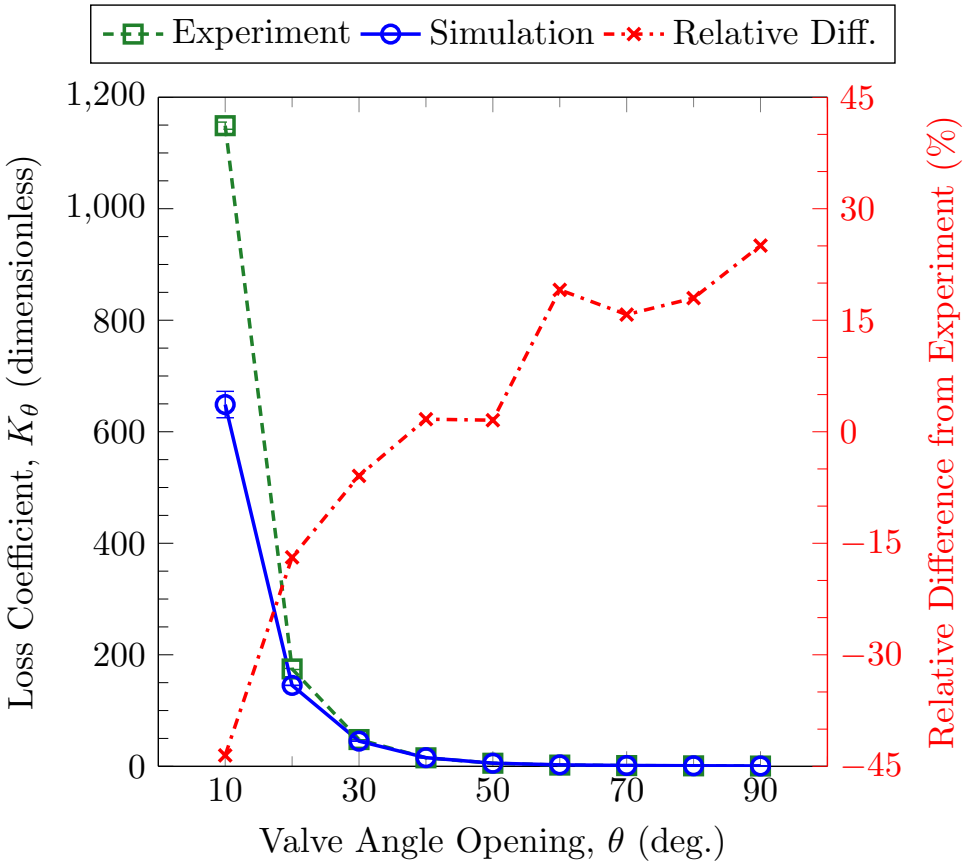

Fig. 6.33: Comparison plot of loss coefficient results between the experiment and simulation.

Table 6.4: Comparison of loss coefficient results between the experiment and simulation.

θ (deg.)	K_θ Experiment	K_θ Simulation	Relative Difference from Experiment (%)
10	1148.91	648.79	-43.53
20	174.59	145.10	-16.89
30	47.98	45.13	-5.94
40	15.23	15.49	1.69
50	5.52	5.61	1.55
60	2.18	2.60	19.09
70	1.30	1.50	15.76
80	0.83	0.98	17.98
90	0.49	0.61	25.04

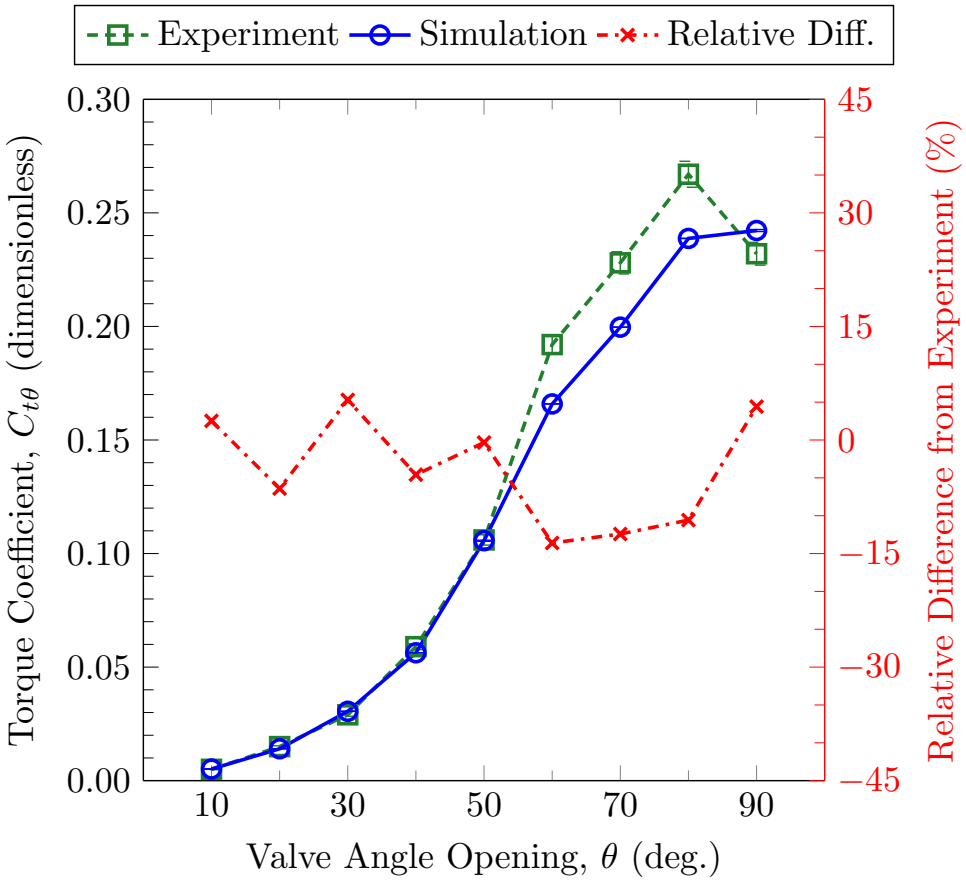

Fig. 6.34: Comparison plot of torque coefficient results between the experiment and simulation.

Table 6.5: Comparison of torque coefficient results between the experiment and simulation.

θ (deg.)	$C_{t\theta}$ Experiment	$C_{t\theta}$ Simulation	Relative Difference from Experiment (%)
10	0.0050	0.0051	2.52
20	0.0150	0.0140	-6.42
30	0.0290	0.0305	5.30
40	0.0590	0.0563	-4.58
50	0.1060	0.1056	-0.33
60	0.1920	0.1659	-13.60
70	0.2280	0.1997	-12.42
80	0.2670	0.2387	-10.58
90	0.2320	0.2422	4.41

6.3 Grid Refinement

Values for the grid sizes and step size ratios, N_1, N_2, N_3, r_{21}, and r_{32}, for each of the three cases are shown below in Table 6.6. Results from the GCI method for grid refinement discussed in Chapter 4 are tabulated in Tables 6.7 - 6.9 for the 10, 50 and 90 degree open cases.

In Tables 6.7 - 6.9, the values listed for the GCI index for each of the performance factors can be considered the amount of error in the simulation due to refinement of the mesh used. For example, based off of the three different mesh sizes used in the simulations for the 10 degree case, one can expect the value for the simulated pressure drop to be within 1.32% of $\phi_1 = 5.718$ psi as the grid is further and further refined. In this particular case, where a large disparity is seen between the experimental value and the simulated value, the error due to grid refinement is insignificant to other possible sources of error, such as turbulence modeling, boundary conditions, etc. Based off the GCI values of Tables 6.7 and 6.8, this can also be stated confidently, due to the small amount of uncertainty due to grid refinement. The GCI values for the 90 degree case in Table 6.9, exhibit slightly larger values than those found in the other two cases. However, it should be noted that more refinement could benefit the value given for the hydrodynamic torque at 90 degrees.

Table 6.6: Number of cells and step size ratios used for the GCI method for grid refinement.

θ	10	50	90
N_1	1062434	1133609	1172912
N_2	825387	875849	891431
N_3	564606	578821	589283
r_{21}	1.088	1.090	1.096
r_{32}	1.135	1.148	1.148

Table 6.7: GCI method results for grid refinement of the 10 degree open case.

ϕ	ΔP_{10} (psi)	T_{d10} (lbf-in)	C_{v10} (gpm/psi$^{1/2}$)	K_{10}	C_{t10}
Convergence	Oscillatory	Oscillatory	Monotonic	Monotonic	Oscillatory
ϕ_1	5.718	3241.8	2614.3	648.787	5.13E-03
ϕ_2	5.614	3099.7	2637.6	638.994	4.99E-03
ϕ_3	5.537	3576.8	2658.0	628.193	5.84E-03
p	11.87	10.46	8.89	4.94	15.13
ϕ_{ext}^{21}	5.778	3342.0	2593.5	667.704	5.18E-03
e_a^{21}	1.82%	4.38%	0.89%	1.51%	2.73%
e_{ext}^{21}	1.04%	3.00%	0.80%	2.83%	1.04%
GCI_{fine}^{21}	1.32%	3.87%	1.00%	3.65%	1.32%

Table 6.8: GCI method results for grid refinement of the 50 degree open case.

ϕ	ΔP_{50} (psi)	T_{d50} (lbf-in)	C_{v50} (gpm/psi$^{1/2}$)	K_{50}	C_{t50}
Convergence	Oscillatory	Oscillatory	Oscillatory	Oscillatory	Monotonic
ϕ_1	3.839	44859.2	28124.6	5.606	0.106
ϕ_2	3.894	46837.1	27936.5	5.691	0.109
ϕ_3	3.861	46764.3	28056.1	5.638	0.110
p	11.03	95.37	9.44	9.96	33.14
ϕ_{ext}^{21}	3.804	44858.7	28274.3	5.544	0.106
e_a^{21}	1.43%	4.41%	0.67%	1.52%	2.83%
e_{ext}^{21}	0.91%	0.001%	0.53%	1.13%	0.17%
GCI_{fine}^{21}	1.13%	0.001%	0.67%	1.39%	0.22%

Table 6.9: GCI method results for grid refinement of the 90 degree open case.

ϕ	ΔP_{90} (psi)	T_{d90} (lbf-in)	C_{v90} (gpm/psi$^{1/2}$)	K_{90}	C_{t90}
Convergence	Oscillatory	Monotonic	Oscillatory	Oscillatory	Monotonic
ϕ_1	1.216	35276.7	85070.3	0.613	0.242
ϕ_2	1.253	32031.7	83822.8	0.632	0.231
ϕ_3	1.166	29525.1	86914.2	0.588	0.229
p	6.93	10.37	7.33	6.81	37.947
ϕ_{ext}^{21}	1.174	37321.8	86372.9	0.591	0.242
e_a^{21}	3.04%	9.20%	1.47%	3.10%	4.55%
e_{ext}^{21}	3.55%	5.48%	1.51%	3.71%	0.14%
GCI_{fine}^{21}	4.29%	7.25%	1.91%	4.47%	0.18%

Chapter 7

Conclusion

Overall, it was found that for the pressure drop, only valve angles within 30-50 degrees were capable of predicting the experimental value within $E_{ref} \approx \pm 15\%$. For the hydrodynamic torque, valve degree openings of approximately 20-80 degrees were able to give satisfactory results within $E_{ref} = \pm 15\%$. For the flow coefficient, valve degree openings of 20-90 degrees were able to give excellent results within $E_{ref} \approx \pm 10\%$. For the loss coefficient, valve degree openings of 30-50 degrees gave excellent results within $E_{ref} = \pm 10\%$. For the torque coefficient, all valve degree openings were able to predict the experimental values within $E_{ref} = \pm 15\%$, with most within $\pm 10\%$.

The GCI indices for the performance factors on the 10, 50, and 90 degree cases were all well within 5%, with exception of the hydrodynamic torque at the 90 degree open position which was at a value above 7%. Most of the calculated GCI indices were within 2%, showing excellent grid convergence, which may be a result of the fine volumetric controls used in the CFD simulations.

7.1 Sources of CFD Uncertainty

Versteeg and Malalasekera [22] cite the main sources of error and uncertainty that are prevalent in CFD. Causes of errors include: numerical errors, coding errors, and user errors. Numerical errors refer to roundoff errors, iterative convergence errors, and discretisation errors. Coding errors refers to mistakes in the software, which is inherent in unverified CFD code. User errors refer to human errors through incorrect use of the software. For this study, quality iterative convergence was achieved and double precision was used. The verified STAR-CCM+ software was also executed by a CFD competent individual. Furthermore, the grid convergence results using the GCI method showed that the error due to discretisation

was minimal compared to other possible sources of error. Thus, it is not believed that numerical, coding and/or user errors are a significant source of error.

Causes of uncertainty include: input uncertainty and physical model uncertainty. Input uncertainty refers to inaccuracies due to limited information or approximate representation of geometry, boundary conditions, material properties, etc. Physical model uncertainties refers to discrepancies between real flows and CFD due to inadequate representation of physical or chemical processes (e.g. turbulence, combustion, etc.) or due to simplifying assumptions in the modeling process (e.g. incompressible flow, steady flow).

While it is difficult to quantify the amount of uncertainty due to any one factor, it is the author's belief that the largest amount of uncertainty in the CFD simulations presented here arise from the turbulence modeling aspect, and correct representation of boundary conditions. In general, the performance factors were observed to have larger relative differences from the experimental values when the valve was at both lower and higher valve degree openings. It may be that for very low valve angles, when the flow is restricted around the butterfly valve, the turbulence models suffer in attempting to simulate the actual turbulent behavior via the RANS equations. For higher valve angle openings, the flow rate is set to a much higher level, giving Reynolds numbers in the range of 10^6, and thus a higher amount of turbulence in the flow. Because most authors have omitted tabulated data from their studies on predicting butterfly valve performance factors (with some giving rather limited information), it is impossible to determine how well their results compare to those of this study. Only graphed results showing an overall agreement were available, which can be misleading of the quality of the results. However, Song et al. [12] and Chaiworapuek et al. [17] briefly mention seeing relative differences up to 50% for some flow performance factors. Song noticed this occurred at smaller valve angle openings. Other authors previously mentioned [10, 15], noticed a difference in using different turbulence models such as k-ω to resolve the RANS equations.

A boundary condition of large concern is the outlet boundary condition. As discussed in Chapter 2, the total length downstream of the butterfly valve was approximately 15D.

The simulation attempted to use approximately 12D with an assumed zero gradient outflow boundary condition. Knowing the exact upstream effects of the experiment's control valve downstream of the butterfly valve before exiting to atmospheric conditions, is also difficult to quantify. Ideally, if the geometry of the downstream control valve and accompanying atmospheric discharge could be modeled in the simulations, it would prove ideal over the current method used. However, due to limited information, this became a source of uncertainty due to the assumptions implemented.

7.2 Final Remarks

Computational fluid dynamics continues to be an impressive tool in helping model real world problems. However, it has its limitations which are mainly centered in turbulence modeling for incompressible applications. Due to an attempt to resolve the non-linearities that arise in the governing equations, turbulence modeling will never be exact. However, CFD can be used to give insight into visualization of complex flows, and fluid flow problems one is attempting to solve. In this study, CFD was able to model the overall behavior of fluid flow for an incompressible fluid around a butterfly valve at angles ranging from 10-90 degrees. For mid-opening valve angles (30-60 degrees), CFD was able to appropriately model all of the common performance flow factors of a butterfly valve. Using predicted results from simulated lower valve angle cases (10-20 degrees) should be avoided overall. Higher valve angles (70-90 degrees) can produce reasonably predicted values which should be used with discretion. It is worth noting however, that despite the relative differences that may occur between the simulated and experimental values, CFD simulations can be used to predict values on or near the same order of magnitude and range of the real life values one is seeking. This can be especially useful if experimental models are not available.

References

[1] Cohn, S.D., 1951, "Performance Analysis of Butterfly Valves," J. Instruments and Control Systems, **24**, pp. 880–884.

[2] McPherson, M.B., Strausser, H.S., and Williams, J.C., 1957, "Butterfly Valve Flow Characteristics," J. Hydraulics Division, **83**(1), pp. 1–28.

[3] Sarpkaya, T., 1961, "Torque and Cavitation Characteristics of Butterfly Valves," J. Applied Mechanics, **28**(4), pp. 511–518.

[4] Addy, A.L., Morris, M.J., and Dutton, J.C., 1985, "An Investigation of Compressible Flow Characteristics of Butterfly Valves," J. Fluids Engineering, **107**(4), pp. 512–517.

[5] Eom, K., 1988, "Performance of Butterfly Valves as a Flow Controller," J. Fluids Engineering, **110**(1), pp. 16–19.

[6] Kimura, T., Tanaka, T., Fujimoto, K., and Ogawa, K., 1995, "Hydrodynamic Characteristics of a Butterfly Valve - Prediction of Pressure Loss Characteristics," ISA Trans., **34**(4), pp. 319–326.

[7] Ogawa, K., and Kimura, T., 1995, "Hydrodynamic Characteristics of a Butterfly Valve - Prediction of Torque Characteristics," ISA Trans., **34**(4), pp. 327–333.

[8] Huang, C., and Kim, R.H., 1996, "Three-dimensional Analysis of Partially Open Butterfly Valve Flows," J. Fluids Engineering, **118**(3), pp. 562–568.

[9] Blevins, R.D., 1984, *Applied Fluid Dynamics Handbook*, Van Nostrand Reinhold, New York, NY, Chap. 6.

[10] Lin, F., and Schohl, G.A., 2004, "CFD Prediction and Validation of Butterfly Valve Hydrodynamic Forces," *Proceedings of the World Water and Enviornmental Resources Congress*, pp. 1–8.

[11] Hoerner, S., 1958, *Fluid-Dynamic Drag: Practical Information on Aerodynamic Drag and Hydrodynamic Resistance*, Hoerner Fluid Dynamics, CA.

[12] Song, X., Wang, L., and Park, Y., 2008, "Fluid and Structural Analysis of Large Butterfly Valve," *AIP Conference Proceedings*, **1052**, pp. 311–314.

[13] Song, X., and Park, Y.C., 2007, "Numerical Analysis of Butterfly Valve - Prediction of Flow Coefficient and Hydrodynamic Torque Coefficient," In *Proceedings of the World Congress on Engineering and Computer Science*, pp. 759–763.

[14] Leutwyler, Z., and Dalton, C., 2006, "A Computational Study of Torque and Forces Due to Compressible Flow on a Butterfly Valve Disk in Mid-Stroke Position," J. Fluids Engineering, **128**(5), pp. 1074–1082.

[15] Leutwyler, Z., and Dalton, C., 2008, "A CFD Study of the Flow Field, Resultant Force, and Aerodynamic Torque on a Symmetric Disk Butterfly Valve in a Compressible Fluid," J. Pressure Vessel Technology, **130**(2), p. 021302.

[16] Henderson, A.D., Sargison, J.E., Walker, G.J., and Haynes, J.H., 2008, "A Numerical Prediction of the Hydrodynamic Torque Acting on a Safety Butterfly Valve in a Hydro-Electric Power Scheme," WSEAS Trans. on Fluid Mechanics, **1**(3), pp. 218–223.

[17] Chaiworapuek, W., Champagne, J., El Haj em, M., and Kittichaikan, C., 2010, "An Investigation of the Water Flow Past the Butterfly Valve," *AIP Conference Proceedings*, **1225**, pp. 249–262.

[18] Feng, W., Xiao, G., and Song, L., 2009, "Numerical Simulation of the Flow Field to the Double Eccentric Butterfly Valve and Performance Prediction," In *Power and Energy Engineering Conference*, pp. 1–4.

[19] Bosserman, B.E., Ali, A., Schuraytz, I.M., 2012, *Butterfly Valves: Torque, Head Loss, and Cavitation Analysis AWWA Manual; M49*, 2nd ed., American Water Works Association, Denver, CO.

[20] Cengel, Y., and Cimbala, J., 2009, *Fluid Mechanics: Fundamentals and Applications*, 2nd ed., McGraw-Hill Companies, Inc., New York, NY.

[21] Coleman, H.W., and Steele, W.G., 2009, *Experimentation, Validation, and Uncertainty Analysis for Engineers*, 3rd ed., John Wiley and Sons, Inc., Hoboken, NJ.

[22] Versteeg, H.K., and Malalasekera, W., 2007, *An Introduction to Computational Fluid Dynamics: The Finite Volume Method*, 2nd ed., Pearson Education Limited, London, England.

[23] Kundu, P., and Cohen, I., 2010, *Fluid Mechanics*, 4th ed., Academic Press Elsevier, Burlington, MA.

[24] *STAR-CCM+ Ver. 7.04.006 User Guide*, 2012, CD-Adapco.

[25] Celik, I.B., Ghia, U., Roache, P.J., and Freitas, C.J., *Journal of Fluids Engineering Procedure for Estimation and Reporting of Uncertainty Due to Discretization in CFD Applications*, from http://journaltool.asme.org/Content/JFENumAccuracy.pdf.

[26] *Journal of Fluids Engineering Editorial Policy Statement on the Control of Numerical Accuracy*, from http://journaltool.asme.org/Content/JFENumAccuracy.pdf.

[27] Shah, R.K., and Bhatti, M.S., 1987, *Handbook of Single-Phase Convective Heat Transfer*, Wiley Interscience, New York, NY, Chap. 3.

[28] Zhi-qing, W., 1982, "Study on Correction Coefficients of Laminar and Turbulent Entrance Region Effect in Round Pipe," Applied Mathematics and Mechanics, **3**, pp. 433–446.

Appendices

Appendix A

Uncertainty of Experimental Data

Uncertainty in general terms can be defined as the range in which one expects results from an experiment to be at a specified confidence interval. In experiments, it is often common to consider uncertainty regarding directly measured values (i.e. Q, ΔP_θ, etc.) and results (i.e. $C_{v\theta}$, K_θ, $C_{T\theta}$, $T_{d\theta}$, etc.) which can be a function of those measured values. Every measured value in an experiment has some degree of uncertainty which must be taken into consideration. Uncertainties originate from systematic and random errors. Systematic errors consist of effects that do not vary throughout a measurement period, such as bias, digital resolution, etc. Random uncertainties consist of all the effects that do vary throughout a measurement period, such as the repeatability of a sensor, random noise in the measurement, statistical scatter, etc. While systematic errors are consistent for any given sensor, random errors can be reduced by taking additional measurements.

A common method for carrying out a general uncertainty analysis involves using the Taylor Series Method (TSM) for propagation of uncertainties [21]. This usually involves considering a result, r, as a function of several variables

$$r = r(X_1, X_2, ..., X_N). \tag{A.1}$$

The combined standard uncertainty at 95% confidence interval, U_{95}, is given as

$$U_{95} = 2\left[\sum_{i=1}^{N}\left(\frac{\partial r}{\partial X_i}\right)^2 ({b_{X_i}}^2 + {s_{X_i}}^2)\right]^{1/2} \tag{A.2}$$

where b_{X_i} and s_{X_i} are the systematic and random standard uncertainties, respectively. In this study, the correlated systematic and random errors are deemed as insignificant when

compared to uncorrelated systematic errors. Under these simplifications, Eqn. A.2 becomes

$$U_{95} = \left[\sum_{i=1}^{N} \left(\frac{\partial r}{\partial X_i} \right)^2 {U_i}^2 \right]^{1/2} \tag{A.3}$$

where each U_i is the large-sample 95% expanded uncertainty for variable X_i. Equation A.3 describes the propagation of the overall uncertainties in the measured variables into the overall uncertainty of the result. This is commonly termed general uncertainty analysis. Another useful variation of Eqn. A.3 involves relative uncertainties, U_i/X_i, such that

$$U_{95} = \left[\sum_{i=1}^{N} \left(\frac{\partial r}{\partial X_i} X_i \right)^2 \left(\frac{U_i}{X_i} \right)^2 \right]^{1/2}. \tag{A.4}$$

A very useful specific form of Eqn. A.4 involves a data reduction equation with the form

$$r = k X_1^a X_2^b X_3^c \cdots \tag{A.5}$$

where the exponents may be positive or negative constants, k is a constant, the X_i terms represent directly measured variables. Application of Eqn. A.4 to the relationship of Eqn. A.5 gives

$$\frac{U_r}{r} = \left[a^2 \left(\frac{U_{X_1}}{X_1} \right)^2 + b^2 \left(\frac{U_{X_2}}{X_2} \right)^2 + c^2 \left(\frac{U_{X_3}}{X_3} \right)^2 + \cdots \right]^{1/2} \tag{A.6}$$

which avoids the need to calculate any partial derivative terms of Eqn. A.3 or perform any subsequent algebraic manipulation. Equation A.6 will be used specifically for doing expanded uncertainty analysis on the butterfly valve performance factors $C_{v\theta}$, K_θ, and $C_{T\theta}$, which are of the form in Eqn. A.5. The uncertainty analysis for the hydrodynamic torque, $T_{d\theta}$, will be carried out first by using Eqn. A.4.

A.1 Experimental Uncertainty of Hydrodynamic Torque

For the calculated hydrodynamic torque, $T_{d\theta}$, from Eqn. 1.7, it is observed that $T_{d\theta} = T_{d\theta}(T_{to\theta}, T_{tc\theta})$. Using Eqn. A.4 we then have

$$U_{T_{d\theta}} = \left[\left(\frac{\partial T_{d\theta}}{\partial T_{to\theta}} T_{to\theta} \right)^2 \left(\frac{U_{T_{to\theta}}}{T_{to\theta}} \right)^2 + \left(\frac{\partial T_{d\theta}}{\partial T_{tc\theta}} T_{tc\theta} \right)^2 \left(\frac{U_{T_{tc\theta}}}{T_{tc\theta}} \right)^2 \right]^{1/2}. \tag{A.7}$$

After calculating the partial derivatives and substituting them into Eqn. A.8 , both sides are divided by $T_{d\theta}$, to get the relative uncertainty of the hydrodynamic torque on the left hand side, such that

$$\frac{U_{T_{d\theta}}}{T_{d\theta}} = \left[\left(\frac{1}{2} \frac{T_{to\theta}}{T_{d\theta}} \right)^2 \left(\frac{U_{T_{to\theta}}}{T_{to\theta}} \right)^2 + \left(\frac{1}{2} \frac{T_{tc\theta}}{T_{d\theta}} \right)^2 \left(\frac{U_{T_{tc\theta}}}{T_{tc\theta}} \right)^2 \right]^{1/2}. \tag{A.8}$$

A.2 Experimental Uncertainty of Flow Coefficient

For the calculated flow coefficient, $C_{v\theta}$, from Eqn. 1.8, it is observed that $C_{v\theta} = C_{v\theta}(Q, \Delta P_\theta)$, since the uncertainty of the physical property SG is of such low magnitude relative to Q and ΔP_θ [21]. Because $C_{v\theta}$ is of the form in Eqn. A.5, application of the expanded uncertainty of Eqn. A.6 gives

$$\frac{U_{C_{v\theta}}}{C_{v\theta}} = \left[\left(\frac{U_Q}{Q} \right)^2 + \left(\frac{1}{4} \right) \left(\frac{U_{\Delta P_\theta}}{\Delta P_\theta} \right)^2 \right]^{1/2}. \tag{A.9}$$

It should be noted that from inspection of Eqn. A.9, the relative uncertainty of the flow coefficient is four times more sensitive to the relative uncertainty of the volume flow rate than the pressure drop. Furthermore, because the relative uncertainties for the volume flow rate and pressure drop are constant, the relative uncertainty for flow coefficient will also be constant.

A.3 Experimental Uncertainty of Loss Coefficient

For the calculated loss coefficient, K_θ, from Eqn. 1.9, it is observed that $K_\theta = K_\theta(\Delta P_\theta, V_{avg})$, since the uncertainty of the physical property ρ is of such low magnitude relative to ΔP_θ

and V_{avg}. Because K_θ is of the form in Eqn. A.5, the expanded uncertainty of Eqn. A.6 is used such that

$$\frac{U_{K_\theta}}{K_\theta} = \left[\left(\frac{U_{\Delta P_\theta}}{\Delta P_\theta} \right)^2 + (4) \left(\frac{U_{V_{avg}}}{V_{avg}} \right)^2 \right]^{1/2}. \tag{A.10}$$

Prior to solving for the relative uncertainty of the loss coefficient, the relative uncertainty of V_{avg} must be determined. The average velocity is defined as

$$V_{avg} = QA, \tag{A.11}$$

where Q is the volume flow rate and A is the cross-sectional area of the pipe flow. Because the uncertainty of A is much lower in magnitude than the uncertainty of Q, it is safely assumed that $V_{avg} = V_{avg}(Q)$, which by using Eqn. A.6 leads to the trivial case in which the relative uncertainty of V_{avg} is equal to the relative uncertainty of Q. It should be noted that from inspection of Eqn. A.10, the relative uncertainty of the loss coefficient is four times more sensitive to the relative uncertainty of the average velocity (which is equal to the relative uncertainty of the volume flow rate) than the relative uncertainty of the pressure drop.

A.4 Experimental Uncertainty of Torque Coefficient

For the calculated torque coefficient, $C_{t\theta}$, from Eqn. 1.12, it is observed that $C_{t\theta} = C_{t\theta}(T_{d\theta}, \Delta P_\theta)$, since the uncertainty of the the pipe diameter, D, is of such low magnitude relative to $T_{d\theta}$ and ΔP_θ. Because $C_{t\theta}$ is of the form in Eqn. A.5, the expanded uncertainty of Eqn. A.6 is used such that

$$\frac{U_{C_{t\theta}}}{C_{t\theta}} = \left[\left(\frac{U_{T_{d\theta}}}{T_{d\theta}} \right)^2 + \left(\frac{U_{\Delta P_\theta}}{\Delta P_\theta} \right)^2 \right]^{1/2}. \tag{A.12}$$

A.5 Results

The performance factor relative uncertainties were calculated by substituting in the known relative uncertainties and the measured values given in Table 2.1. The calculated relative uncertainties for all nine butterfly valve experiment cases are provided in Table 2.3.

Appendix B

Periodic Flow Simulation

Hydrodynamic entry lengths for reaching fully developed turbulent flow for internal flows has been approximated as:

$$L_{h,turbulent} = 1.359 Re^{1/4} D \tag{B.1}$$

where Re is Reynolds number and D is the internal diameter of the pipe flow being considered [27, 28]. Reynolds numbers concerning this study in the range of 10^5 to 10^6 yield hydrodynamic entry lengths of approximately 24D and 43D, respectively, which are considerably long lengths to model computationally. Many pipe flows of practical engineering interest require a pipe length of about 10D, where the entrance effects become insignificant. Using such a model upstream of the butterfly valve with CFD would be computationally expensive and would require trial and error to reach a fully developed profile that matches the measured flow characteristics from the experiment in Table 2.1. To alleviate this problem, a periodic flow simulation was devised.

A periodic flow simulation can allow for the continuous interfacing of two different boundaries, such as an inlet and outlet for simple pipe flow. This causes the flow conditions at the outlet to become the flow conditions at the inlet continuously, which is useful in the rapid development of fully developed flow conditions for internal flow. In order for periodic flow to function properly, a pressure drop or mass flow rate must be specified to force the solution to the specified conditions in a steady state case. In this study, the pressure drop was specified instead of the mass flow rate. Forcing the flow to match a specified flow rate would have been more desirable since the experimental volume flow rate and fluid properties are known. However, in attempting to specify the mass flow rate initially, it was soon discovered that the converged simulations consistently resulted

in invalid solutions which didn't represent fully developed flow profiles, such as asymmetry in the velocity distributions. CD-Adapco, the distributor of STAR-CCM+ was contacted regarding the problem and is investigating the issue. Consequently, the pressure drop was specified, which required iteration in order to achieve the desired volume flow rate and its corresponding flow characteristics. For the periodic flow simulations carried out, a short cylinder of length 1.5 m with the same diameter as the experiment, was modeled and meshed as seen in Fig. B.1. The meshing and physics models used, as well as their options will now be discussed below.

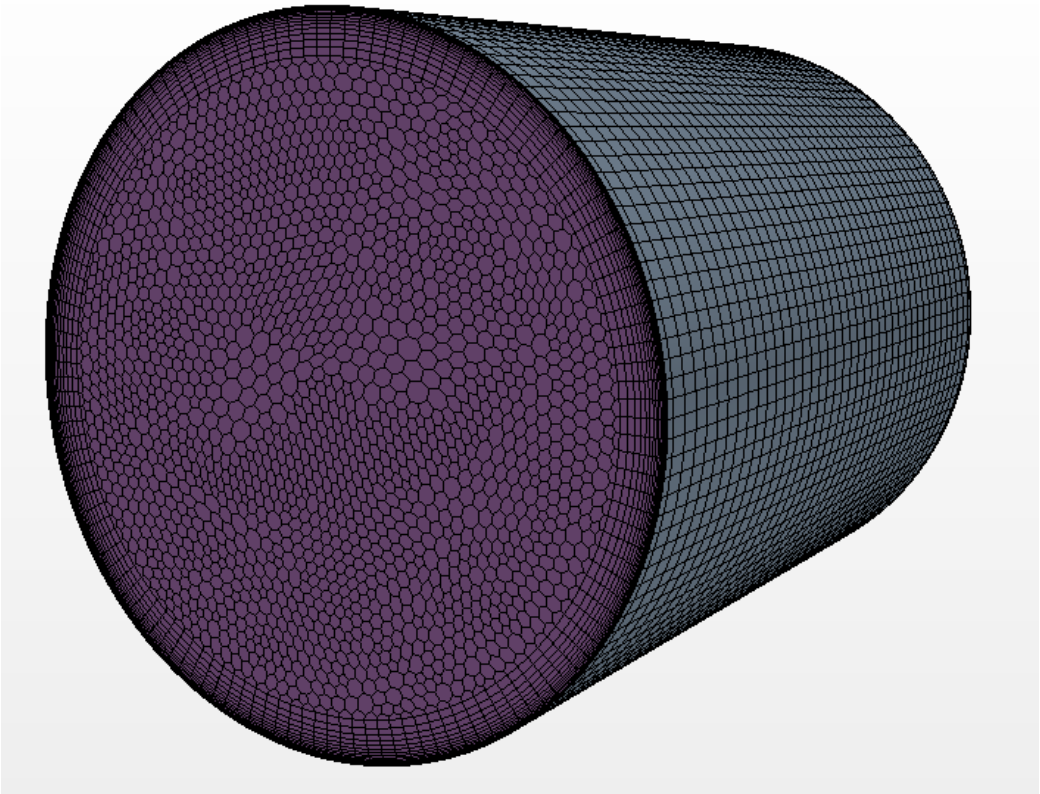

Fig. B.1: Volume mesh representation of the periodic flow simulations.

B.1 Meshing

The following meshing models were selected for the meshing continuum: polyhedral mesher, prism layer mesher, and surface remesher. All of these meshing models have been previously mentioned and discussed in 4.3, with exception to the volumetric controls. In addition, all of their selected parameters and options were identical to those specified in the same chapter. Additional information regarding the meshing models can be found in Appendix C. Reference values for the periodic flow simulations are identical to those listed in Table 4.1, with exception to the wrapper feature angle and scale factor which aren't available options, due to omission of the surface wrapper meshing model.

B.2 Physics

The same physics models and options described in 5.1, were used for the periodic flow simulation. Additional information regarding the physics model options and parameters can be found in Appendix D. Fully developed periodic flow conditions were set between the inlet and outlet of the cylinder for a specified pressure drop and solved.

B.3 Results

The simulation iterates until convergence, or reaching a steady state, at which point the volume flow rate is calculated and compared to the experimental data. The velocity flow profile is also inspected to verify a fully developed flow profile as seen in Fig. B.2 and B.3. If the periodic simulation and experimental volume flow rates do not match, the process is repeated by specifying a different pressure drop across the simulation by iteration until they do. If the volume flow rates match, the following scalar and vector values are extracted from the simulation and used as necessary inlet conditions for the butterfly valve simulations: turbulent dissipation rate, turbulent kinetic energy, and velocity. The process is then repeated for all nine butterfly valve simulation cases.

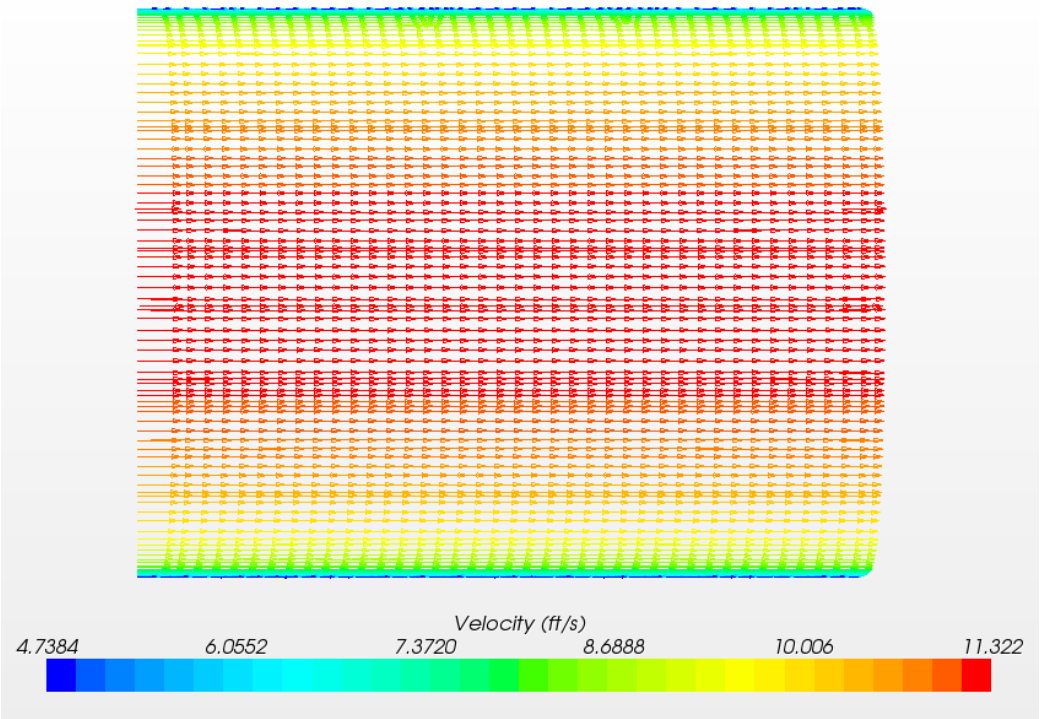

Fig. B.2: Cross-section velocity vectors for a periodic flow simulation.

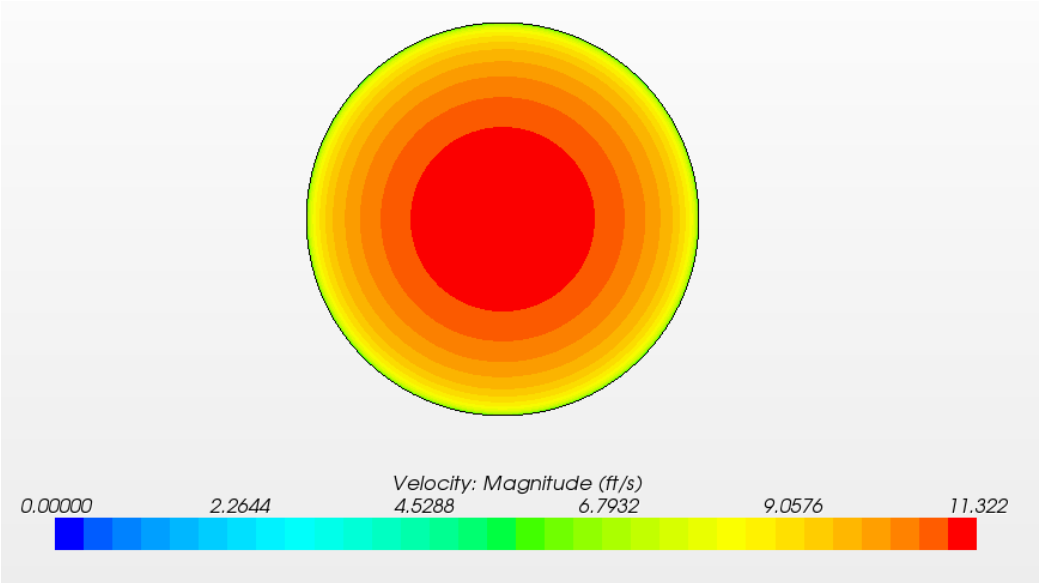

Fig. B.3: Velocity scalars along the direction of flow for a periodic flow simulation.

Appendix C

STAR-CCM+ Meshing Parameters and Options

This appendix provides additional details regarding the specific options and parameters of the STAR-CCM+ meshing models used in this study. Additional information is available in the STAR-CCM+ user's manual [24].

C.1 Polyhedral Mesher

- Run optimizer option: improves the quality of the overall mesh by running a vertex-based optimizer.

C.2 Extruder

- Constant rate normal extrusion type: ensures a constant thickness ratio between one cell layer and the next depending on the stretching parameter chosen. The extrusion will also project out normal from surface origin of extrusion.
- Average Normal Extrusion Option: forces the extruder to compute an average face normal across the the whole boundary origination.
- Number of Layers Parameter: determines the number of cells in the direction of extrusion.
- Stretching Parameter: the ratio of the length of the final extrusion cells to the length of the first extrusion cells. A value greater than one means as layers of extrusions away from the origin of extrusion increases, so does the length of each subsequent extrusion layer, resulting in a less compact layer of orthogonal cells toward the end of the extrusion.

- Magnitude Parameter: the total length of the extrusion.
- Create a New Region Option: when checked, a new region will be added to interact within the entire region continuum. When the extrusion is finally created, an automatic internal interface boundary is created between the original boundary ending of the first region and the new boundary beginning of the second region so that there is no disruption in the continuum.

C.3 Prism Layer Mesher

- Geometric Progression Stretching Function: the thickness of each cell layer is calculated based around a constant size ratio from one layer to the next.
- Stretch Factor Stretching Mode: for the geometric progression stretching function, the stretch factor is the ratio of the thickness of one cell layer to the thickness of the cell layer beneath it as one moves away from the wall.
- Gap Fill Percentage: the maximum proportion of a gap that can be occupied by a prism layer mesh, since it is possible a prism layer could become larger than a gap in a narrow passage.
- Minimum Thickness: the smallest prism layer thickness allowed below which the thickness of a prism layer would have to be forced to zero in order to prevent poor cell quality due to squeezing several prism layers into a thin section.
- Layer Reduction: controls the point at which the number of layers within a contracting prism layer is reduced due to corners, narrowing gaps, curved surfaces, etc.
- Boundary March Angle: specifies the deviation from the normal that is allowed in order for the subsurface to be successfully generated along a boundary that doesn't have any thickness specified for it.
- Concave and Convex Angle Limit: allows subsurfaces to be automatically retracted in areas where the surface edge angle is less than the concave angle limit or greater than

the convex angle limit in order to improve the prism layer mesh quality in narrow wedge-like regions. Using the default values of 0 and 360 for the concave and convex angle limits, respectively, disables them.

- Near Core Layer Aspect Ratio: improves the transition from the prism layer to the core mesh, which in this case is a polyhedral mesh.

- Improve Subsurface Quality Option: causes retriangulation of boundary surfaces that do not have prism layers after the subsurface stage of the volume meshing process, resulting in a better quality mesh.

C.4 Surface Wrapper

- Curvature Refinement Option: allows cell refinement based on the number of points around a circle or curve and the curvature deviation distance.

- Proximity Refinement Option: allows the specification of cell refinement based on a search distance and the number of points in a gap.

C.5 Surface Remesher

- Curvature Refinement Option: allows cell refinement based on the number of points around a circle or curve and the curvature deviation distance.

- Proximity Refinement Option: allows the specification of cell refinement based on a search distance and the number of points in a gap.

- Compatibility Refinement Option: imposes a surface growth rate of two to limit the difference in face sizes across a gap.

- Retain Geometric Features Option: aims to preserve all CAD edges when generating a surface mesh, which provides a better representation of the original CAD model. This also makes the CAD projection process more efficient, as a face on the surface mesh will not span multiple CAD surfaces.

- Create Aligned Meshes Option: generates a surface mesh with face edges that aim to follow the curvature of rounded CAD features, such as fillets.

- Minimum Face Quality Parameter: property value that ranges from 0 to 1, with 0 being the worst and 1 being perfect. The quality of a triangle is calculated by comparing the area of the face to the area of an equilateral triangle that would fit inside a circle touching the three corner points of the original face.

- Enable Automatic Surface Repair Option: provides an automatic procedure for correcting a range of geometric type problems that may exist in the remeshed surface once the surface remeshing process is complete. This criteria for determining correction is based on pierced faces, surface proximity, and surface quality.

C.6 Reference Values

- Base Size: is a characteristic dimension of the model that other meshing parameters use as a relative value reference.

- Automatic Surface Repair Minimum Proximity: specifies the minimum proximity value which all faces should have after fixing.

- Automatic Surface Repair Minimum Quality: specifies the minimum value which all faces should have after fixing which can range from 0 (worst) to 1 (perfect). The quality of a triangle is given by 2r/R where r is the radius of the circle that fits inside the triangle and R is the radius of the circle that passes through the three corner points of the triangle.

- CAD Projection: when enabled, allows vertices to be projected back to the imported CAD surface during surface wrapping and/or surface remeshing, which results in a surface definition closer to the original.

- Number of Prism Layers: sets the number of cell layers that are generated within the prism layer on a boundary surface.

- Prism Layer Stretching: ratio of the thickness of one cell layer to the thickness of the cell layer beneath it, moving away from the wall.
- Prism Layer Thickness: total overall thickness of all the prism layers.
- Enable Curvature deviation distance: when enabled, allows the curvature deviation distance value to be prescribed by the user. This value is the maximum distance permitted between the center of any mesh edge and its associated input surface.
- Basic Curvature: defines the approximate number of triangles for a surface or cell that would be used around a 360 degree cylindrical surface.
- Surface Growth Rate: controls the rate at which triangle edges sizes can vary from one cell to its neighbor.
- Surface Proximity # of points in gap: used for specifying the refinement for surfaces that are close to one another.
- Surface Proximity Search Floor: represents the minimum size gap to be considered for proximity refinement.
- Surface Relative Minimum Size: sets the minimum surface size possible relative to the base size.
- Surface Relative Target Size: sets the desired surface meshing size relative to the base size.
- Tet/Poly Density: changes the overall density of the mesh everywhere in the bulk volume.
- Tet/Poly Growth Factor: changes the rate at which cells grow/blend from coarse to fine areas.
- Tet/Poly Volume Blending Factor: controls the mesh density transition when volumetric controls overlap or are in close proximity to the surface mesh boundary or

interface. Used to avoid sharp transitions in mesh density which could lead to numerical instability in the simulation.

- Wrapper Feature Angle: determines whether feature edges within the import surface geometry are maintained or not in the wrapped surface.
- Wrapper Scale Factor: property that is applied to all refinement sizes which scales by a common factor during the surface wrapping process allowing for quick and easy alteration of all the surface refinement inputs that have currently been set for each region that is linked to the surface wrapper continuum model.

Appendix D

STAR-CCM+ Physics Parameters and Options

This appendix provides additional details regarding the specific options and parameters of the STAR-CCM+ physics models used in this study. Additional information is available in the STAR-CCM+ user's manual [24].

D.1 Gradients

- Verbose Option: provides additional output while the simulation is running and can be useful for debugging problems that occur.
- Gradient Method: specifies which gradient method to use: Hybrid LSQ-Gauss or Green-Gauss.
- Limiter Method: specifies which limiter method to use: Venkatakrishnan or Modified Venkatakrishnan.
- Least-Squares Quality Criterion Option: when enabled, gradient corrections are made for cells with poor least-squares tensor quality.
- Flat Cells Curvature Criterion Option: when enabled, gradient corrections are made for flat cells with sensible curvature.
- Cell Skewness Criterion Option: when enabled, gradient corrections are made for cells with a large skewness angle.
- Chevron-Cell Criterion Option: when enabled, gradient corrections are made for all chevron cells, which are pairs of thin slender cells sharing a common face that are bent at an angle such that the line joining the cell centers does not pass through the common face.

- Least-Squares Tensor Minimum Eigenvalues Ratio: minimum admissible value of ratio between the minimum and maximum eigenvalue of the least-squares tensor.
- Normalized Flat Cells Curvature Factor: acceptable ratio between the tangent of cell-skewness angle and the aspect ratio of the cell.
- Maximum Safe Skewness Angle: value below which no related specific corrections are applied to least-squares computed gradients.
- Minimum Unsafe Skewness Angle: value above which all negative skewness angle cells and gradients are corrected to ensure robustness.

D.2 Segregated Flow

- Convection Scheme: the manner in which the face values scalars are computed from one cell value to the next. Different schemes include: first-order upwind, second-order upwind, central-differencing, bounded central-differencing, blended upwind/central, hybrid second-order upwind/central, and hybrid second-order upwind/bounded-central.
- Minimum Absolute Pressure: minimum allowed absolute pressure for compressible flows (not applicable).
- Flow Boundary Diffusion: when enabled, allows flow-boundary diffusion fluxes or viscous fluxes for flow models.
- Secondary Gradients: when enabled, includes interior and boundary diffusion gradients.
- Delta-V Dissipation: when enabled, allows a robust treatment of porous media and similar large body forces by making the segregated solver behave more like the coupled solver, and fixing checker-boarding at a porous/non-porous interface (not applicable).

D.3 Realizable k-ϵ Two-Layer

- Two-Layer Type: selects a two-layer formulation for the k-ϵ model. Options include: shear driven (Wolfstein or Norris-Reynolds) for flows not dominated by buoyancy forces and buoyancy driven (Xu) for flows dominated by buoyancy forces.

- Convection Scheme: the manner in which the face values scalars are computed from one cell value to the next. Different schemes include: first-order upwind, second-order upwind, central-differencing, bounded central-differencing, blended upwind/central, hybrid second-order upwind/central, and hybrid second-order upwind/bounded-central.

- Normal Stress Term Option: when enabled, allows a directly incorporated divergence and turbulent kinetic energy term for the full Boussinesq approximation in compressible flows (not applicable).

- Two-Layer ReY*: defines the limit of applicability of the two-layer formulation.

- Two-Layer Delta ReY: constant used in determining the width of the blending function.

- Secondary Gradients: when enabled, includes interior and boundary diffusion gradients.

- Buoyancy Production of Dissipation: determines how coefficient $C_{3\epsilon}$ is calculated.

- $C_\mu, C_{1\epsilon}, C_{2\epsilon}, C_t, \sigma_k, \sigma_\epsilon$, Sarkar: standard k-ϵ model coefficients.

- Tke Minimum: the minimum allowable turbulent kinetic energy.

- Tdr Minimum: the minimum allowable turbulent dissipation rate.

D.4 Reference Values

- Minimum Allowable Wall Distance: minimum allowable wall distance in the fluid continuum so as to avoid numerical instability that results from boundary sliver cells close to zero.

- Reference Pressure: the absolute pressure value relative to which all other pressures (gauge) are defined. In this study, the reference pressure is input as the measured pressure 2D upstream from the butterfly valve in Table 2.1. All absolute pressure are scaled from this point in the simulations.

Appendix E

CFD Flow Visualizations

This appendix provides visualizations of the flow field for the absolute pressure and the velocity vectors for every valve opening angle simulated, presented along two planes intersecting the flow domain: one perpendicular to the angle of rotation, and another parallel to the angle of rotation for the butterfly valve, referred henceforth as the top and side views, respectively. These visualizations are shown in Figs. E.1 - E.72. Detailed views of the region surrounding the valve are also provided in the mentioned figures, in order to allow greater clarity regarding the characteristics of the flow. Discussion regarding some of these figures is provided in Chapter 6.

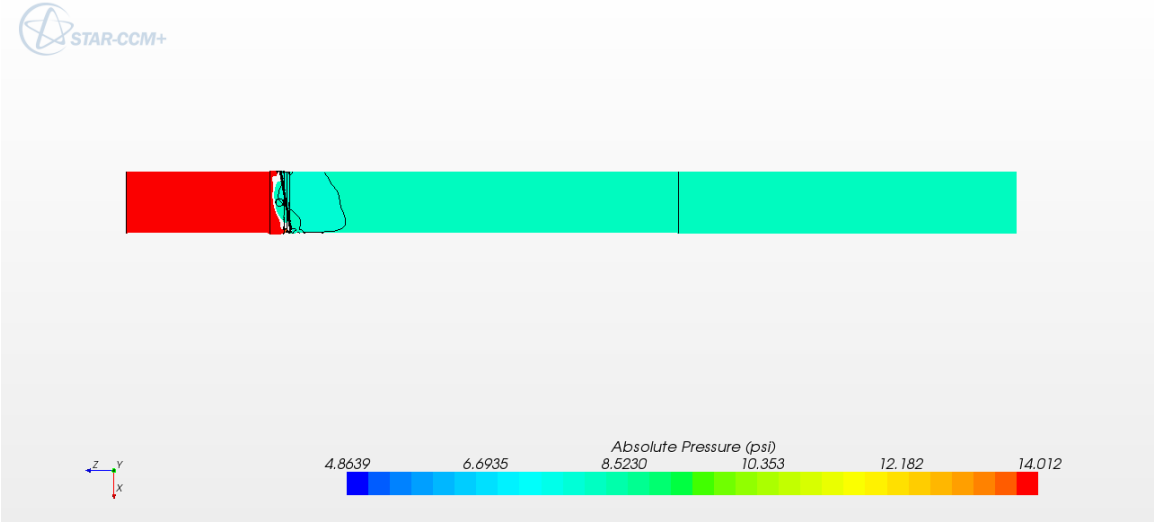

Fig. E.1: Top view of absolute pressure across the entire flow domain for the 10 degree open case.

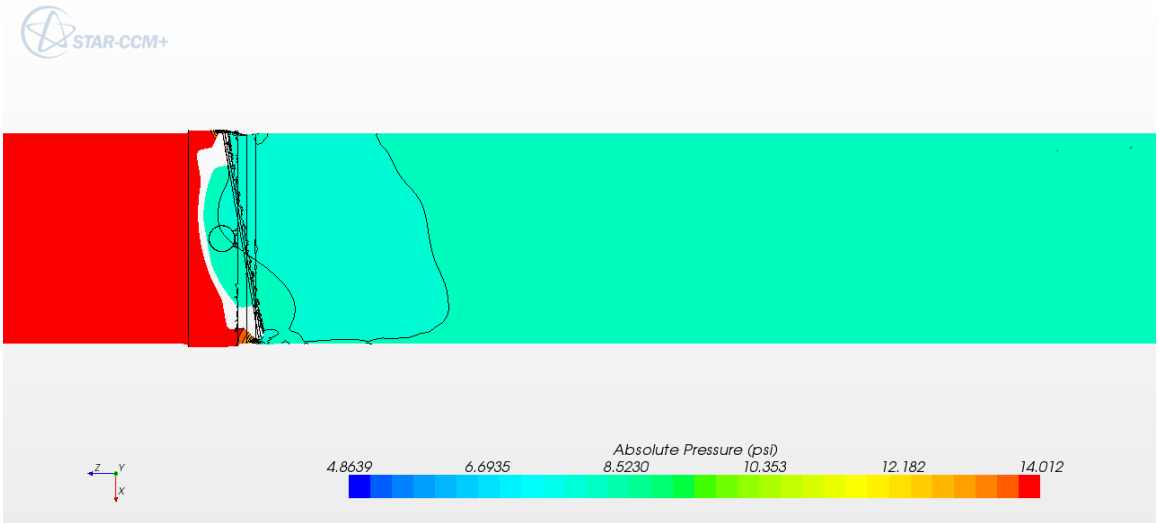

Fig. E.2: Detailed top view of absolute pressure across the butterfly valve for the 10 degree open case.

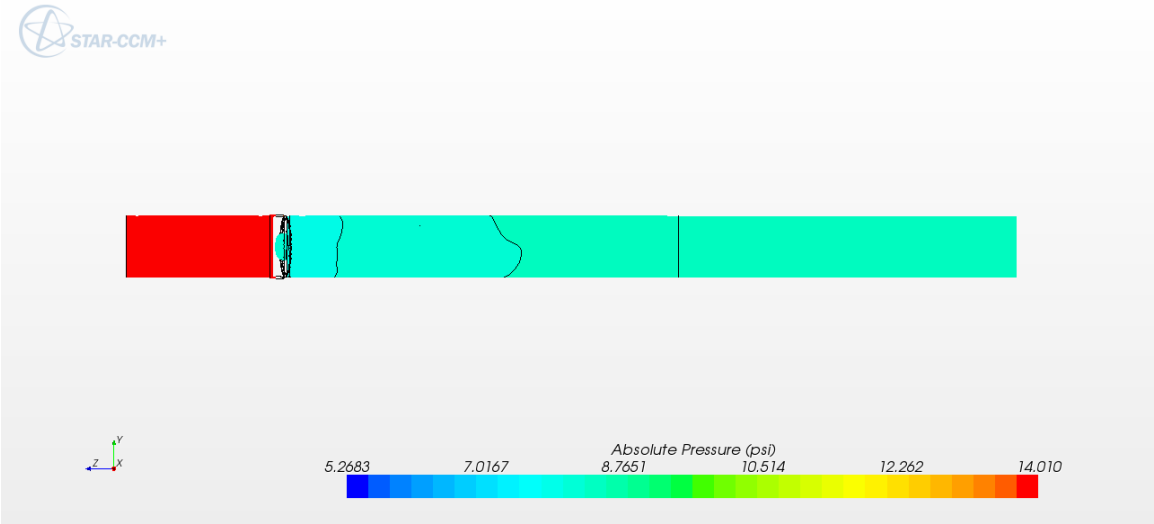

Fig. E.3: Side view of absolute pressure across the entire flow domain for the 10 degree open case.

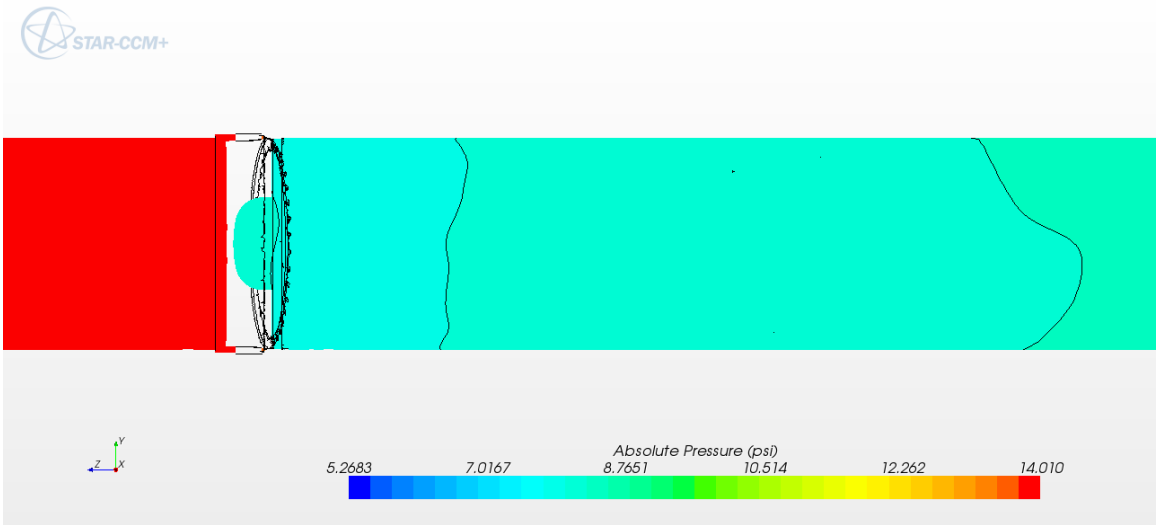

Fig. E.4: Detailed side view of absolute pressure across the butterfly valve for the 10 degree open case.

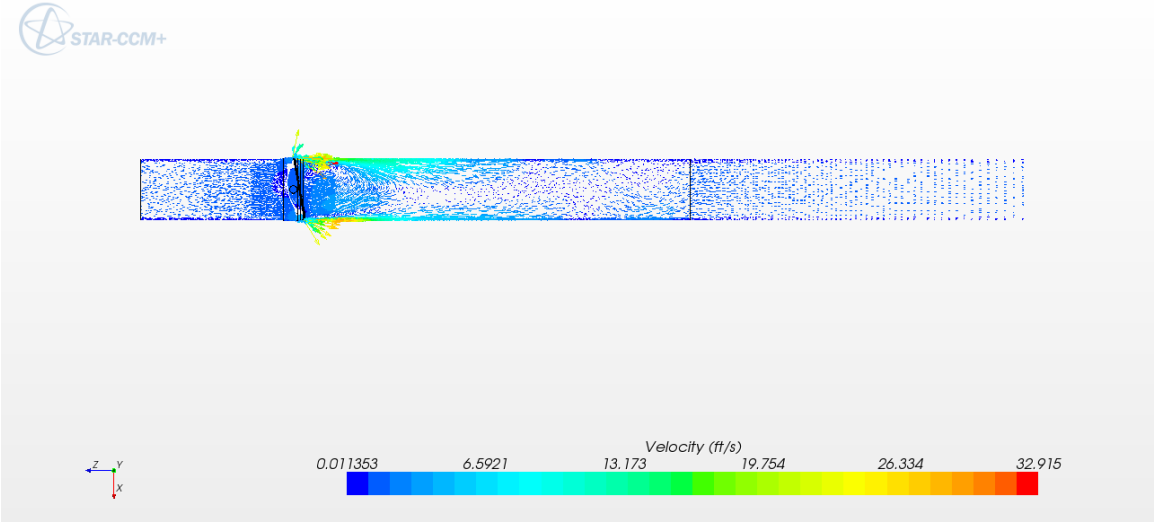

Fig. E.5: Top view of velocity vectors across the entire flow domain for the 10 degree open case.

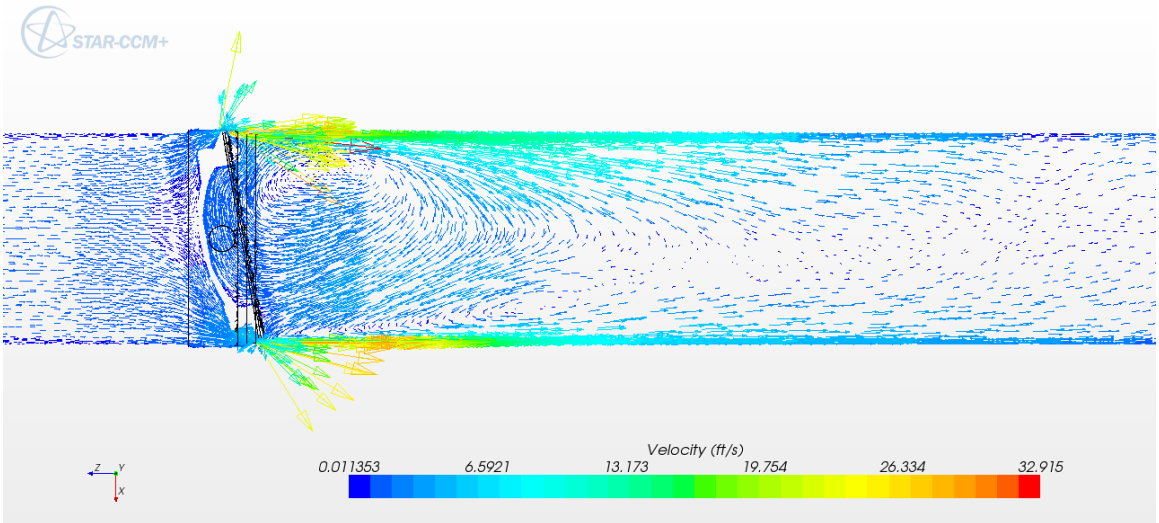

Fig. E.6: Detailed top view of velocity vectors across the butterfly valve for the 10 degree open case.

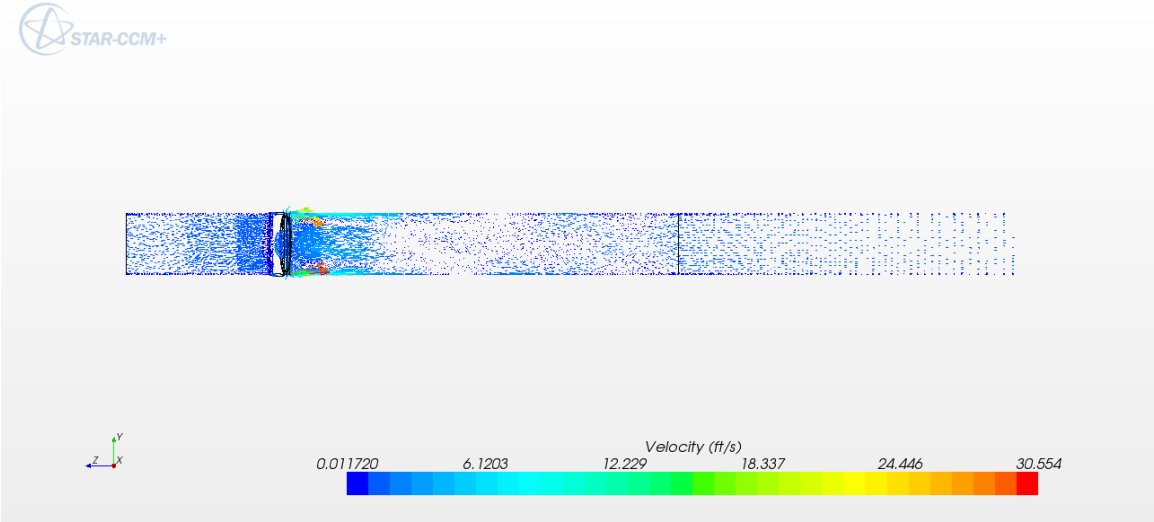

Fig. E.7: Side view of velocity vectors across the entire flow domain for the 10 degree open case.

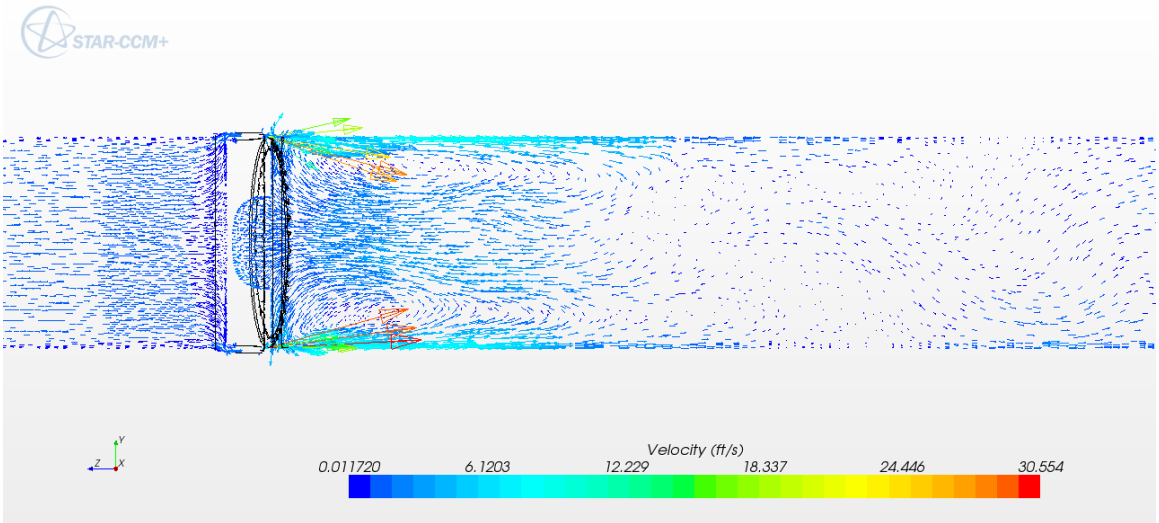

Fig. E.8: Detailed side view of velocity vectors across the butterfly valve for the 10 degree open case.

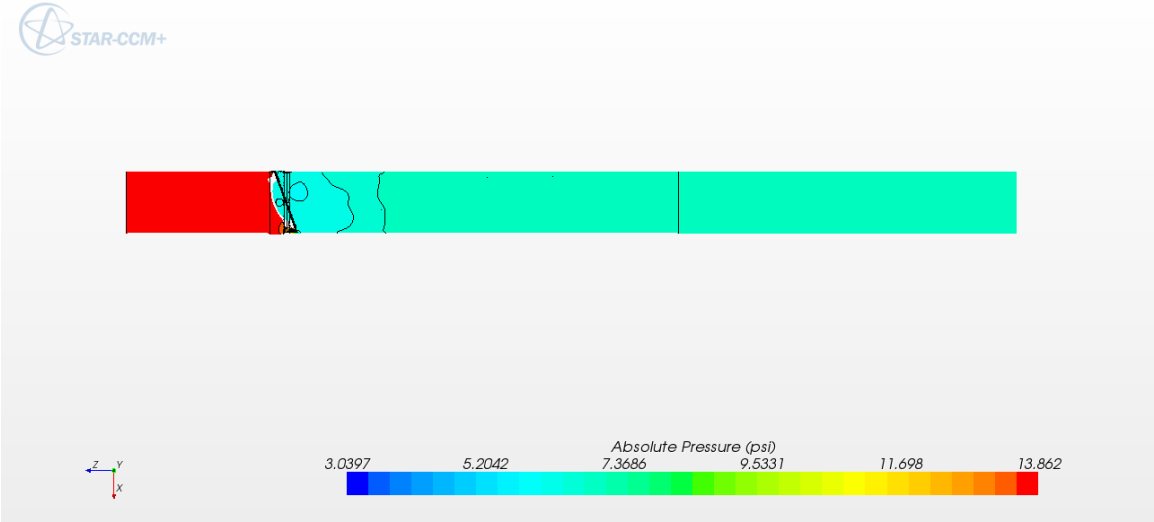

Fig. E.9: Top view of absolute pressure across the entire flow domain for the 20 degree open case.

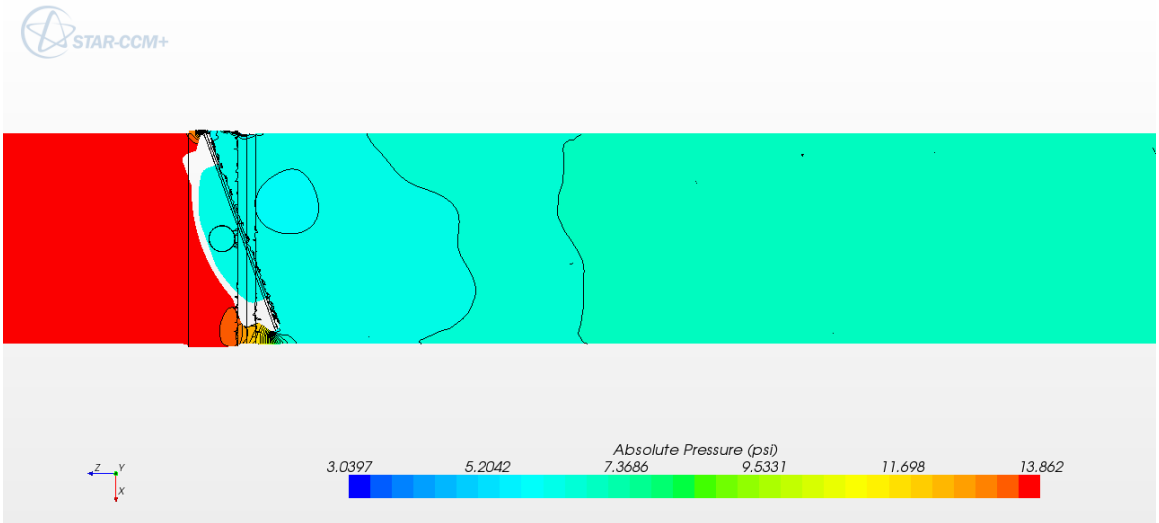

Fig. E.10: Detailed top view of absolute pressure across the butterfly valve for the 20 degree open case.

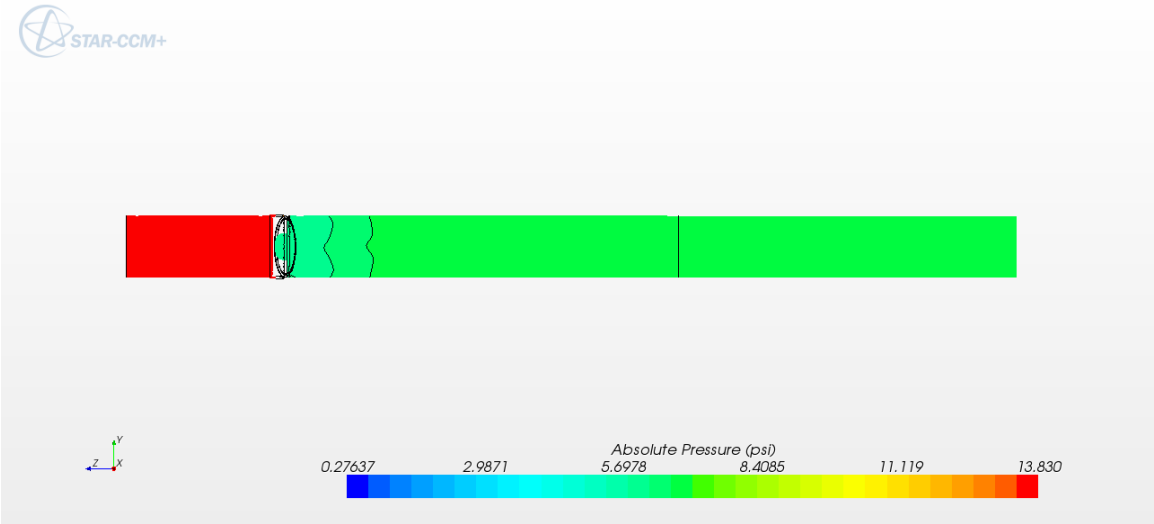

Fig. E.11: Side view of absolute pressure across the entire flow domain for the 20 degree open case.

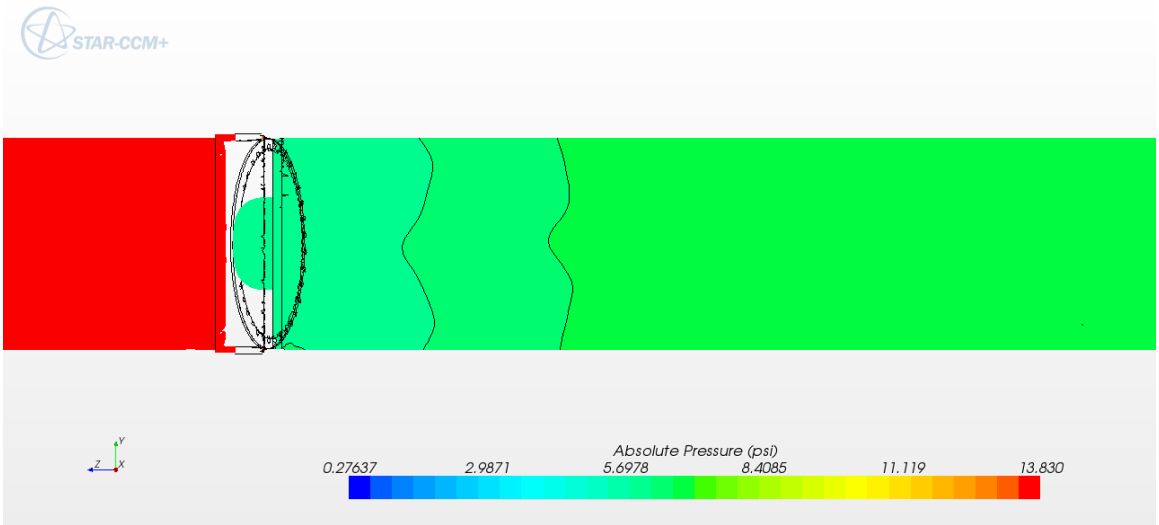

Fig. E.12: Detailed side view of absolute pressure across the butterfly valve for the 20 degree open case.

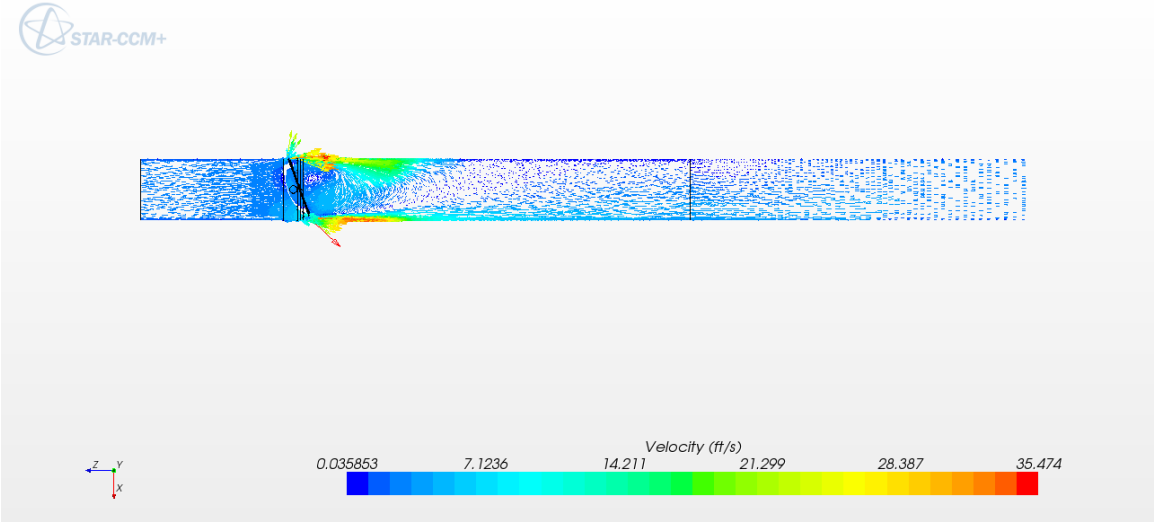

Fig. E.13: Top view of velocity vectors across the entire flow domain for the 20 degree open case.

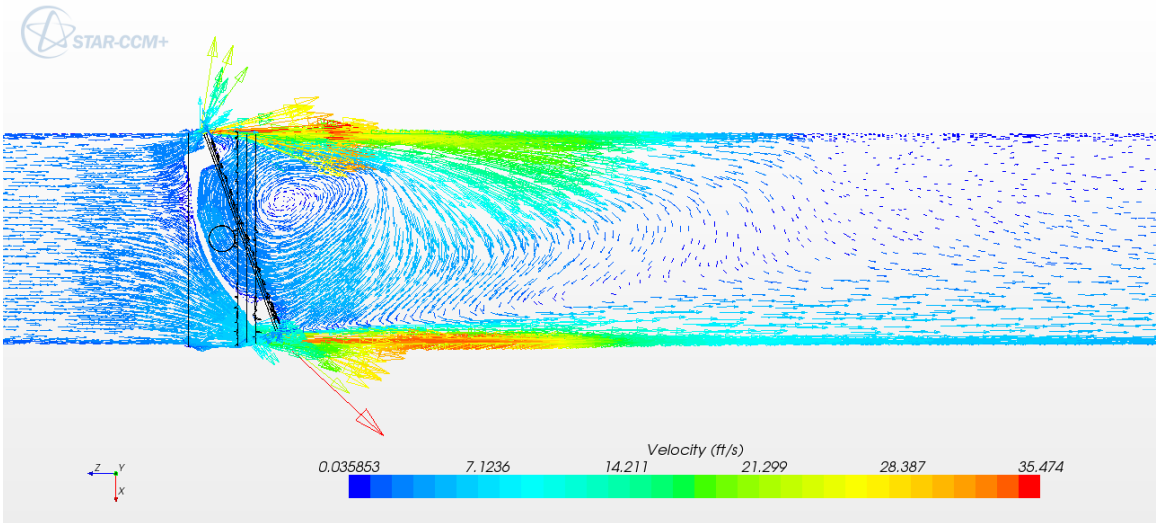

Fig. E.14: Detailed top view of velocity vectors across the butterfly valve for the 20 degree open case.

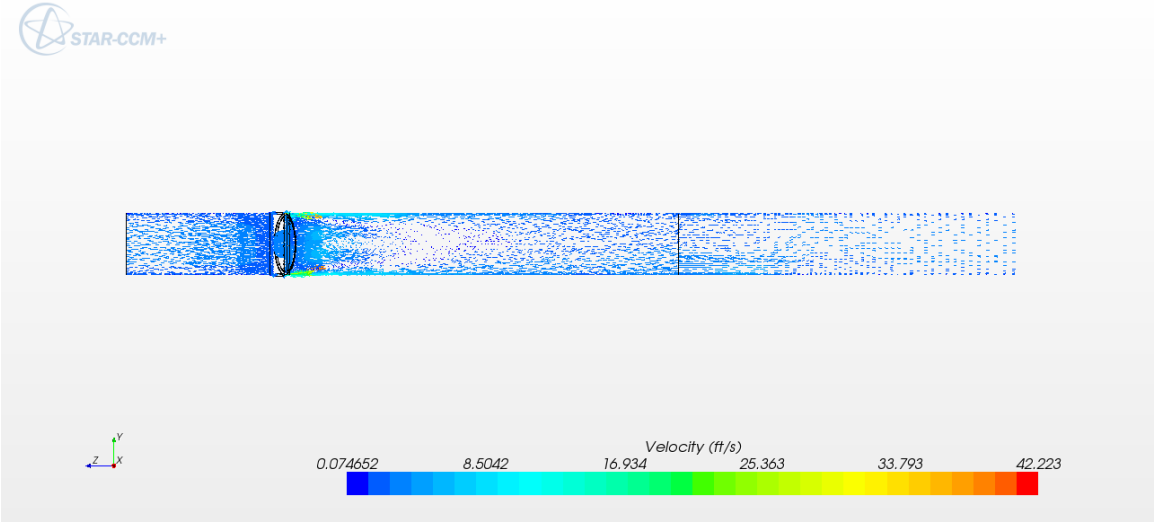

Fig. E.15: Side view of velocity vectors across the entire flow domain for the 20 degree open case.

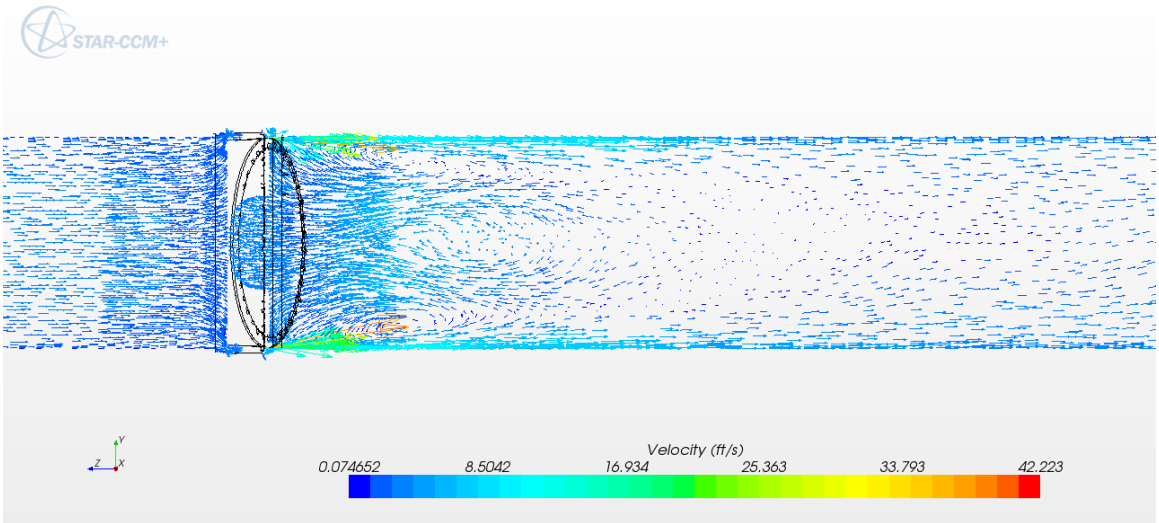

Fig. E.16: Detailed side view of velocity vectors across the butterfly valve for the 20 degree open case.

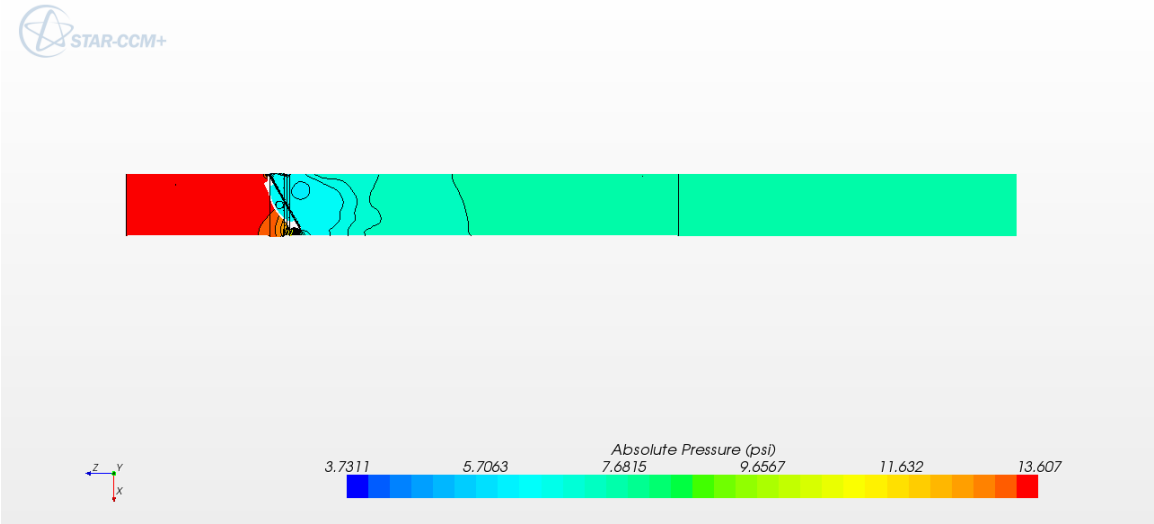

Fig. E.17: Top view of absolute pressure across the entire flow domain for the 30 degree open case.

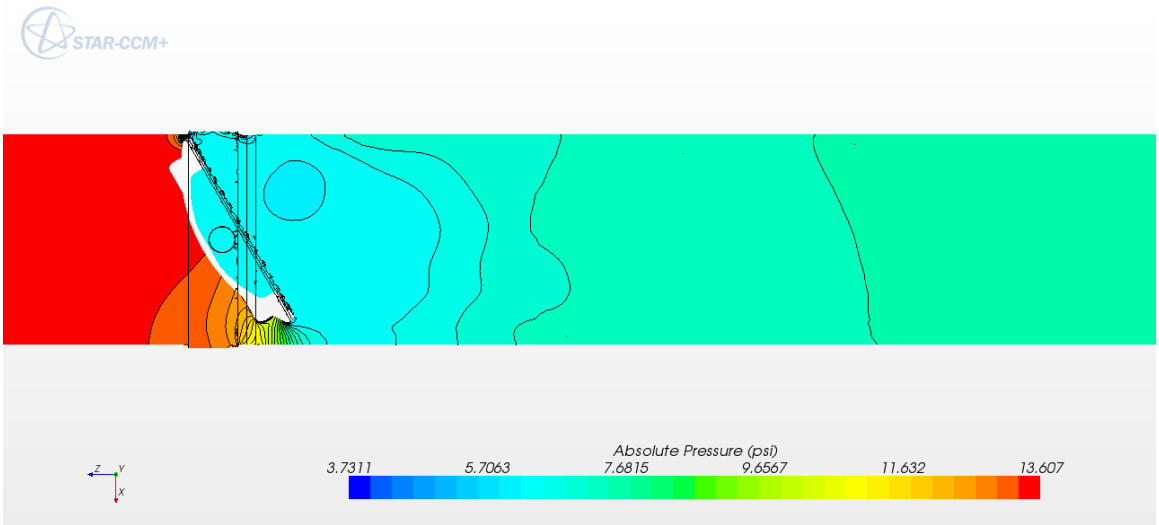

Fig. E.18: Detailed top view of absolute pressure across the butterfly valve for the 30 degree open case.

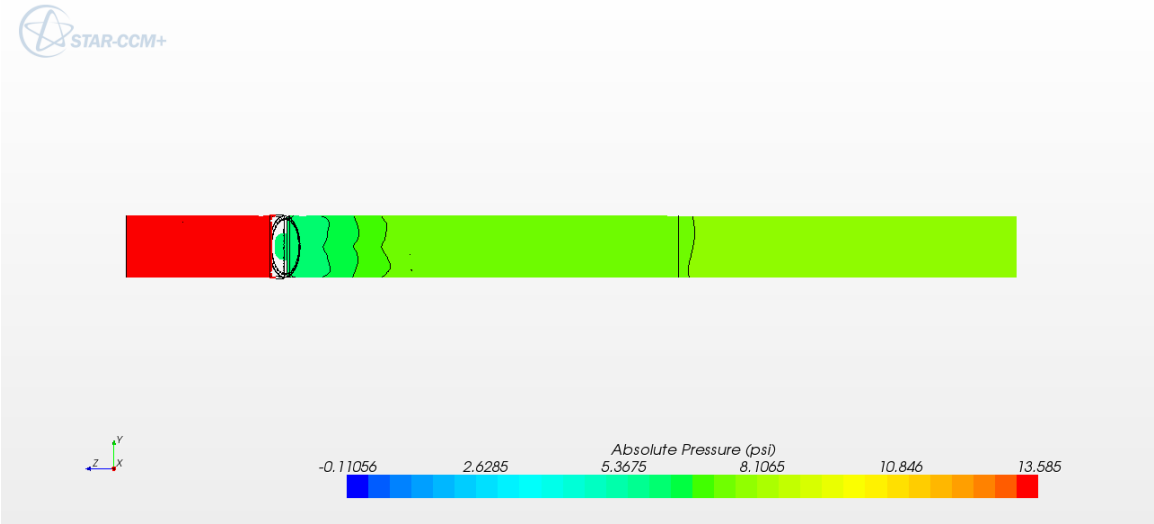

Fig. E.19: Side view of absolute pressure across the entire flow domain for the 30 degree open case.

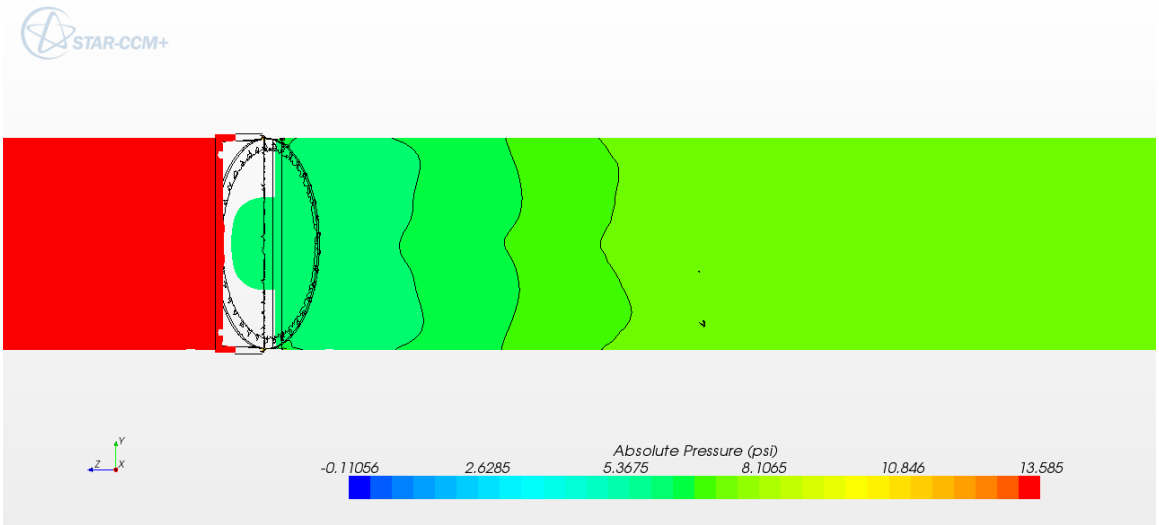

Fig. E.20: Detailed side view of absolute pressure across the butterfly valve for the 30 degree open case.

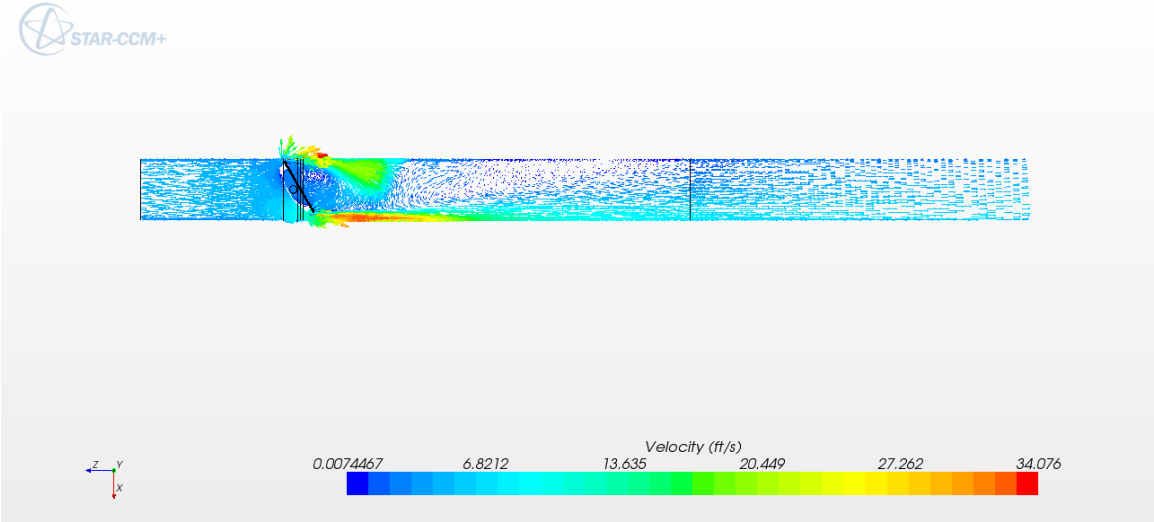

Fig. E.21: Top view of velocity vectors across the entire flow domain for the 30 degree open case.

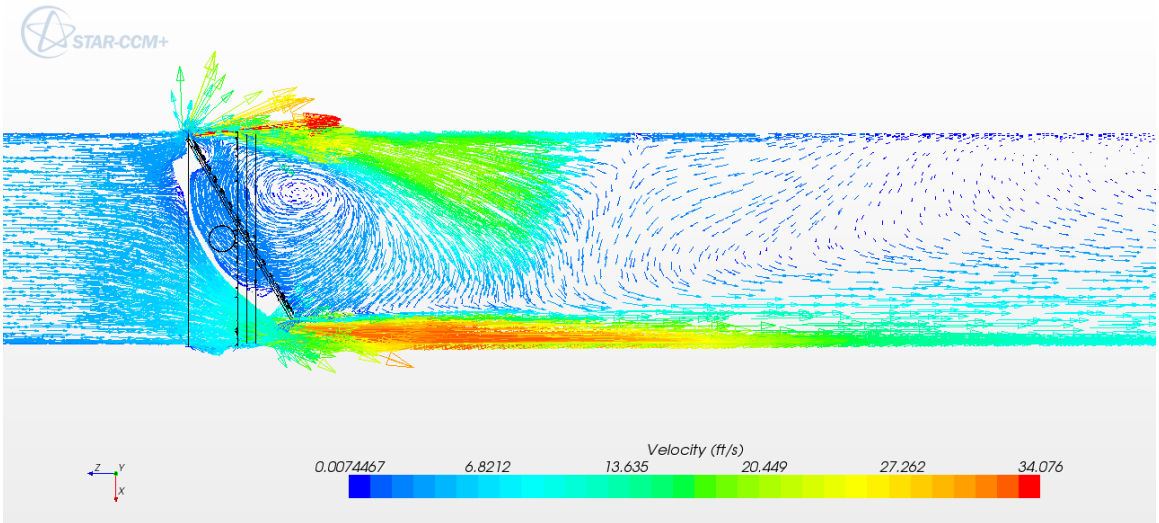

Fig. E.22: Detailed top view of velocity vectors across the butterfly valve for the 30 degree open case.

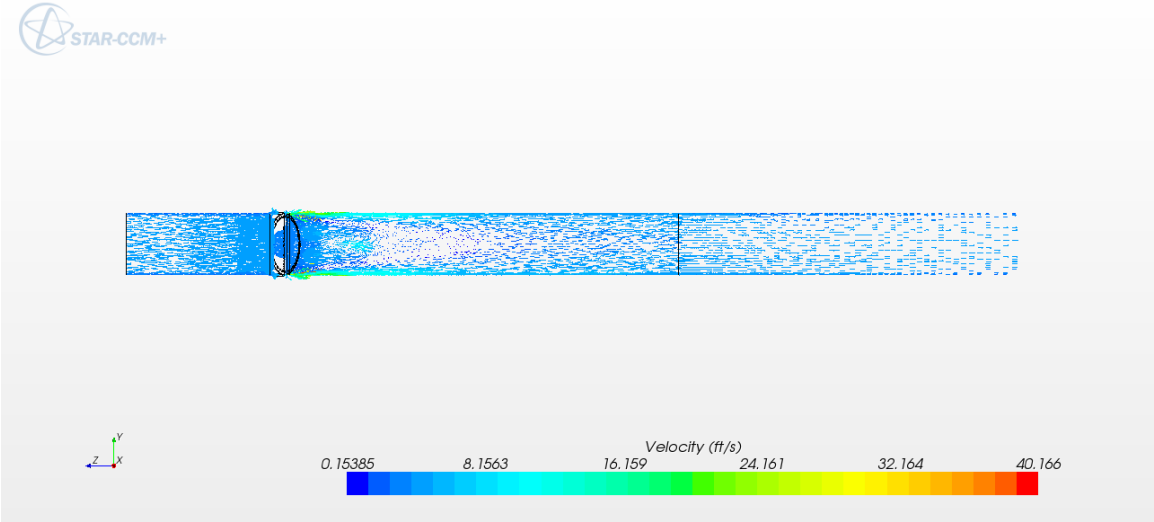

Fig. E.23: Side view of velocity vectors across the entire flow domain for the 30 degree open case.

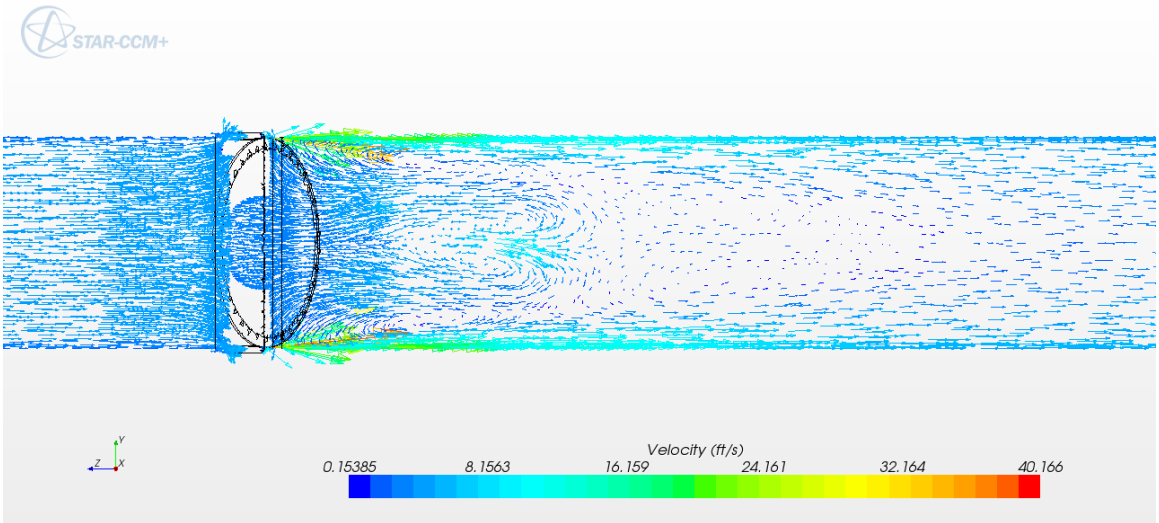

Fig. E.24: Detailed side view of velocity vectors across the butterfly valve for the 30 degree open case.

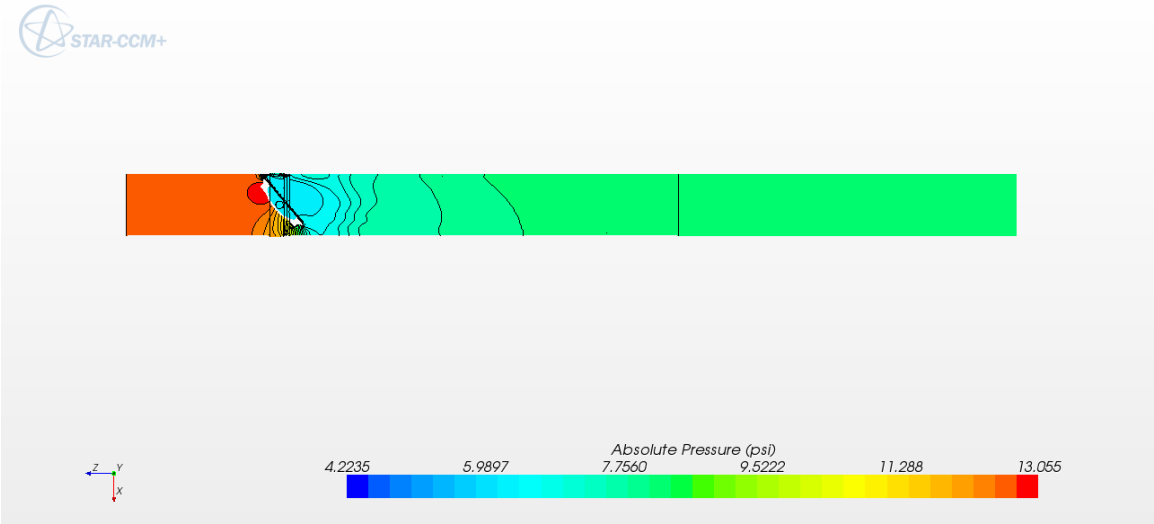

Fig. E.25: Top view of absolute pressure across the entire flow domain for the 40 degree open case.

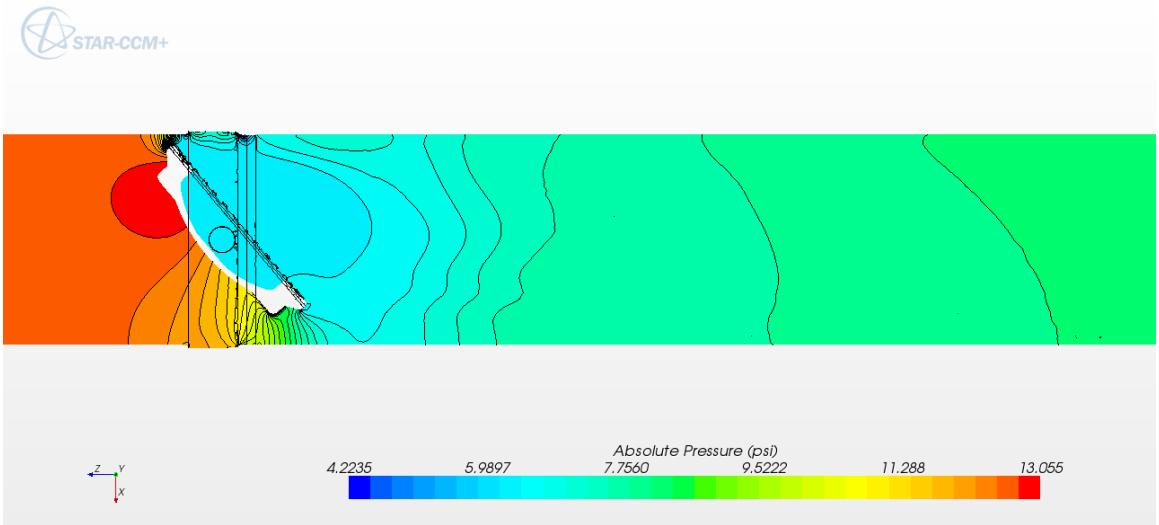

Fig. E.26: Detailed top view of absolute pressure across the butterfly valve for the 40 degree open case.

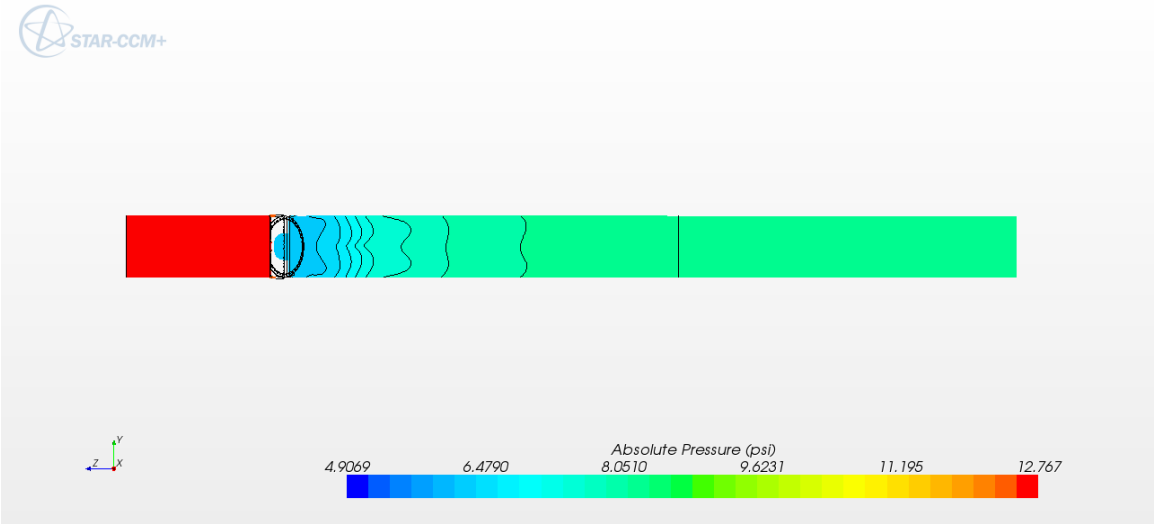

Fig. E.27: Side view of absolute pressure across the entire flow domain for the 40 degree open case.

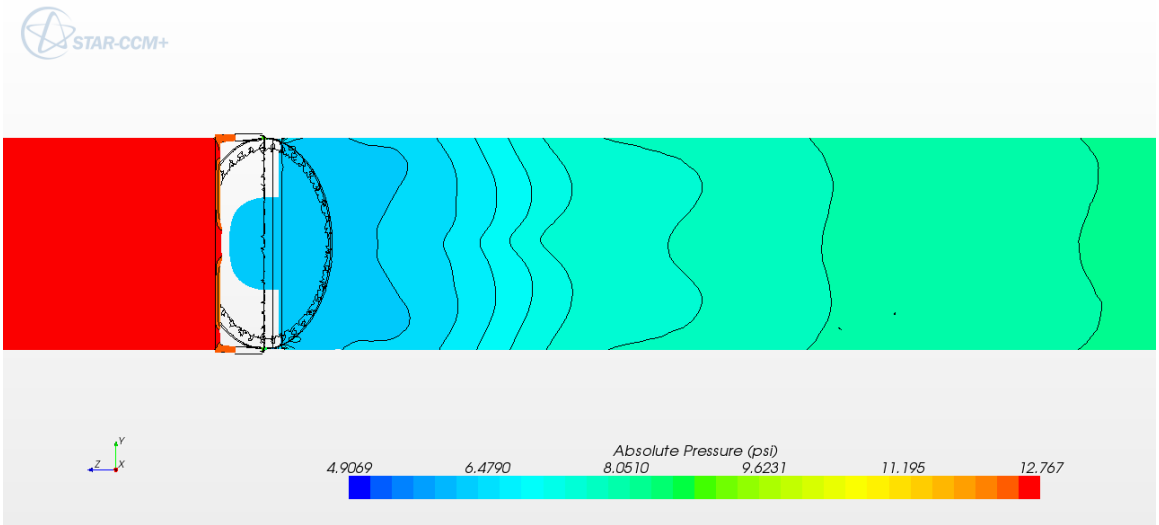

Fig. E.28: Detailed side view of absolute pressure across the butterfly valve for the 40 degree open case.

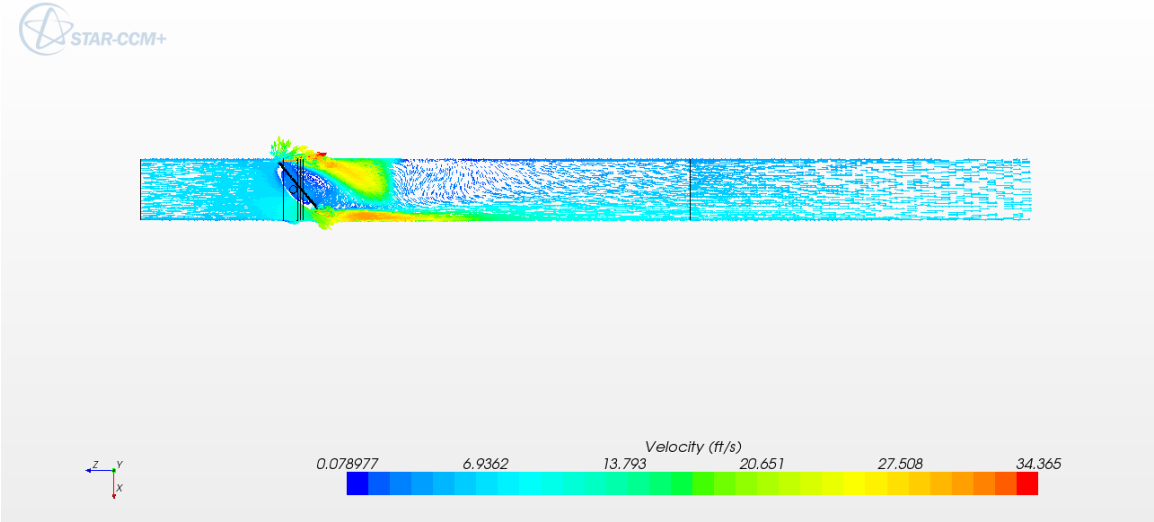

Fig. E.29: Top view of velocity vectors across the entire flow domain for the 40 degree open case.

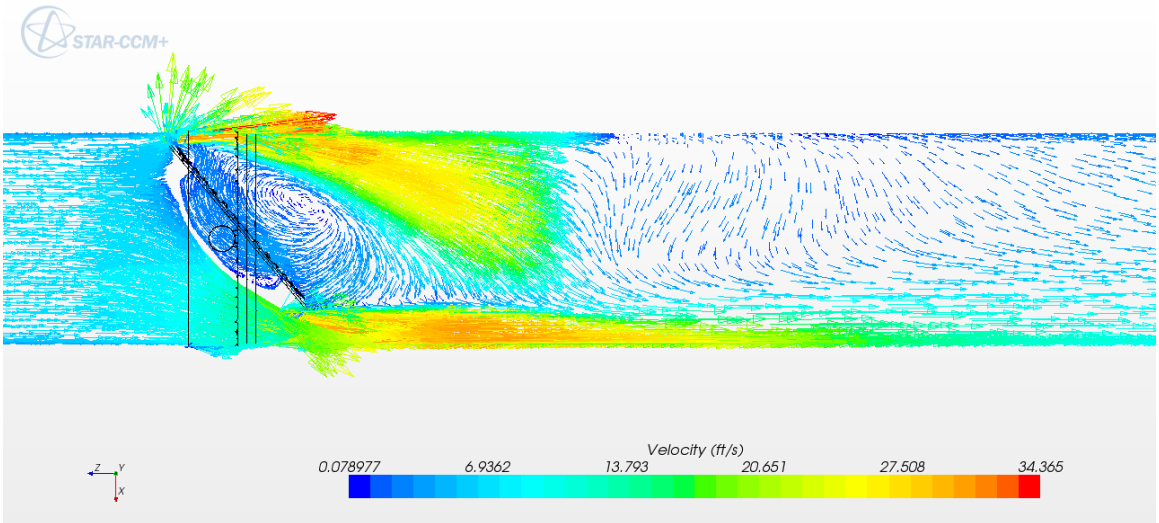

Fig. E.30: Detailed top view of velocity vectors across the butterfly valve for the 40 degree open case.

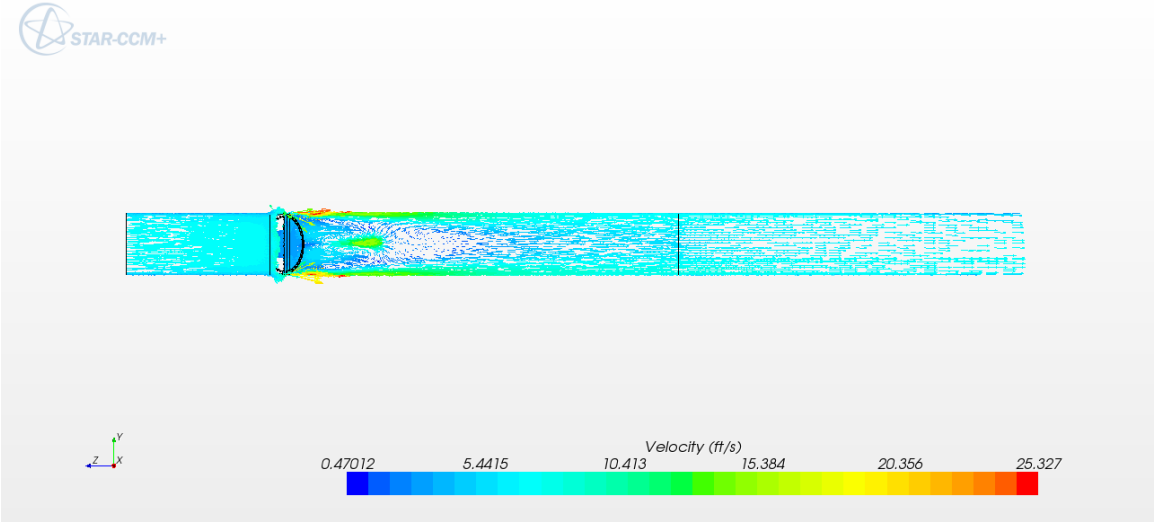

Fig. E.31: Side view of velocity vectors across the entire flow domain for the 40 degree open case.

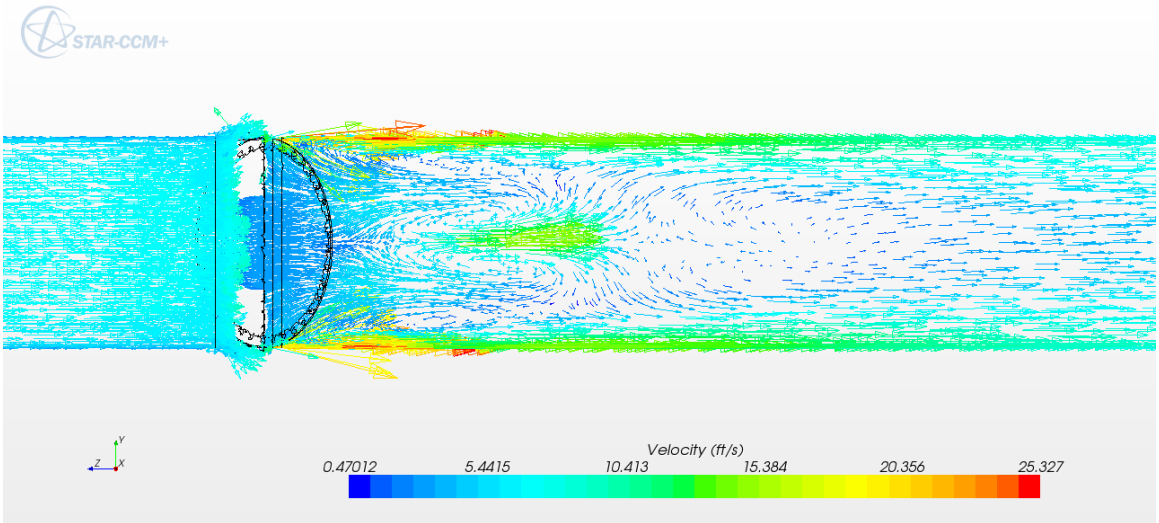

Fig. E.32: Detailed side view of velocity vectors across the butterfly valve for the 40 degree open case.

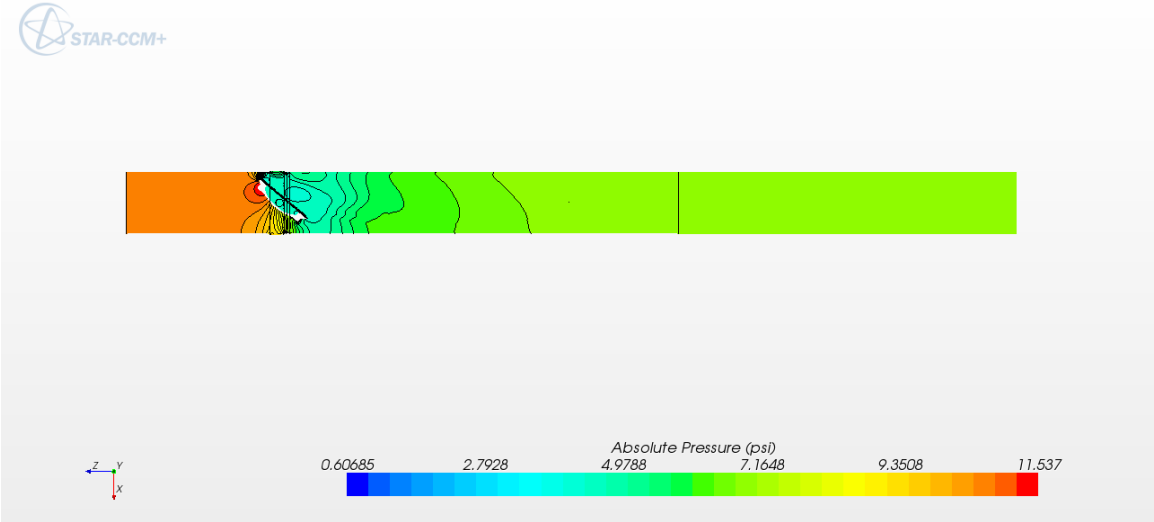

Fig. E.33: Top view of absolute pressure across the entire flow domain for the 50 degree open case.

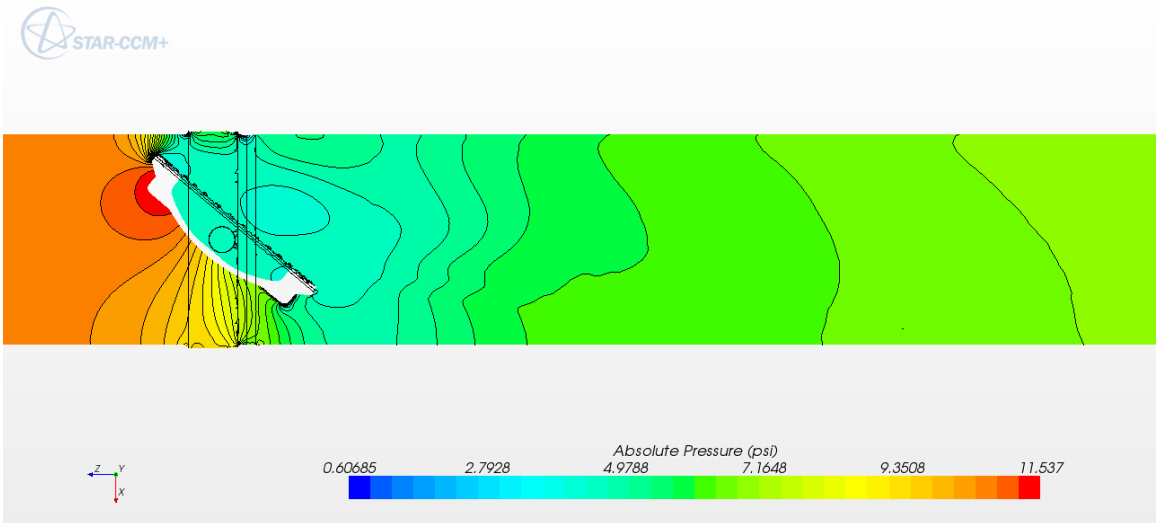

Fig. E.34: Detailed top view of absolute pressure across the butterfly valve for the 50 degree open case.

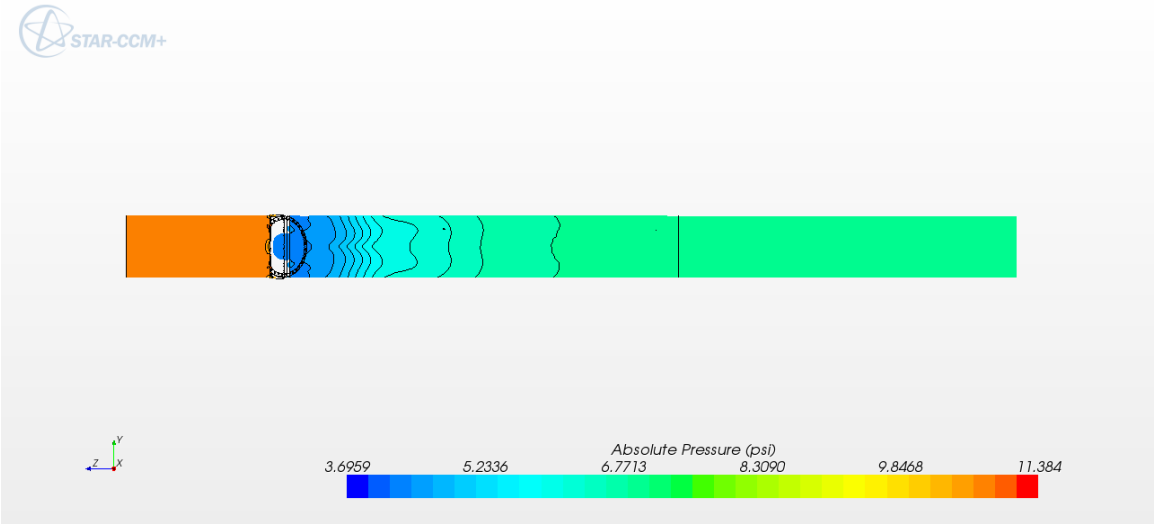

Fig. E.35: Side view of absolute pressure across the entire flow domain for the 50 degree open case.

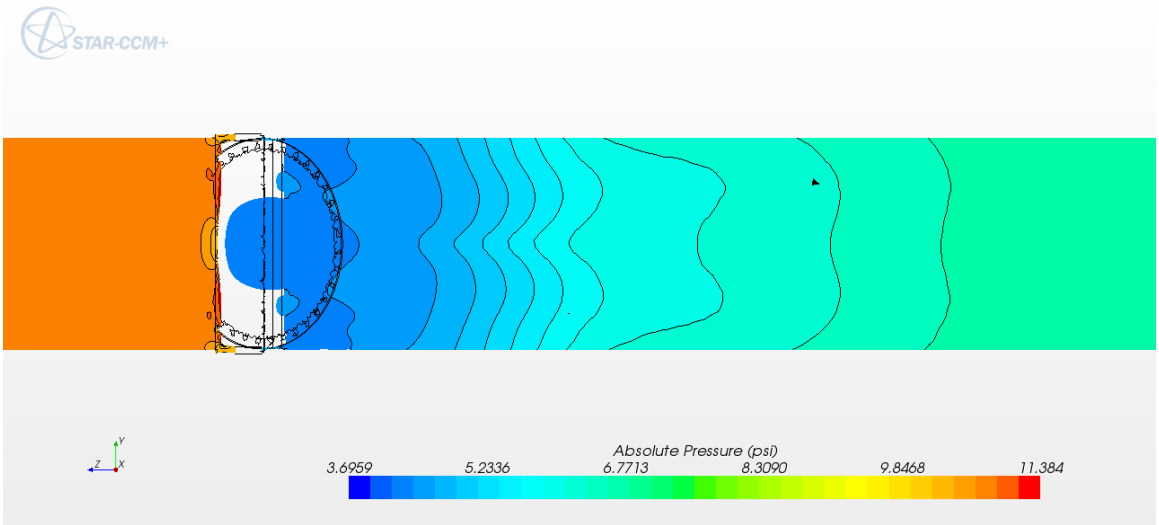

Fig. E.36: Detailed side view of absolute pressure across the butterfly valve for the 50 degree open case.

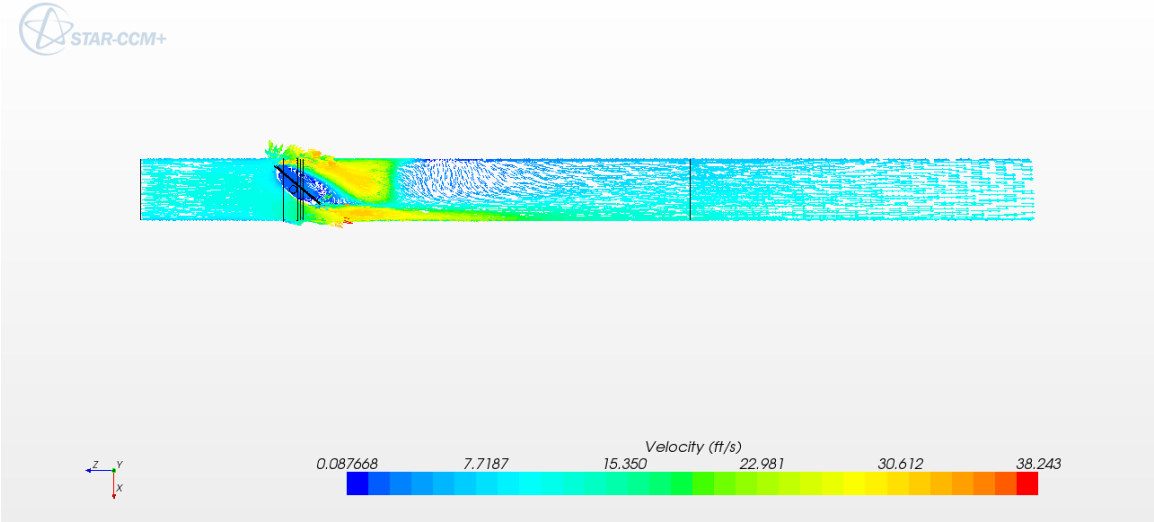

Fig. E.37: Top view of velocity vectors across the entire flow domain for the 50 degree open case.

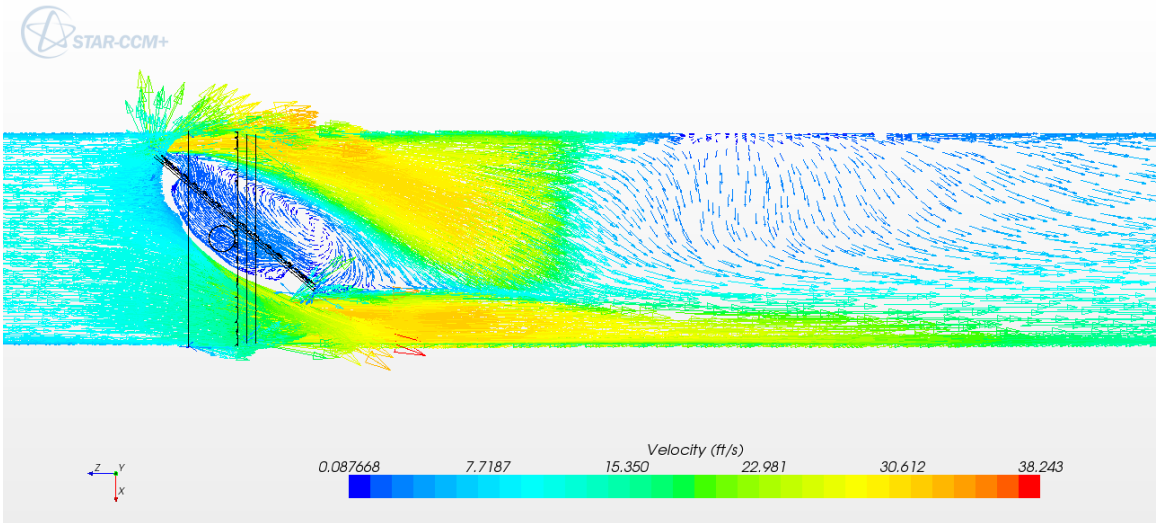

Fig. E.38: Detailed top view of velocity vectors across the butterfly valve for the 50 degree open case.

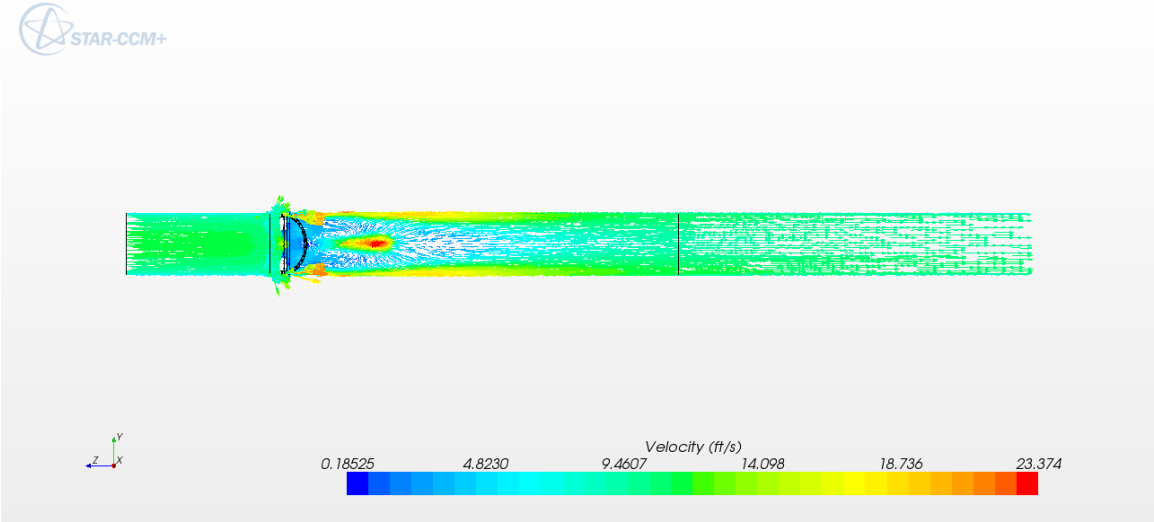

Fig. E.39: Side view of velocity vectors across the entire flow domain for the 50 degree open case.

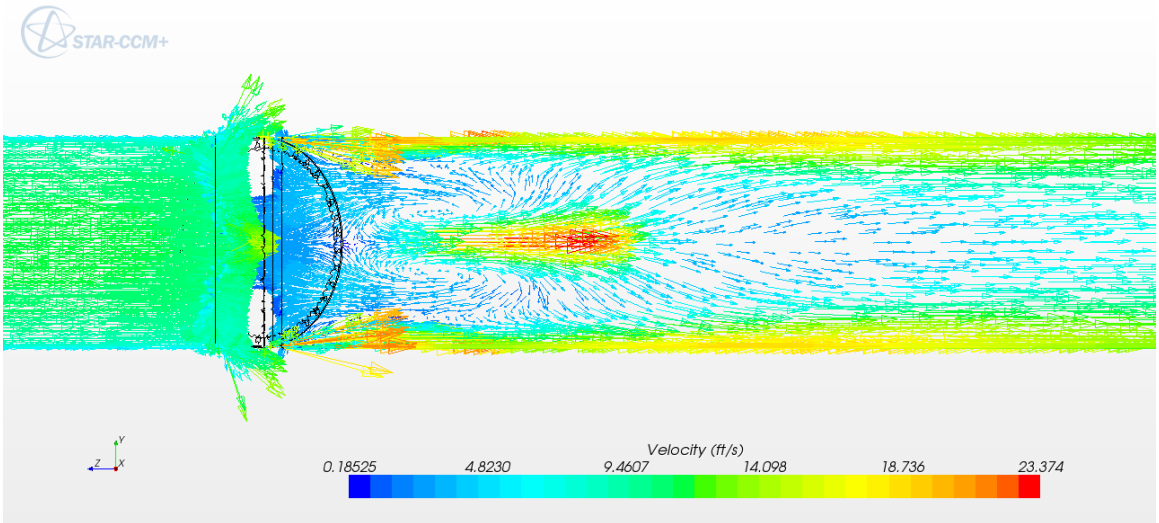

Fig. E.40: Detailed side view of velocity vectors across the butterfly valve for the 50 degree open case.

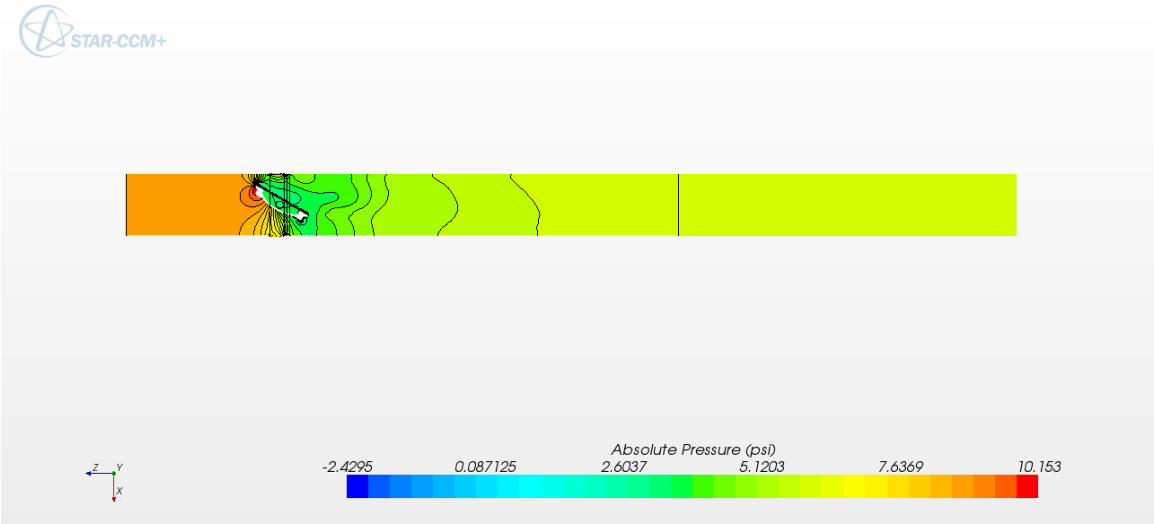

Fig. E.41: Top view of absolute pressure across the entire flow domain for the 60 degree open case.

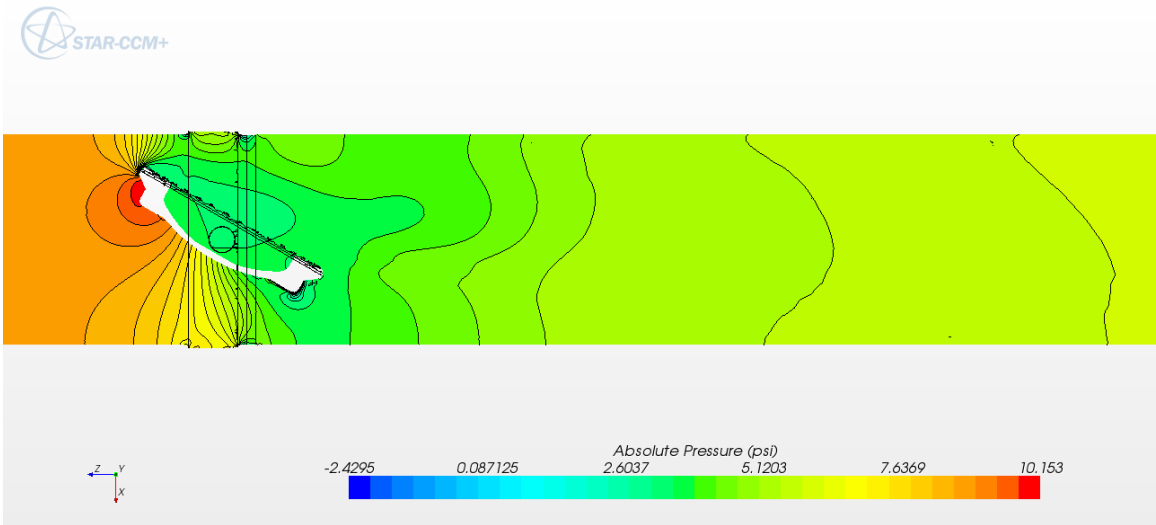

Fig. E.42: Detailed top view of absolute pressure across the butterfly valve for the 60 degree open case.

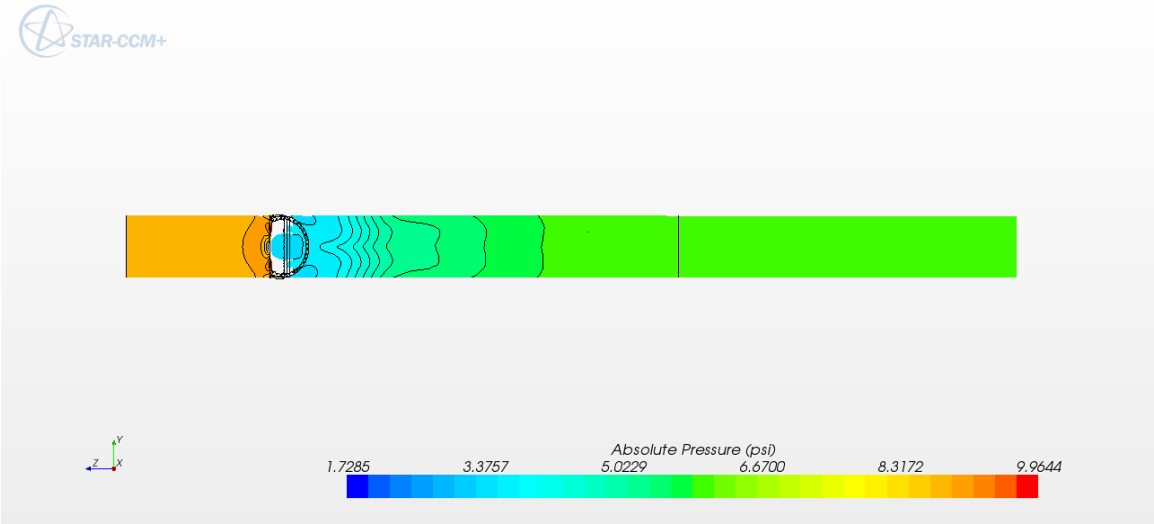

Fig. E.43: Side view of absolute pressure across the entire flow domain for the 60 degree open case.

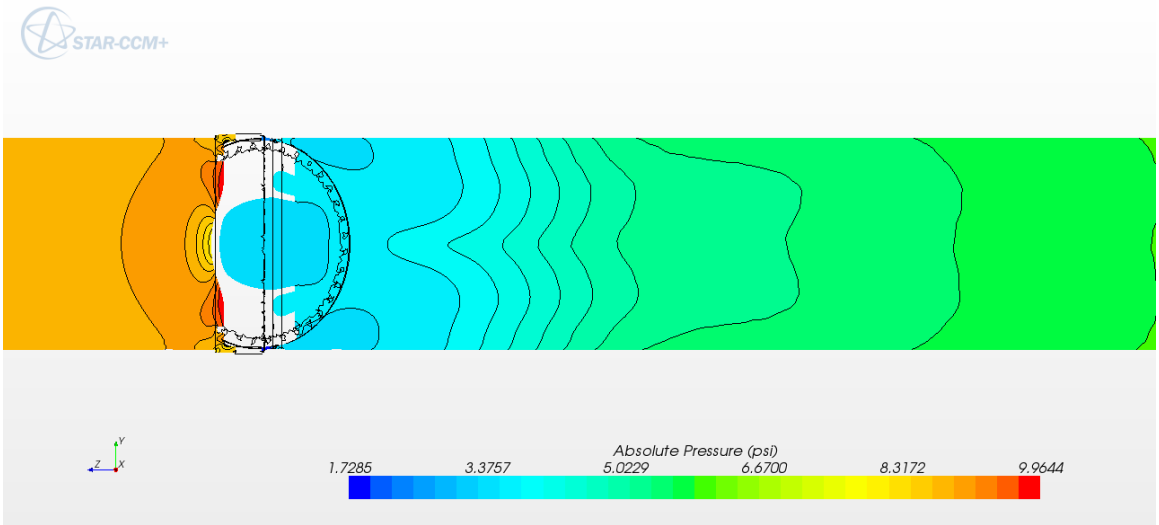

Fig. E.44: Detailed side view of absolute pressure across the butterfly valve for the 60 degree open case.

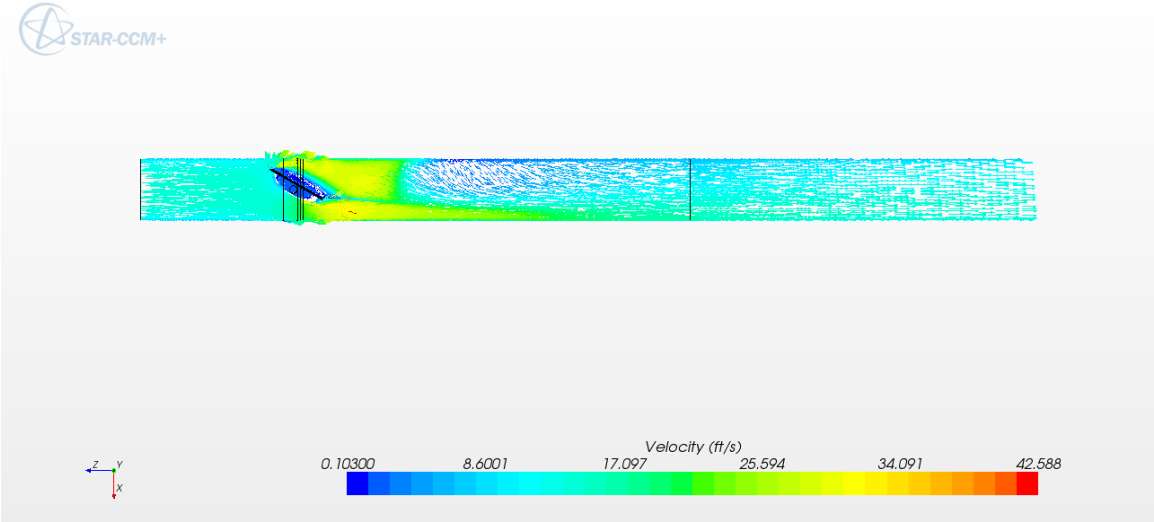

Fig. E.45: Top view of velocity vectors across the entire flow domain for the 60 degree open case.

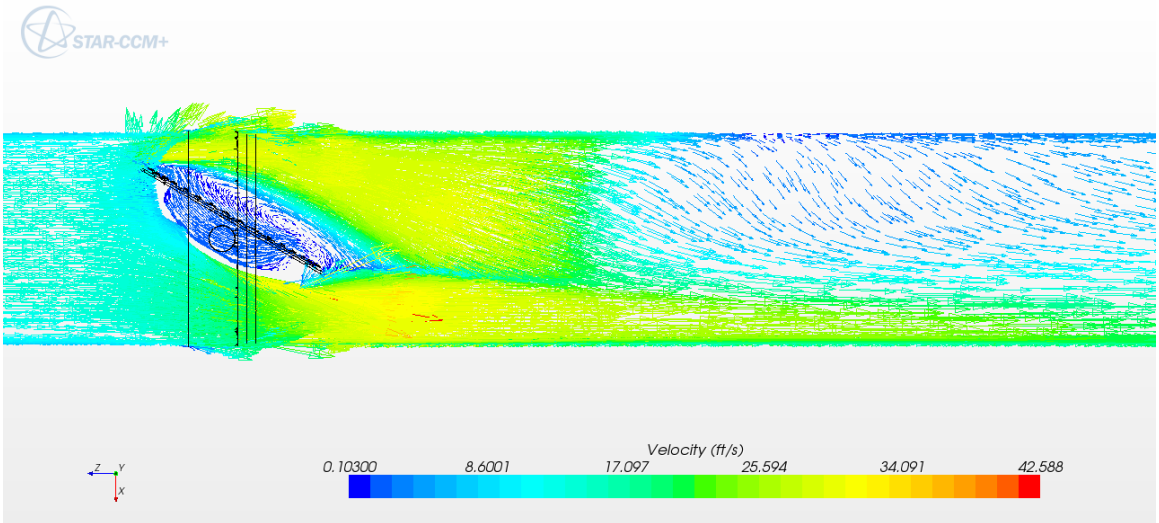

Fig. E.46: Detailed top view of velocity vectors across the butterfly valve for the 60 degree open case.

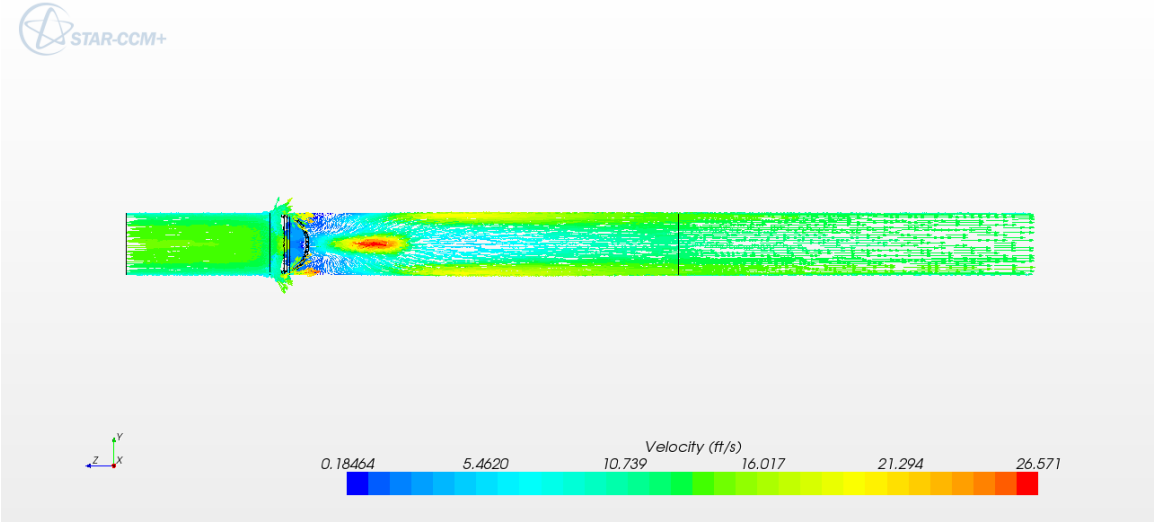

Fig. E.47: Side view of velocity vectors across the entire flow domain for the 60 degree open case.

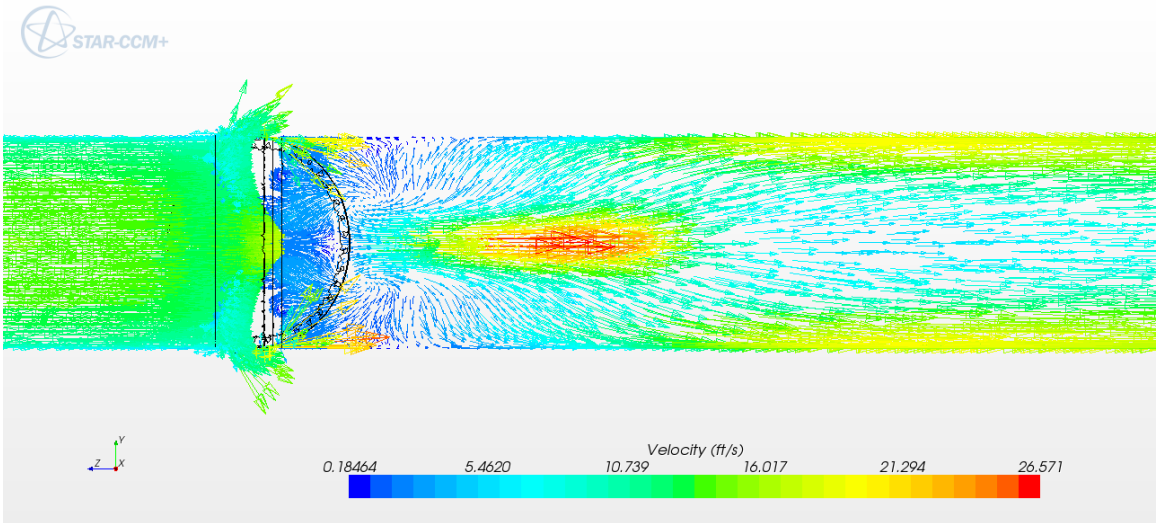

Fig. E.48: Detailed side view of velocity vectors across the butterfly valve for the 60 degree open case.

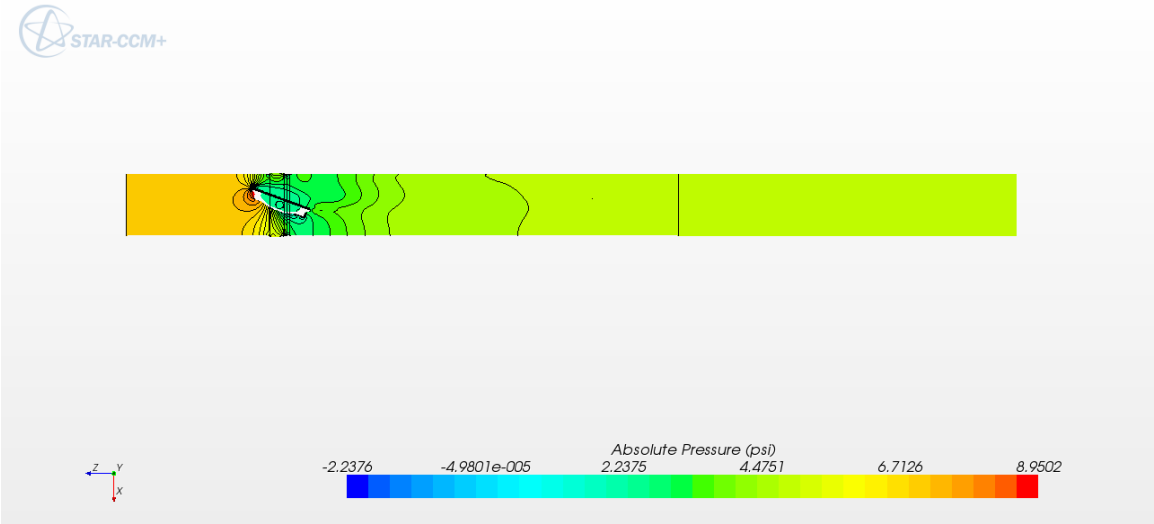

Fig. E.49: Top view of absolute pressure across the entire flow domain for the 70 degree open case.

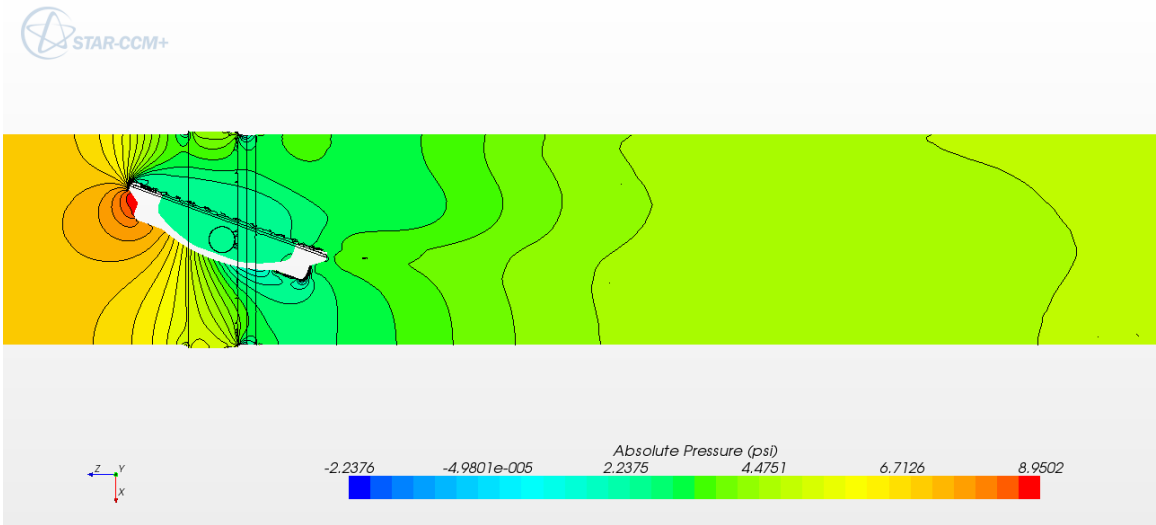

Fig. E.50: Detailed top view of absolute pressure across the butterfly valve for the 70 degree open case.

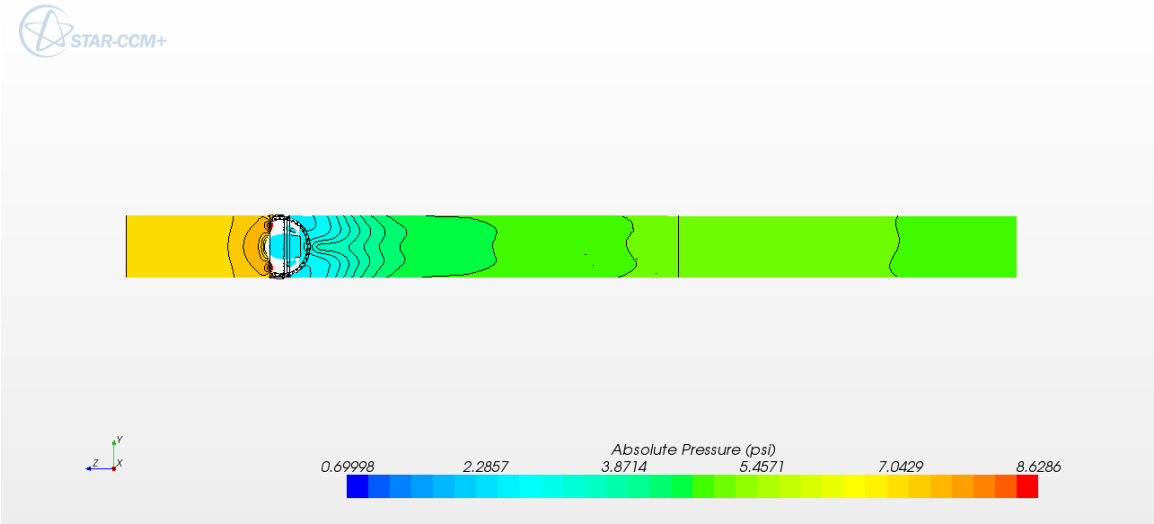

Fig. E.51: Side view of absolute pressure across the entire flow domain for the 70 degree open case.

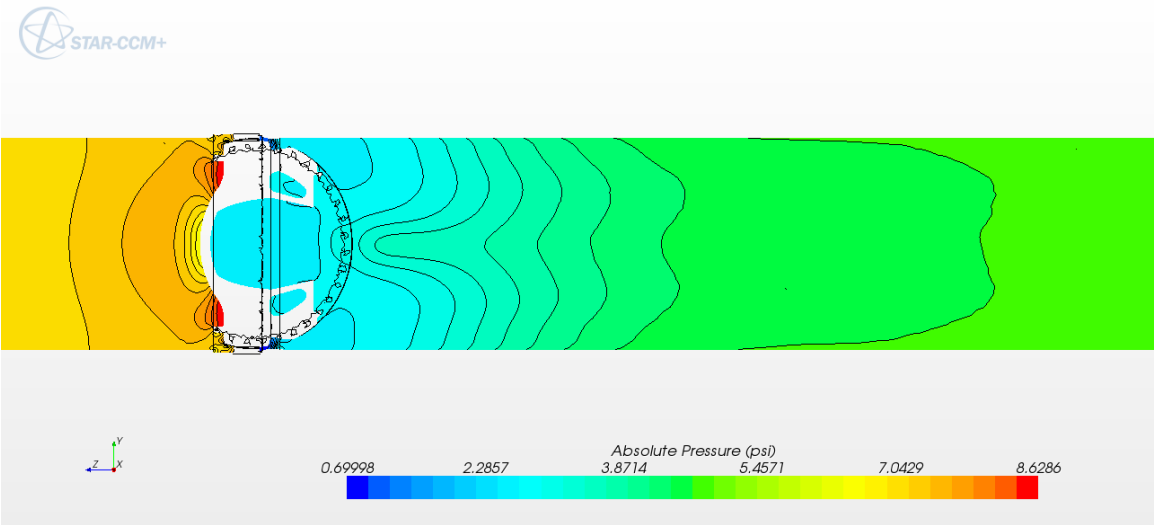

Fig. E.52: Detailed side view of absolute pressure across the butterfly valve for the 70 degree open case.

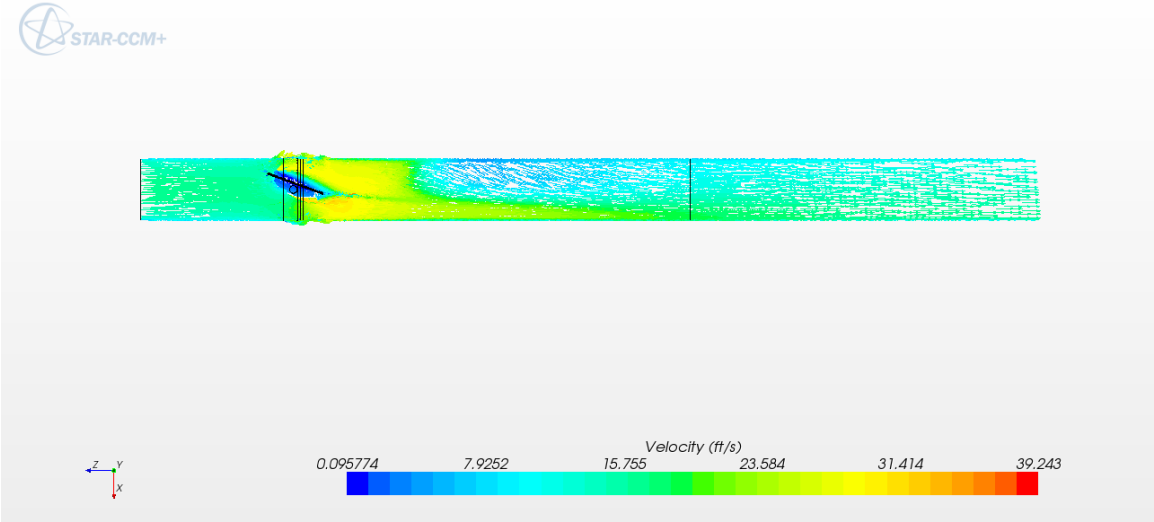

Fig. E.53: Top view of velocity vectors across the entire flow domain for the 70 degree open case.

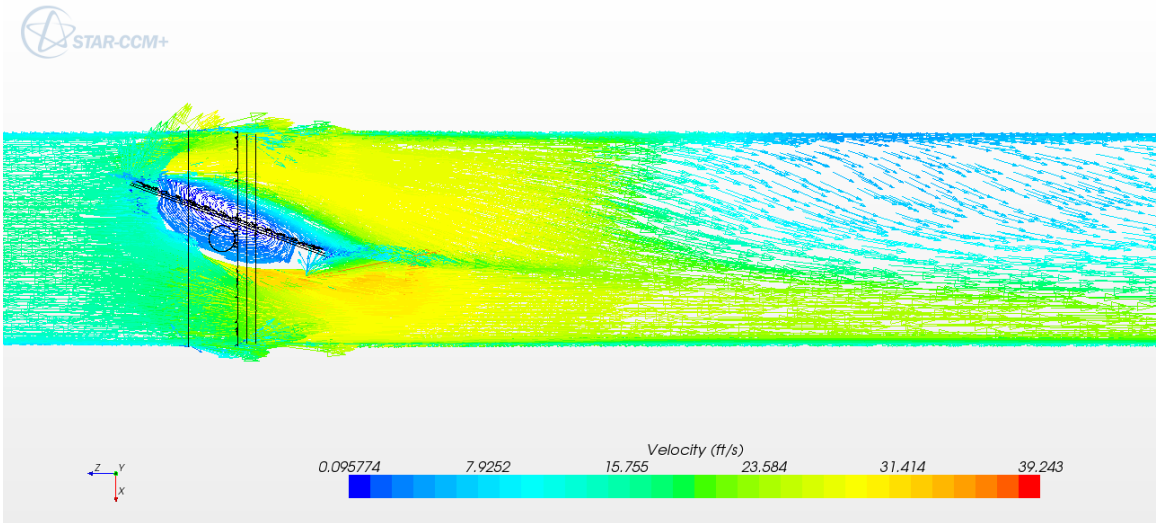

Fig. E.54: Detailed top view of velocity vectors across the butterfly valve for the 70 degree open case.

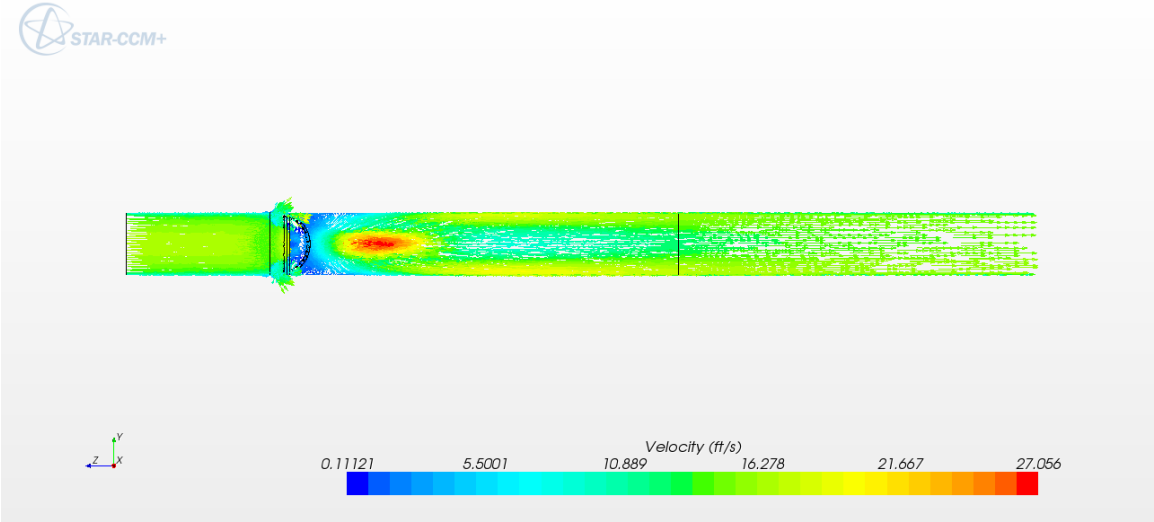

Fig. E.55: Side view of velocity vectors across the entire flow domain for the 70 degree open case.

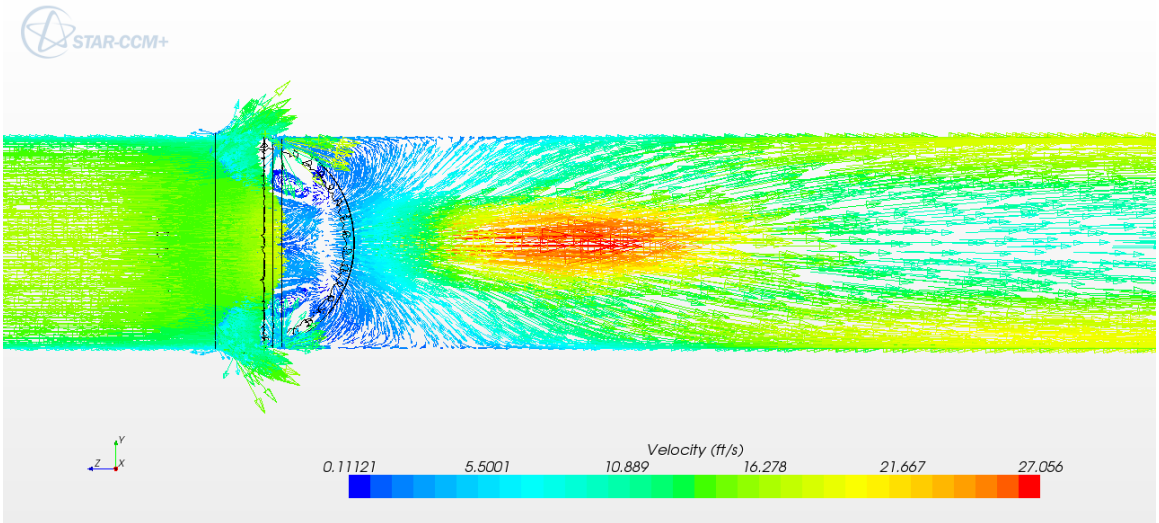

Fig. E.56: Detailed side view of velocity vectors across the butterfly valve for the 70 degree open case.

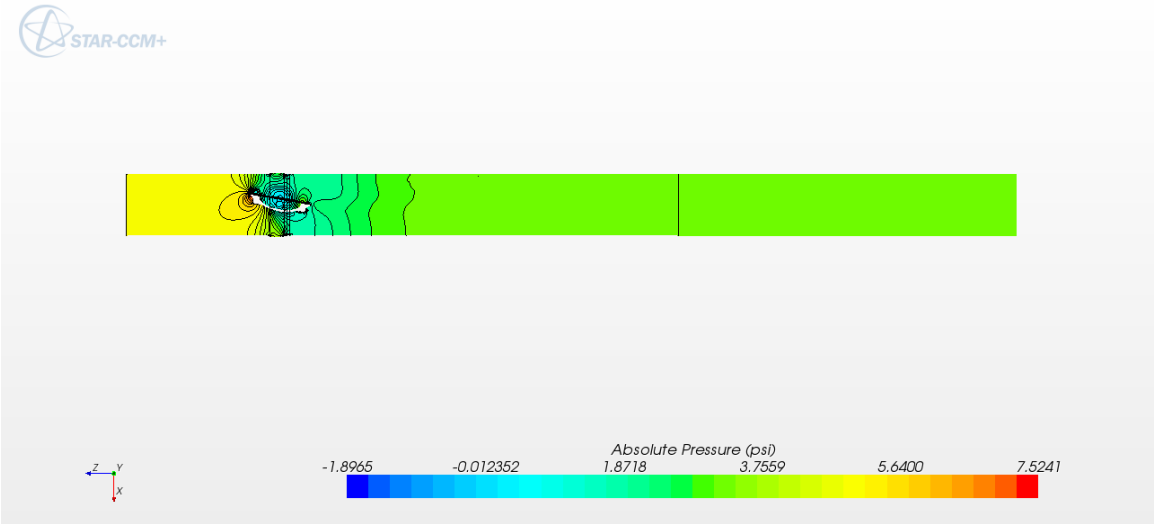

Fig. E.57: Top view of absolute pressure across the entire flow domain for the 80 degree open case.

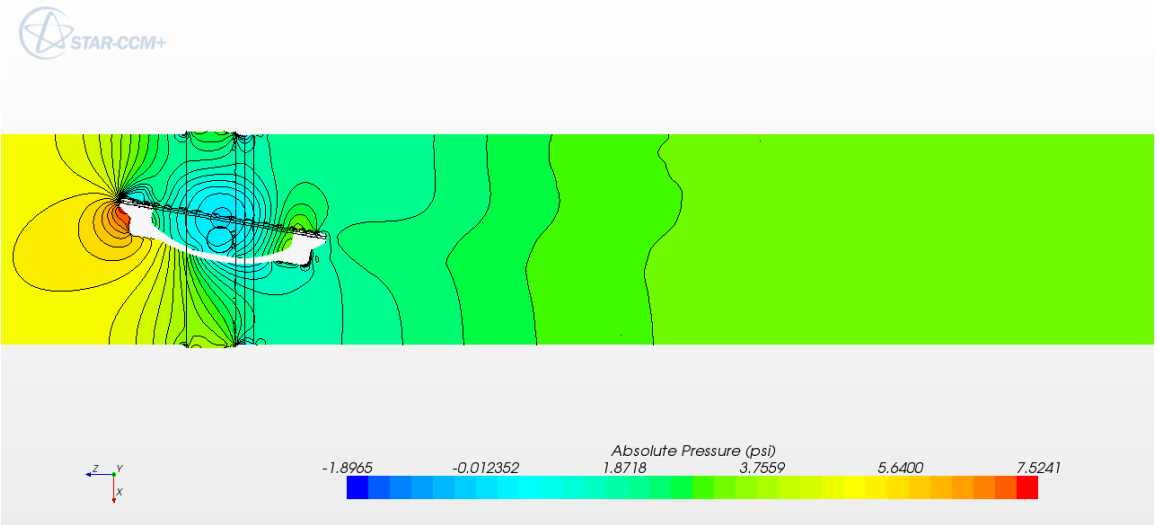

Fig. E.58: Detailed top view of absolute pressure across the butterfly valve for the 80 degree open case.

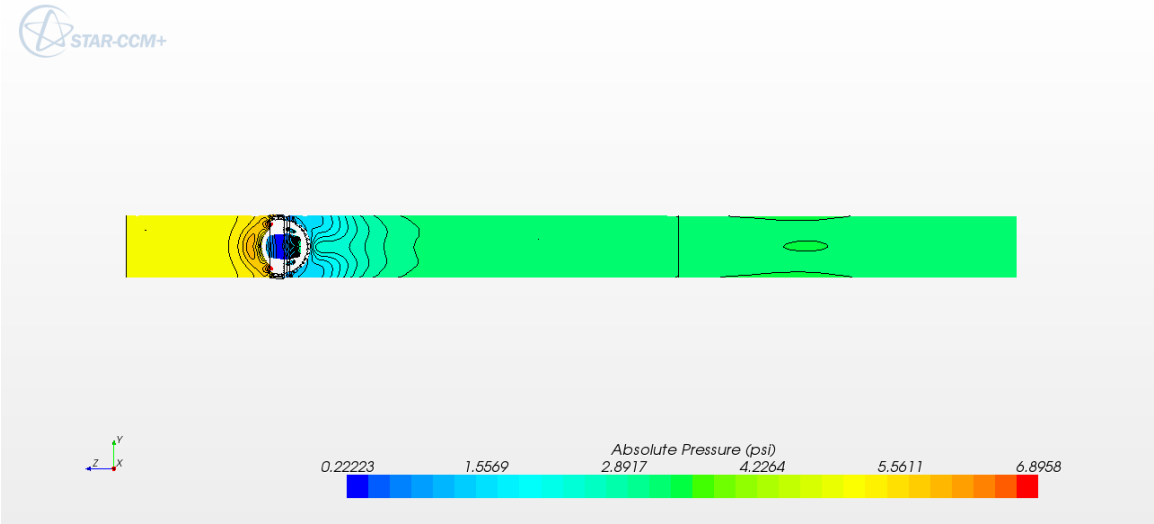

Fig. E.59: Side view of absolute pressure across the entire flow domain for the 80 degree open case.

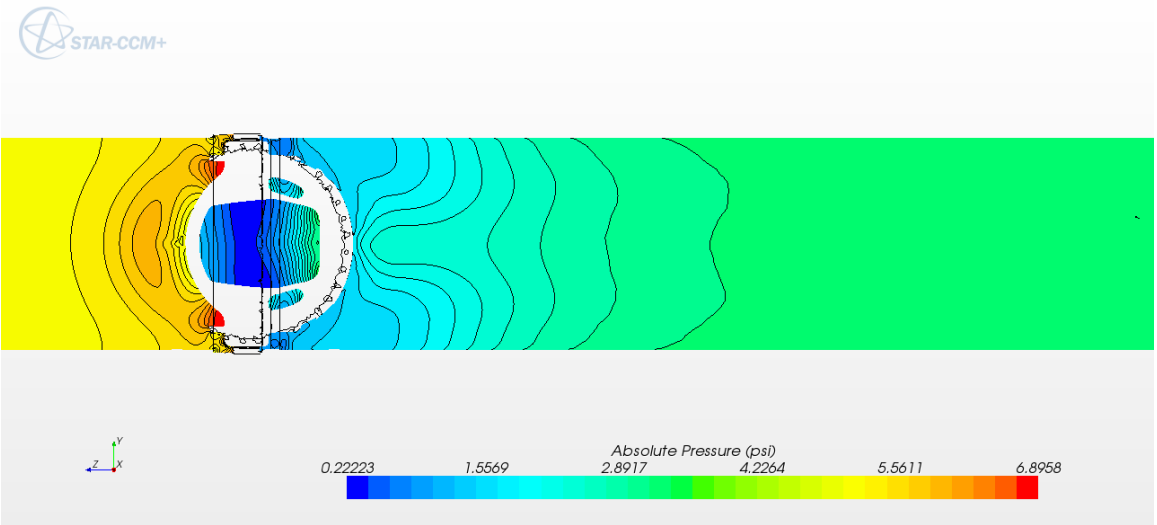

Fig. E.60: Detailed side view of absolute pressure across the butterfly valve for the 80 degree open case.

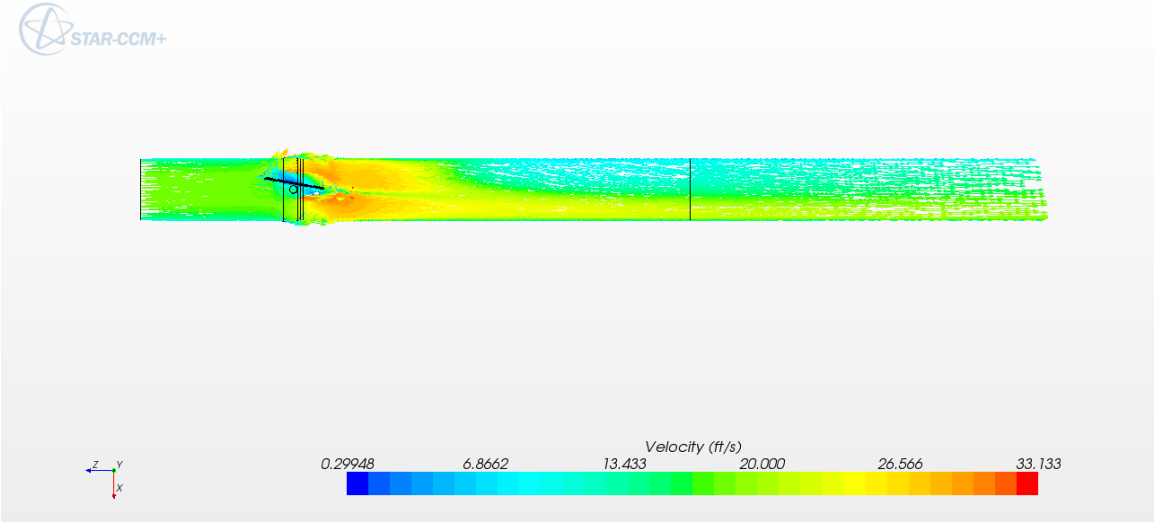

Fig. E.61: Top view of velocity vectors across the entire flow domain for the 80 degree open case.

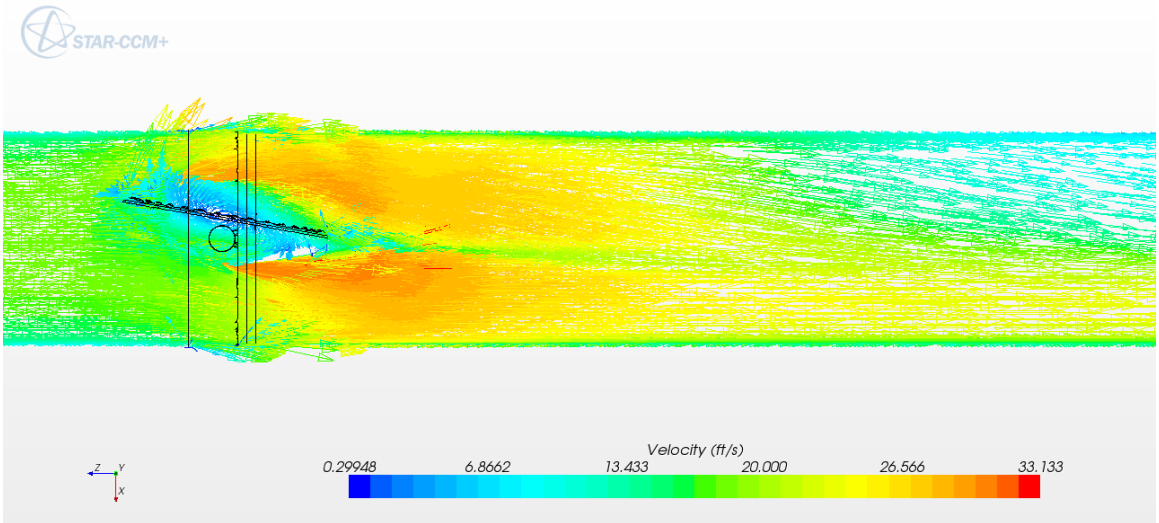

Fig. E.62: Detailed top view of velocity vectors across the butterfly valve for the 80 degree open case.

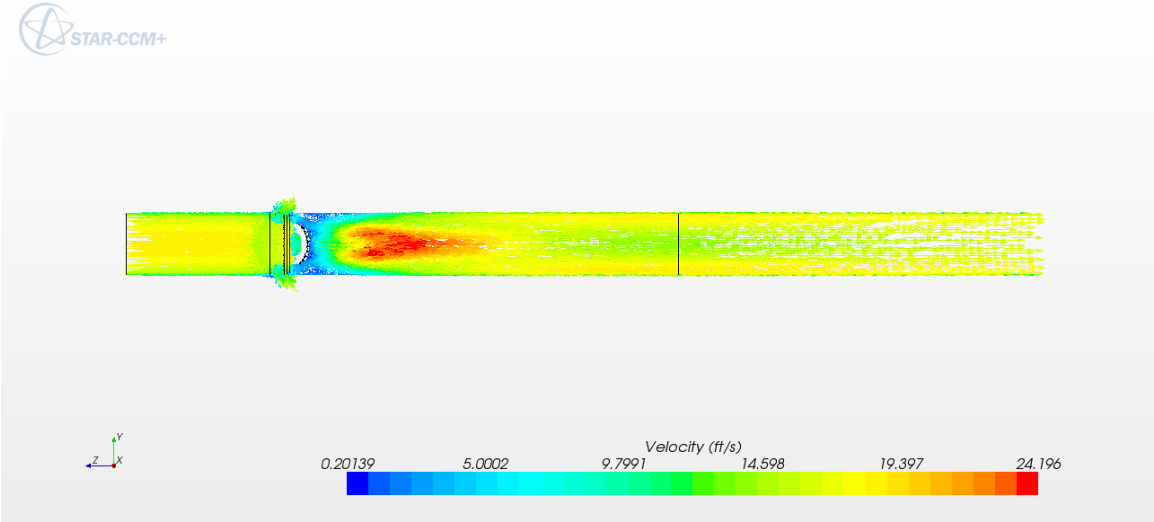

Fig. E.63: Side view of velocity vectors across the entire flow domain for the 80 degree open case.

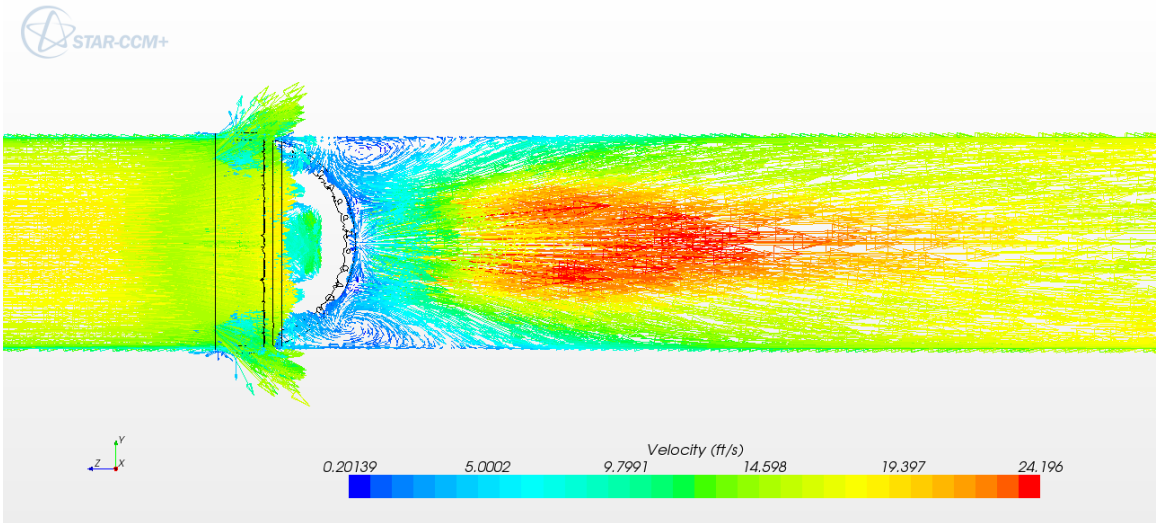

Fig. E.64: Detailed side view of velocity vectors across the butterfly valve for the 80 degree open case.

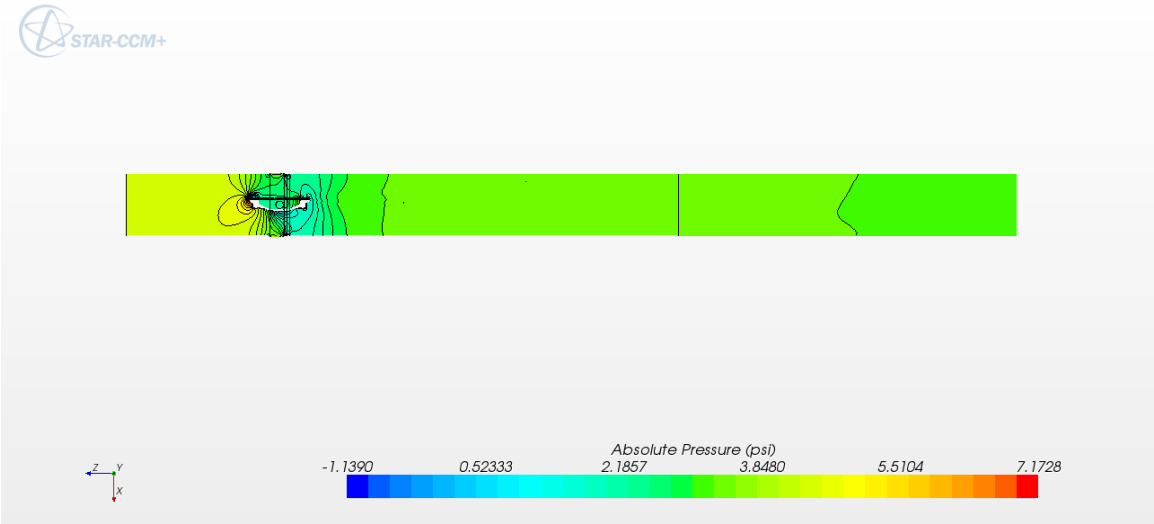

Fig. E.65: Top view of absolute pressure across the entire flow domain for the 90 degree open case.

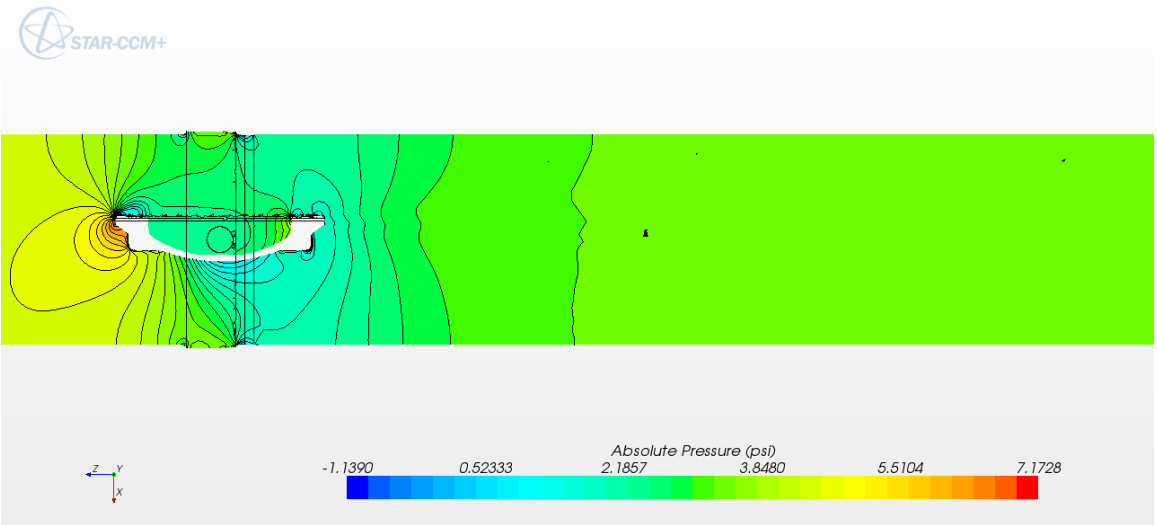

Fig. E.66: Detailed top view of absolute pressure across the butterfly valve for the 90 degree open case.

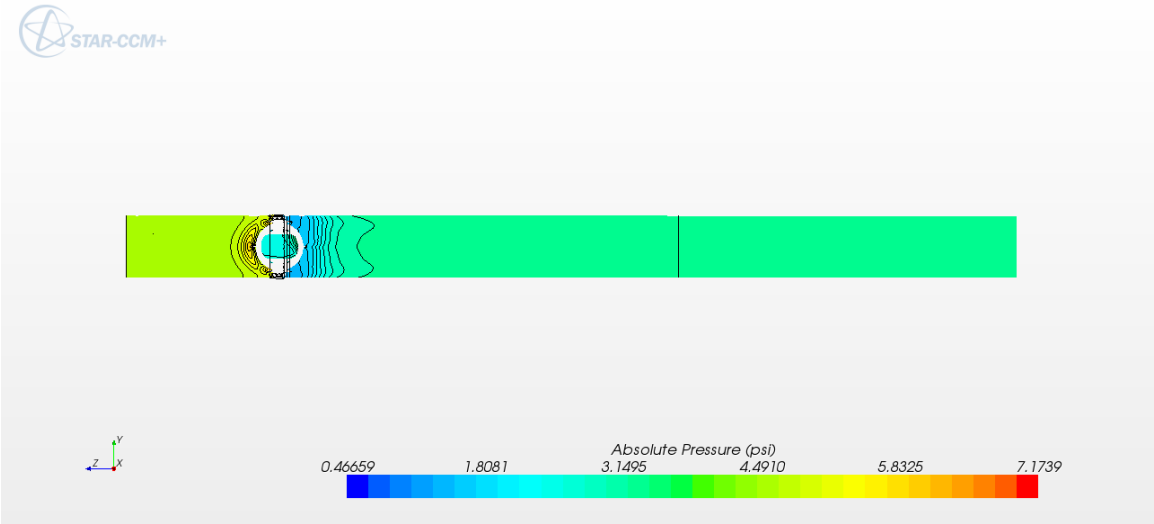

Fig. E.67: Side view of absolute pressure across the entire flow domain for the 90 degree open case.

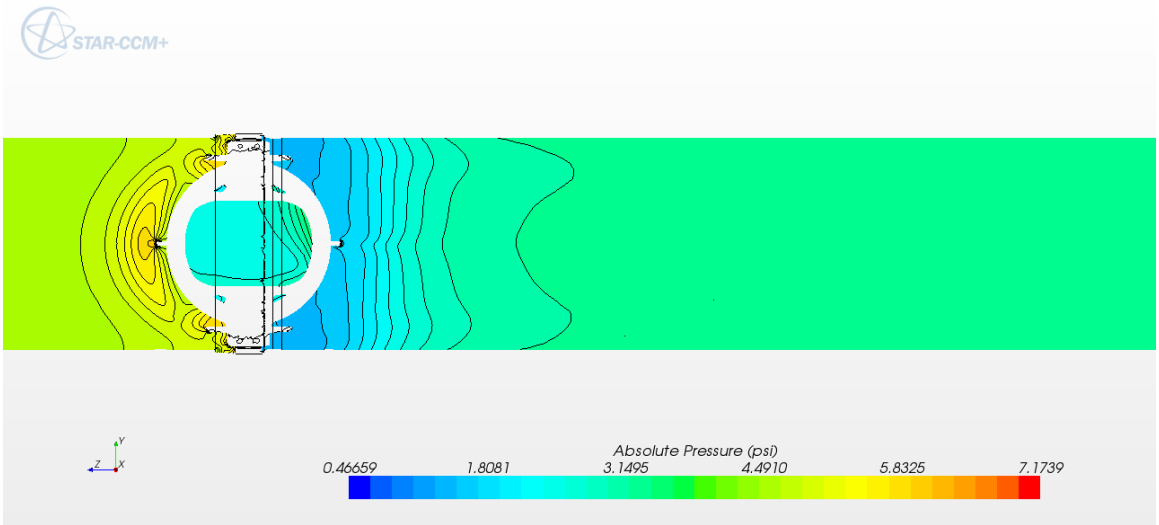

Fig. E.68: Detailed side view of absolute pressure across the butterfly valve for the 90 degree open case.

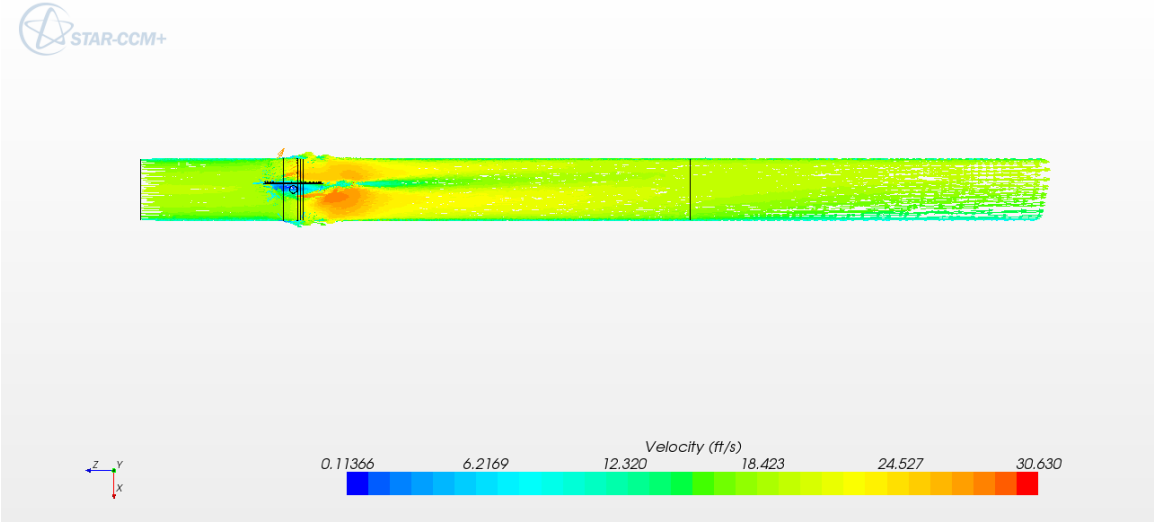

Fig. E.69: Top view of velocity vectors across the entire flow domain for the 90 degree open case.

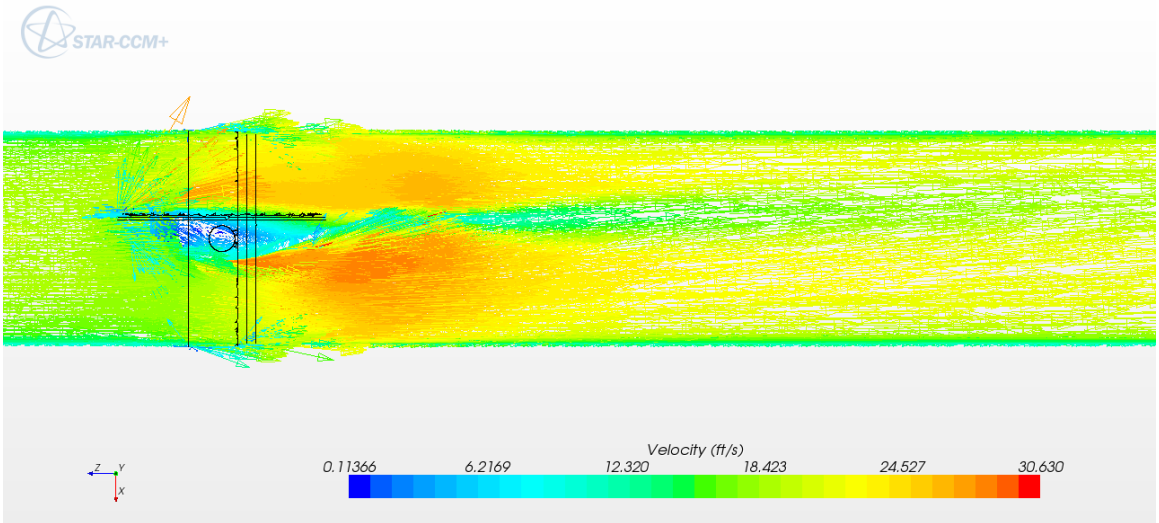

Fig. E.70: Detailed top view of velocity vectors across the butterfly valve for the 90 degree open case.

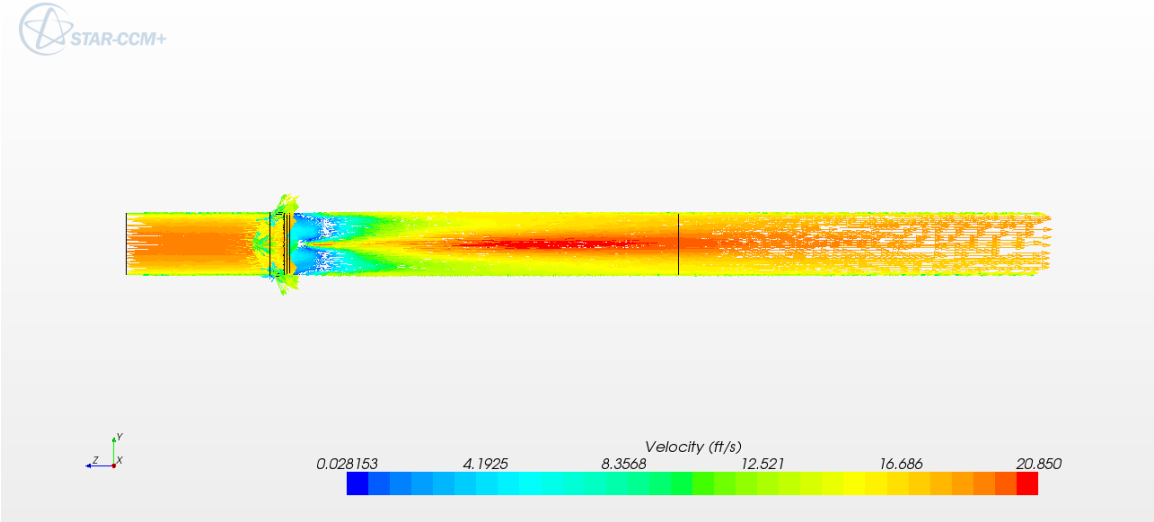

Fig. E.71: Side view of velocity vectors across the entire flow domain for the 90 degree open case.

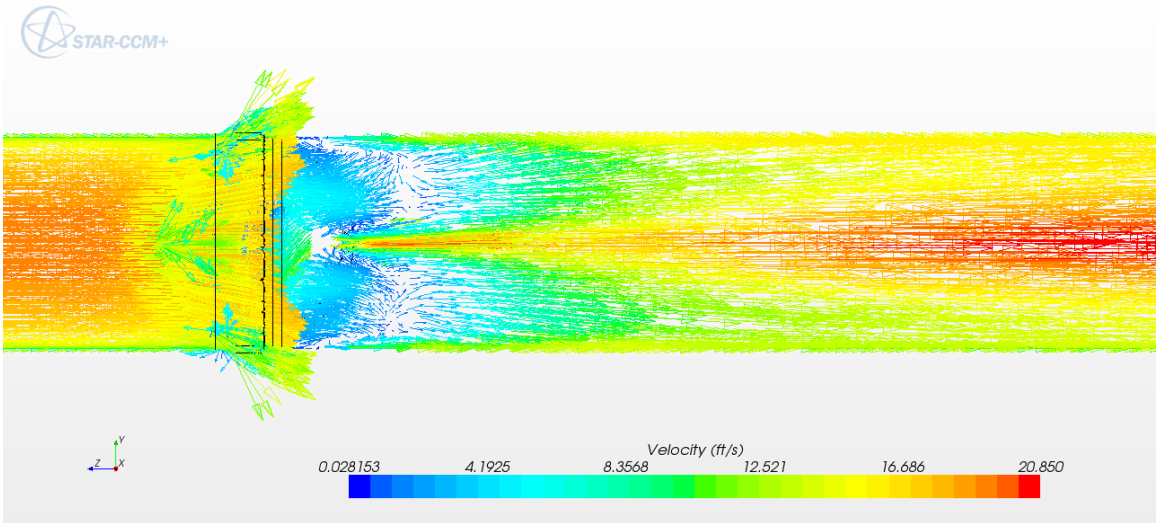

Fig. E.72: Detailed side view of velocity vectors across the butterfly valve for the 90 degree open case.